Enhancements in Electrical Impedance Tomography (EIT) Image Reconstruction for 3D Lung Imaging

BY

BRADLEY MICHAEL GRAHAM

Thesis submitted to the
Faculty of Graduate and Postdoctoral Studies
In partial fulfillment of the requirements
For the PhD degree in Electrical and Computing Engineering

School of Informtation Technology
Faculty of Graduate and Postdoctoral Studies
University of Ottawa

Abstract

Electrical Impedance Tomography (EIT) is an imaging technique which calculates the electrical conductivity distribution within a medium from electrical measurements made at a series of electrodes on the medium surface. Reconstruction of conductivity or conductivity change images requires the solution of an ill-conditioned nonlinear inverse problem from noisy data. EIT is a hard problem as it is a particularly difficult example of attempting to recover a signal from noise.

To date most EIT scanners and algorithms have been designed for 2D applications. This simplifying assumption was originally used due to the prohibitive computational complexity of solving the larger 3D problem. Contemporary PC's can now calculate 3D solutions, however at the start of this thesis the prevailing algorithms in clinical use remain 2D models that rely on *ad hoc* tweaking to produce useful reconstructions.

The aim of this thesis is to develop enhancements in EIT image reconstruction for 3D lung imaging; to remove some of the limitations that continue to impede its routine use in the clinic. The aim is attained through the systematic achievement of the following four main objectives: (1) Improve the method of hyperparameter selection in order to eliminate case by case tweaking of parameters, provide repeatability of experiments, and reduce the number of reconstructions needed to find the best reconstruction for a given data set. (2) Increase the resolution of 3D models by increasing the number of elements in the Finite Element Model (FEM). This requires the development of an algorithm to solve the large inversion using readily available computers. (3) Determine the best way to collect 3D data from the chest given some equipment limitations and a specific set constraints concerning electrode placement. (4) Determine the viability of non-blurring regularization for 3D lung imaging.

The bulk of this thesis describes how the four objectives were successfully addressed with the result that some of the major limitations discouraging and preventing the routine use of 3D models for lung imaging have been eliminated. This thesis concludes with a recommendation for how to collect and reconstruct 3D EIT images of the lungs.

Acknowledgements

I would like to dedicate this work to my children, Benjamin and Selena and to my wife Kathleen without whose love, support, and encouragement it would not have been possible.

I would like to thank my thesis supervisor Dr. Andy Adler for his friendship, ideas, guidance, and assistance in completing this thesis. I would also like to thank Dr. Bill Lionheart for helping me understand the Primal Dual - Interior Point Algorithm.

There is no such thing as luck; there is only adequate or inadequate preparation to cope with a statistical universe.

-Robert A. Heinlein

Contents

List of Figures

List of Principal Symbols

The notation of this thesis is as follows: matrices are boldface upper-case letters, column vectors are boldface lowercase letters. The $n \times n$ identity matrix is $\mathbf{I}_n$. The $(i,j)^{th}$ entry of $\mathbf{A}$ is A_{ij}, similarly the i^{th} entry of a vector $\mathbf{x}$ is x_i. Continuum operators are upper-case letters while continuum variables are lowercase letters.

General Variables

- ℓ is the electrode number
- Ω represents the medium under analysis
- Γ represents the boundary of the medium under analysis
- N number of Nodes in a FEM
- E number of elements in a FEM
- L number of electrodes in a FEM
- M number of measurements in a frame of data
- ϕ linear interpolation function
- n is noise
- $\|\cdot\|_p$ is the p norm, where p is usually 2.

Continuum Variables

- u is the potential
- $u(\hat{x})$ is the spatial potential
- F is the forward operator
- σ is the conductance or in a few places the standard deviation
- I is the current
- $\hat{n}$ normal

Discrete Variables

- $\mathbf{I}$ is the matrix or vector of nodal currents
- V_ℓ is the voltage on electrode ℓ
- $\mathbf{V}$ is the vector or matrix of nodal voltages
- $\boldsymbol{\sigma}$ is the conductance or in a few places the standard deviation
- $\mathbf{Y}$ is the admittance matrix of a FEM with simple point electrodes
- $\mathbf{A}$ is the admittance matrix of a FEM with the Complete Electrode Model
- $T[]$ is an extraction operator
- $\mathbf{z}$ is the EIT signal
- $\hat{\mathbf{x}}$ is the parameter recovered through solution of the inverse problem
- $\hat{\mathbf{n}}$ is the unit normal vector

Chapter 1

Introduction

1.1 Background

Electrical Impedance Tomography (EIT) is an imaging technique which estimates the electrical impedance distribution within some medium. Since impedance is not directly measurable it is calculated from boundary voltage measurements which are a function of the impedance and a current which is applied or injected by the EIT scanner. Using different current injection patterns and voltage measurement sequences, an approximation of the spatial distribution of the impedance or changes in impedance within the object are reconstructed. It is also possible to inject voltages and measure the resulting currents, however the majority of work to date uses the former technique.

EIT has numerous applications that can be categorized into three major fields:

1. Industrial. These applications include the imaging of fluid flows in pipelines, the measurement of fluid distribution in mixing vessels, and non-destructive testing such as crack detection [43][9].

2. Geophysical. Applications include geophysical prospecting, cross borehole measurement and surface measurement [88][93].

3. Medical. EIT is used for monitoring of pulmonary and cardiac functions, measurement of brain function, detection of haemorrhage, measurement of gastric imaging, detection and classification of tumours in breast tissue and functional imaging of the thorax [67][49][83][46][82][70][56][107]. This thesis is primarily concerned with medical imaging applications, however the results are applicable to the other fields.

EIT suffers from severe limitations that may prevent its adoption for routine medical diagnosis. Its major limitations are low spatial resolution, susceptibility to noise and electrode errors, and in medical imaging, large variability of images between subjects. Thus EIT is not suited for anatomical imaging in the way that Magnetic Resonance Imaging (MRI) or Computed Tomography (CT) are. EIT does however, show promise as a diagnostic tool for medical clinicians. It has the advantage of being relatively inexpensive (on the order of thousands of dollars) compared to modalities such as MRI, CT, and Positron Emission Tomography (PET). Moreover, EIT equipment is non-invasive, is safe, and since it is small and non-cumbersome it can be easily moved and left in place for extended time periods. Thus it may be viable for continuous bedside monitoring for such pathologies as pulmonary oedema, cerebral ventricular haemorrhage, and gastric emptying. Additionally, it has the ability to produce a high number of images per second encouraging its use in functional

as opposed to anatomical imaging. With functional applications images can be considered intermediate data for some technique such as the determination of the change in lung tidal volume.

1.2 Current state and problems

A detailed review of the current state of EIT is presented in chapters 2 and 3. Chapter 3 concludes with a discussion of the best practices used in EIT lung imaging at the start of this work.

The field of impedance imaging of lungs is immature as an engineering endeavour. Despite 20 years of research and the availability of inexpensive medical grade EIT scanners, EIT has yet to make the transition from the lab to the clinic [48]. The adoption of EIT imaging for clinical use will require algorithms that provide 3D information, improve resolution, and be robust and reliable enough that clinicians will routinely and confidently employ the equipment for diagnostics.

Although there are many papers (the bibliography lists over 80) and even a few books (for example [69]) dealing with EIT, there is a lack of rigorous evaluation and comparison of competing methods and techniques. Moreover, many algorithms (perhaps the majority) are *ad hoc* and require tweaking of parameters that prevents repeatability in experimentation. Finally, 2D algorithms continue to be used: the bulk of research in EIT has revolved around 2D finite element models. Improvements in computational power has permitted the recent development of 3D algorithms, however the use of 2D continues to be routine in lung imaging, perhaps due to the ready availability of equipment designed for 2D applications. Among other limitations, 2D imaging cannot provide vertical location information of off-plane contrasts. Although one can predict theoretically how a known off-plane contrast will affect the resulting 2D image, one cannot infer the location of the source of an artefact in a 2D image, caused by an off-plane contrast, from the 2D image. This is a severe limitation to 2D imaging that should encourage the development of 3D algorithms. The practical use of 3D imaging has been pioneered by the Industrial Process Monitoring (IPM) community. The main difference between IPM applications and lung applications is that IPM has the advantage of well known and stable electrode position information thus reconstruction models can match the tank geometry to high precision. Contrarily, lung imaging suffers from unknown *a priori* electrode position which is exacerbated by continuous electrode movement throughout data collection. These problems make difference imaging difficult and make absolute imaging practically impossible unless one can track the electrode positions.

EIT remains a promising medical imaging modality. However, to move the modality into routine use for lung imaging will, as a minimum, require the development of rigorous, repeatable and rapid 3D image reconstruction techniques. Thus the aim of this thesis is to develop Enhancements in EIT Image Reconstruction for 3D Lung Imaging. In other words, to remove some of the limitations that continue to prevent the routine use of 3D models. Although it is expected that these enhancements will be useful in other applications the specific interest in this thesis is 3D lung imaging.

1.3 Objectives

The aim of this thesis will be addressed in terms of the following four major objectives:

O1: Improve the method of hyperparameter selection in order to eliminate case by case

tweaking of parameters, provide repeatability of experiments, and reduce the number of reconstructions needed to find the best reconstruction for a given data set.

EIT is an ill-conditioned problem in which regularization is used to calculate a stable and accurate solution by incorporating some form of prior knowledge into the solution. A hyperparameter is used to control the trade-off between conformance to data and conformance to the prior. A difficulty with experimental and clinical EIT reconstruction algorithms is the tendency of algorithms to rely on subjective methods to select this hyperparameter. The absence of objective hyperparameter selection methods results in several issues which hinder experimental and clinical use of the technique: (1) users of EIT for clinical applications are uncomfortable using 'fiddle' adjustments to modify images, (2) comparisons of EIT reconstruction algorithms can be subjective due to the necessity of manual tuning of hyperparameter values, (3) experimental work is not repeatable if disparate researchers cannot objectively recreate the hyperparameter values used in the work of others, (4) meta-algorithms, such as detection of electrode errors [7], require a method to fix these values, and (5) Many existing methods of hyperparameter selection, such as the L-curve and expert selection, require the calculation of multiple reconstructions in order to obtain the algorithm's output.

O2: Increase the resolution of 3D models by increasing the number of elements in the FEM. This will require the development of an algorithm to solve the large inversion using readily available computers.

Calculation of conductivity solutions using one of the Newton type methods requires inverting large linear systems derived from finite element models in which the conductivity is constant over each element. The Hessian matrix in these linear systems scales with the square of the number of elements in the model and the square of the number of measurements used in the reconstruction. The large number of elements required for 3D reconstructions have to date restricted 3D reconstructions to coarse, low resolution (low number of elements) models. Although there is a limit to the achievable spatial resolution that is independent of mesh density, overly coarse meshes will result in the geometry of the mesh biasing the solution. Complex, accurate geometries, *a priori* structures, the increased number of measurements possible with newer machines and the desire for improved resolution in the third dimension leads to a requirement to solve large 3D models. Such reconstructions are beyond the capability of contemporary computers such as the AMD Athlon 64 3000+, 2GB RAM computers used in our lab. Thus the development of algorithms that can efficiently calculate full 3D solutions over dense finite element models using many measurements is required.

O3: Determine the best way to collect 3D data from the chest given some equipment limitations and a specific set of constraints concerning electrode placement.

Electrode placement for 2D reconstruction algorithms is typically confined to planar arrangements that match the 2D reconstruction geometry; yet the EIT problem is inherently 3D as currents cannot be confined to flow in the plane. Consequently 2D reconstructions are subject to artefacts generated by off plane contrasts. 3D reconstruction algorithms with multi-plane electrode arrangements have been used to more accurately reconstruct impedance distributions [90][99][115]. Compared to 2D there are many more ways to arrange and sequence electrodes when placing them in 3D. Given the variety of possible 3D electrode placement configurations, it is important

to know how various alternative configurations compare to one another in order to determine which one to use in a specific application such as lung imaging.

O4: Determine the viability of non-blurring regularization for 3D lung imaging.

Most common regularization methods impose smoothness constraints on solutions thereby prohibiting the reconstruction of edges in the recovered conductivity distribution. Employment of non-smooth reconstruction techniques is important for medical imaging applications of EIT as they involve discontinuous profiles which occur at inter organ boundaries. Total Variation (TV) is a promising regularization technique that permits the recovery of such discontinuities. However, TV regularization requires the solution of the inverse problem formulated as the minimization of a non-differentiable function. Application of traditional minimization techniques (Steepest Descent Method, Newton Method) is computationally prohibitive [44][23]. Recently Borsic [23] developed the Primal-Dual Interior-Point Method for solution of the TV minimization for static (absolute) EIT which reduces the complexity of the TV minimization to the point of viability for general EIT applications. However the performance of this algorithm with respect to traditional smooth algorithms is unknown.

1.4 Contributions

1.4.1 Contributions by Objective

O1: Improve the method of hyperparameter selection in order to eliminate case by case tweaking of parameters, provide repeatability of experiments, and reduce the number of reconstructions needed to find the best reconstruction for a given data set.

In this thesis a calibration-based method of objective hyperparameter selection, called *BestRes* is developed, evaluated and compared to five existing strategies for hyperparameter selection. Results of this thesis show that (1) heuristic selections of hyperparameter are inconsistent among experts, (2) generalized cross-validation approaches produce under-regularized solutions, (3) L-curve approaches are unreliable for EIT, (4) *BestRes* produces good solutions comparable to expert selections, and additionally that (5) the method can be used to reliably detect an *inverse crime* when used with the NF calculation. Thus the main contribution of this objective is the development of the *BestRes* hyperparameter selection method which is demonstrated to be as good or better than these existing methods while being stable and repeatable.

This work is described in detail in the article "Objective Selection of Hyperparameter for EIT," by BM Graham and A Adler, published in the IOP Journal Physiological Measurement (2006). Chapter 4 is a copy of this paper.

O2: Increase the resolution of 3D models by increasing the number of elements in the FEM.

In this thesis a *Nodal Jacobian Inverse Solver* algorithm that reduces the execution time and memory required to calculate reconstructions is developed. This algorithm scales with the number of nodes in a finite element mesh rather than with the number of elements. The algorithm is evaluated by comparing its performance to traditional 2D Elemental Jacobian algorithms. Its performance is then evaluated with a 21504 element 3D mesh that is too large to be solved with common linear algebra systems

based on 32 bit pointers (such as is available in current versions of Matlab). For the example used in this paper the size of the linear system is reduced by a factor of 26. The applicability of the algorithm for clinical use is shown by reconstructing experimentally measured human lung data.

Additional advantages of the *Nodal Jacobian Inverse Solver* are the ability to store the solution in a smaller number of parameters, and the ability to rapidly extract and render graphical displays of solutions using a function such as Matlab's built-in *trisurf* function. The *trisurf* function takes as input a list of vertices and associated values at each vertex. No explicit knowledge of the geometry is required, such as an element list providing connectedness between nodes, in order to display cut planes of coplanar nodes. Additionally, nodal solutions are easily processed using pixel based filtering algorithms similar to those used in image processing work.

The main contribution of this objective is the development of the *Nodal Jacobian Inverse Solver* which allows the solution of dense 3D models that were previously not solvable using commonly available linear algebra systems based on 32 bit pointers.

This work is described in the article "A Nodal Jacobian Inverse Solver for Reduced Complex EIT," by BM Graham and A Adler, published in International Journal for Information & Systems Sciences, Special Issue on Computational Aspect of Soft Field Tomography, Volume 2, Number 4 (2006). Chapter 5 is a copy of this paper.

O3: Determine the best way to collect 3D data from the chest given some equipment limitations and a specific set of constraints concerning electrode placement.

In this thesis several "regular" 3D electrode placement (EP) configurations tailored to a 16 electrode adjacent drive EIT system are proposed and evaluated in terms of several figures of merit, immunity to noise and performance in the presence of electrode placement errors. An EP configuration is defined as a combination of physical placement of the electrodes (we restrict ourselves to two planes of electrodes in this work) and a current injection pattern.

The main conclusions are the observation that none of the evaluated EP configuration offers a worthwhile improvement over the others under ideal conditions. Only when noise and electrode placement errors are considered does the choice of EP configuration become important. The Planar electrode placement is recommended for lung imaging.

The main contributions of this objective are the proposal of the EP configurations with their constraints, the rigorous evaluation of their performance and the recommendation of which of the studied EP configurations to use to collect 3D lung data.

This work is described in the article "Electrode Placement Strategies for 3D EIT," by BM Graham and A Adler, accepted for publication in the IOP Journal Physiological Measurement (2007). Chapter 6 is a copy of this paper.

O4: Determine the viability of non-smooth regularization for 3D lung imaging.

In this thesis the PD-IPM algorithm for Total Variation (TV) regularization of EIT reconstructions is evaluated and compared to the computationally less demanding quadratic regularization. The main observations are that the TV solutions of 2D models can produce the desired discontinuous solutions but require on the order of 10 iterations to converge. In comparison, the quadratic algorithm produces good, albeit smooth solutions in 1 to 3 steps. The quadratic algorithm is slightly more robust

to noise however both algorithms produce useful 2D reconstructions at realistic noise levels.

The ability of PD-IPM algorithm to reconstruct edges in 3D models was not satisfactorily determined. The PD-IPM algorithm reconstructs the conductivity in the elemental basis. The complexity of the elemental solution limits the resolution of the finite element model. Thus the capability of determining 3D TV performance is limited to relatively coarse FEMs that may limit the performance of the algorithm. Further work is required to enable the solution of higher resolution 3D models in order to evaluate the performance of PD-IPM for 3D lung imaging.

In summary, TV regularised reconstructions are considerably more expensive to calculate than quadratic reconstructions, however the TV PD-IMP algorithm is able to compute 2D non-smooth reconstructions in the presence of moderate noise, and is therefore of practical use in certain applications. It is not currently recommended for use with 3D lung imaging.

The main contribution of this objective was the improvement in convergence of the PD-IPM algorithm and the evaluation of the algorithm's performance in 2D and 3D applications.

This work is described in the article "Total Variation Regularization for EIT," by Borsic, Graham, Lionheart, and Adler. Chapter 7 is a copy of the a manuscript in preparation for submission to IEEE Transactions on Medical Imaging. This is a collaborative work. The development of the PD-IPM algorithm, it's explanation and implementation are the original work of Andrea Borsic and can be found in [23]. The analysis of the algorithm's performance, including the improvement in convergence, the simplification of the β decay schedule as well as the design and execution of the algorithm's performance evaluation and subsequent conclusions are the original contribution of this thesis. Dr Adler and Dr Lionheart are the PhD supervisors of Graham and Borsic respectively.

1.4.2 Miscellaneous Contributions

The background research for this thesis is contained in chapters 2 and 3. These chapters include, in one place, the complete development of the finite element solution of the forward problem from Laplace's equation through to the finite element solution. We are unaware of the existence of a similar end-to-end derivation elsewhere in the EIT literature.

Numerical simulation of conductivity data permits the rapid development of imaging algorithms than would not be possible if researchers were restricted to only using lab data. However, many EIT papers rely strictly on simulated data to make conclusions. Scientific and engineering results based on simulations are valuable but must be verified with empirical (lab) data. Therefore a collateral objective of this thesis is to verify simulated results with empirical data collected in our lab. Thus, where possible, the conclusions presented in this thesis are verified using the Goe-MF II adjacent stimulation tomography system (Viasys Healthcare, Höchberg, Germany).

The impulse function and point spread function are basic tools of signal processing for linear systems. Neither the impulse function nor point spread function are mentioned in the EIT literature perhaps because EIT is a non-linear modality. In this thesis pseudo-impulse phantoms are introduced and used with EIT. In section 4.3.5 we first introduce the Blur Radius measure which is an analog of the point spread function adapted for EIT using finite element meshes. The argument for the use of pseudo-impulse functions in algorithm

development and evaluation is not based on superposition since it does not hold for non-linear systems, but because they are convenient to use and work well enough in practice. Validation of their utility in spite of the lack of superposition is demonstrated by subsequent verification of algorithm performance using realistic empirical data generated by complex phantoms. Specifically although objectives 1-3 were developed and evaluated using the pseudo-impulse phantom techniques, they were ultimately verified by empirical work.

1.5 Record of Miscellaneous Observations

In the course of this research, several other areas were studied that are outside the focus area of this thesis. In order to record this work and these observations, they are recorded in the appendix.

1.6 Summary

At the start of this work the prevailing algorithms in use for clinical lung imaging were limited to 2D models that relied on *ad hoc* tweaking to produce reconstructions. The aim of this thesis was to develop enhancements in EIT image reconstruction for 3D lung imaging. The aim was attained through the systematic achievement of the four main objectives:

1. The development of the *BestRes* objective hyperparameter selection method provides a calibration based method of calculating a hyperparameter once for a specific configuration of mesh and equipment. Using this algorithm eliminates the necessity of *ad hoc* tweaking by researchers during reconstruction. Different research groups can more easily repeat the work of other research groups. Moreover, by calculating the hyperparameter off-line, a good image can be obtained from a single inversion. Contrarily, methods such as L-curve and expert selection require multiple inversions to be calculated for each useful solution.

2. The development of the *Nodal Jacobian Inverse Solver* algorithm enables the solution of large dense 3D finite element models that, previous to this work, were not solvable using linear algebra systems based on 32 bit pointers. This solver allows one to model and solve complex, accurate geometries containing *a priori* structures with a system that could not solve the same model using the traditional elemental Jacobian.

3. The evaluation of 3D EP configurations provides a rigorous basis for recommending a specific method to collect 3D lung data. Moreover it provides a sound basis to discontinue further evaluation of configurations, such as the proposed opposite configurations, that perform poorly.

4. The improvement and evaluation of the PD-IPM algorithm for TV regularization provides a defensible argument for when and when not to use TV regularization. Moreover the promising 2D results provide justification and incentive for further research into this algorithm aimed at increasing the size of 3D models that can be solved with the algorithm. The development of a nodal TV prior is a promising avenue for further research.

The work described in this thesis has removed some of the major limitations that have discouraged or prevented the routine use of 3D models for lung imaging. This thesis concludes with a recommendation for how to collect and reconstruct 3D EIT images of the lungs under the stated constraints.

Chapter 2

Forward Problem

2.1 Description of a Basic EIT System and Experiment

The following two sections describe a prototypical EIT system for 2D medical applications. The remainder of chapter 2 along with chapter 3 expand on the components and variations of the prototype system.

2.1.1 Data Collection

A typical EIT system uses a set of electrodes attached to the surface of the medium being imaged. One can apply current or voltage to the electrodes and then measure the resulting voltage or current respectively. In most practical systems an alternating current is applied to some electrodes and the resulting voltages are measured at the other electrodes. Assume that $\ell = 16$ electrodes have been fixed around the surface of the object such as the medium in figure 2.1. There are many ways to apply current and measure the resulting voltages

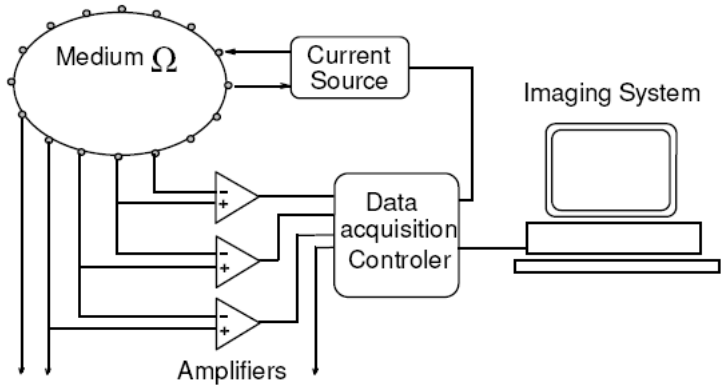

Figure 2.1: *Typical Imaging System with 16 Electrodes attached to the boundary of an object for current injection and voltage measurement (from [3]).*

which will be discussed in section 2.5.1. With the *Adjacent* drive pattern [16], current is applied to an adjacent pair of electrodes and the resultant voltages between the remaining 13 adjacent pairs of electrodes is measured. The three possible measurements involving one or both of the current injecting electrode are not used. This procedure is repeated 16 times with current injected between successive pairs of adjacent electrodes until all 16 possible pairs of adjacent electrodes have been used to apply the known current. This is

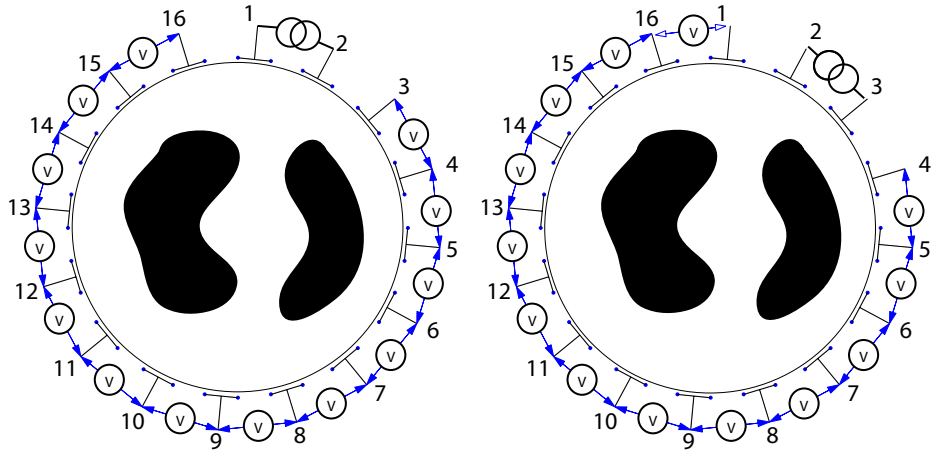

(a) *First drive pair* (b) *Second drive pair*

Figure 2.2: *Adjacent drive patterns*

shown schematically in figure 2.2. In figure 2.2(a) current is injected through electrode pair $(1, 2)$ and the resulting boundary voltage differences are measured from electrode pairs $(3, 4), (4, 5), ..., (14, 15), (15, 16)$. Voltages are not measured between pairs $(16, 1), (1, 2)$, or $(2, 3)$. In figure 2.2(b) the current is injected between pair $(2, 3)$, and the voltage differences measured between pairs $(4, 5), (5, 6), ..., (15, 16), (16, 1)$. This process is repeated until current has been injected between all 16 adjacent pairs of electrodes. This is called a *frame* of data and will produce $16 \times 13 = 208$ measurements. By convention the data frame is arranged as a column vector of length 208. Frame acquisition periods have decreased over the years. For example the equipment used for the empirical work of this thesis, the Goe-MF II type tomography system manufactured by Viasys Healthcare, Höchberg, Germany, collects 12.5 frames per second (80ms per frame).

There are various situations, which will be discussed later, in which it is necessary to numerically calculate the potential field within a medium. A mathematical model of the spatial potential field, $u(\vec{x})$, resulting from injected current patterns over a known conductivity can be formulated as $u(\vec{x}) = F(\sigma, I)$ where F is a forward operator that calculates the spatial potential as a function of the conductivity, σ, and the current injection pattern, I. Here $\vec{x}$ is a position vector which for 2D is a function of (x, y). This model is known as the *forward model* in EIT.

The forward problem is numerically solved using the Finite Element Method (FEM) which will produce an algebraic equation of the form $\mathbf{V} = \mathbf{Y}(\sigma)^{-1}\mathbf{I}$ in which $\mathbf{Y}$ is the FEM system matrix, also known as the admittance matrix, $\mathbf{V}$ is a matrix of voltages. The i^{th} column of $\mathbf{V}$ contains the nodal voltages for current injection pattern i. $\mathbf{I}$ is a matrix of the net current into each node. The i^{th} column of $\mathbf{I}$ contains the nodal currents for current injection pattern i. An operator $T[]$ can be defined to extract the 208 voltage measurements from the finite element model solution as $\mathbf{v} = T[\mathbf{V}] = T[\mathbf{Y}(\sigma)^{-1}\mathbf{I}]$ where $\mathbf{v}$ is the vector of voltage measurements corresponding to a data frame. Numerical solution of the forward problem is the subject of chapter 2.2.

2.1.2 Reconstruction

The process of estimating the impedance from the measured data is known as the *inverse problem* in EIT. The inverse problem is solved using a reconstruction algorithm of which

there are two primary types in EIT. *Static imaging* attempts to recover an estimate of the absolute conductivity of the medium from which the boundary data was acquired. Static imaging is discussed in section 3.3. *Difference imaging* attempts to recover an estimate of the change in conductivity over some interval based on data frames measured at two times, see figure 2.3. Difference images can be calculated in a single step with a linearized

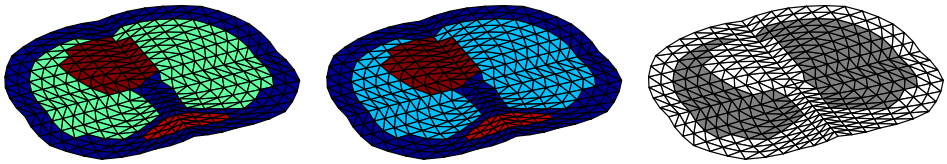

(a) $\boldsymbol{\sigma}$ *at* t_1 (b) $\boldsymbol{\sigma}$ *at* t_2 (c) *Conductivity Change*

Figure 2.3: *Example of 2D difference Image reconstruction*

algorithm, however this assumes that the impedance change over the interval is small. For large impedance changes one needs to solve the non-linear problem with an iterative algorithm. The difference imaging algorithms discussed in this thesis are all of the one-step linearized class.

Define a signal $\mathbf{z} = \mathbf{v_2} - \mathbf{v_1}$, where $\mathbf{v_1}$ is a vector of voltage measurements taken at time t_1 and $\mathbf{v_2}$ is a vector of voltage measurements taken at time t_2. The estimation of a difference image is calculated with an equation of the form

$$\hat{\mathbf{x}} = \mathbf{B}\mathbf{z} \tag{2.1}$$

where $\hat{\mathbf{x}} = \Delta\boldsymbol{\sigma}$ is the change in conductivity between times t_1 and t_2, and $\mathbf{B}$ is a regularized linearized reconstruction operator. It is also possible to define a "normalized difference" signal in which $\mathbf{z}$ is defined as $z_i = \sum_{i}^{length(\mathbf{v})} \left(v_{2,i} - v_{1,i}\right)/v_{1,i}$ where $v_{1,i}$ and $v_{2,i}$ are the i^{th} elements of the vectors $\mathbf{v_1}$ and $\mathbf{v_2}$ respectively. This signal is not used in the current development but is further discussed in section 4.5.3.1.

Calculation of the impedance or impedance changes based on the boundary voltage data is an instance of an ill-conditioned, inverse problem. Such problems are unstable and require some method of improving the conditioning to achieve stability. The most common method is regularization, which involves trading off fidelity to the data against adherence to some *a priori* condition on the solution. Typically, this means that the inverse problem is augmented with a side constraint that is either chosen in an *ad hoc* manner, or based on some sort of prior information about the solution such as amplitude (norm) or smoothness. Numerical solution of the inverse problem is the subject of chapter 3. Figure 2.4 shows an experimental setup of a Goe Type II analyzer connected to one of the several tanks used for phantom studies.

2.2 The Forward Problem

Most EIT equipment uses alternating currents (AC) thus the various loads under analysis could have reactive components. AC reduces electrode corrosion through electrolytic effects, AC detectors can extract the injected signal from the electrodes while filtering out other signals such as the cardiac cycle, and in medical applications AC is required to meet safety standards. Amplitude and frequency vary with application from several Amperes and low frequency in geophysical applications to medical applications using 1-10mA and

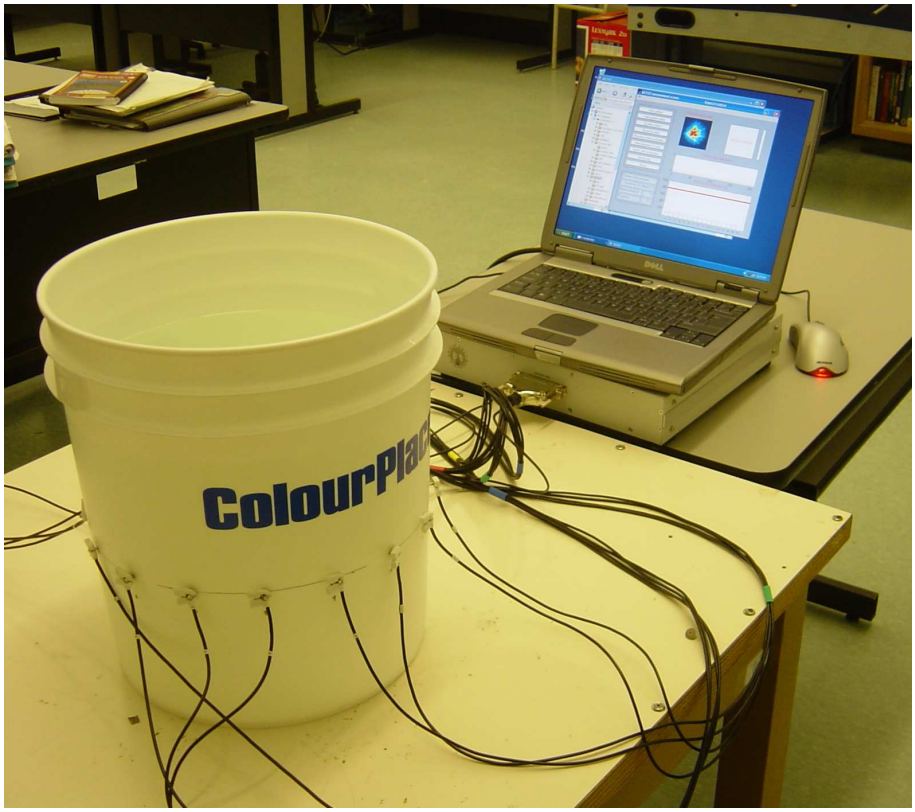

Figure 2.4: *Typical experimental setup with laptop computer and Goe-MF II type tomography system (Viasys Healthcare, Höchberg, FRG) connected to a tank with 16 electrodes.*

10kHz-1MHz. Often in industrial applications loads are assumed to be mainly resistive or mainly capacitive. In these cases only the in-phase or the out-of-phase voltage component is measured therefore only the real or imaginary part of the impedance is estimated. Such applications are referred to as Electrical Resistance Tomography (ERT) and Electrical Capacitance Tomography (ECT). The work of this thesis is based on a family of medical equipment that works with up to 50kHz current. At this low frequency, to a good approximation, only the conductance or equivalently the resistivity is estimated. Thus the work discussed in this thesis is restricted to the recovery of conductance only. One could therefore talk in terms of Electrical Conductance Tomography or the more accepted Electrical Resistance Tomography. However, in keeping with common usage, the term EIT will be maintained. The thesis of Polydorides [98] addresses the estimation of both the real and complex components of the impedance.

In inverse problems a *forward model* is used to predict observations. In the specific case of EIT, a model that predicts the spatial electric field resulting from applying a current to a known conductivity distribution is required. The capability to calculate the electric fields within an object also provides an efficient method to assemble the Jacobian matrix which is necessary to solve the inverse problem.

2.2.1 Physics of the problem - from Maxwell to Laplace

An arbitrary medium, Ω, undergoing electrical stimulation has electrical properties that vary as a function of position and time. These properties are represented by the electrical

impedance, $\sigma(\vec{x},t) + j\omega(\vec{x},t)$, and relative permittivity $\epsilon(\vec{x},t)$ where $\vec{x} = (x_1, x_2)$ for 2D or $\vec{x} = (x_1, x_2, x_3)$ for 3D is the position vector. This work does not consider the temporal aspect of these functions nor, as discussed above, are the reactive components significant. It is also common practice to neglect the effect of magnetic fields in medical applications because the current and frequencies are low. At high frequencies magnetic effects cannot be ignored [110], however, under low frequency conditions the electrical properties are entirely described by the conductivity, $\sigma(\vec{x})$. Additionally, only the case in which the object being imaged has a linear and isotropic conductivity is considered.

A mathematical model of the problem is derived from Maxwell's equations [3]. Outside the medium, Ω, there is no current flow because the conductivity is zero. Energy is applied to the medium in the form of current injection on the boundary, Γ, which sets up a distribution of voltage, $u(\vec{x})$, and a pattern of current flow, $J(\vec{x})$, in the medium. The electric potential, $u(\vec{x})$, can be expressed by an elliptic partial differential equation known as Laplace's equation or just the Laplacian:

$$\nabla \cdot (\sigma \nabla u) \quad = \quad 0 \quad in\, \Omega \tag{2.2}$$

Laplace's equation can be derived starting from the point form of Ohm's Law:

$$J = \sigma E \tag{2.3}$$

where the electric field vector, E, is obtained from the scalar potential function $u(x)$ by taking the negative of the gradient of u:

$$E = -\nabla u \tag{2.4}$$

Applying the field equivalent of Kirchoff's current law, which states that the net current leaving a junction of several conductors is zero, yields:

$$\nabla J = 0 \tag{2.5}$$

Substituting 2.4 into 2.3 and taking the divergence of both sides in accordance with 2.5 gives Laplaces's equation 2.2 for the electric potential inside some medium. Cheney and Isaacson [37] provide the following intuitive description of this equation:

> "To understand where the equation comes from, it helps to read it from the inside out. The inside nabla takes the gradient of the potential, $u(\vec{x})$, computing the direction in which electrons will tend to flow, as well as the rate of change of voltage in that direction. In electric circuits, the conductance of a wire times the change in voltage gives the current passing through the wire. The tissue inside the human body act like an electrical resistor, so the same principle applies: $\sigma(\vec{x})$ times the gradient of $u(\vec{x})$ represents the current at point $\vec{x}$. Finally the outer nabla computes the divergence of the current, a measure of its tendency to flow into or out of one spot. As long as no charge is building up inside the body (a reasonable assumption), the divergence equals zero. The inverse electrical impedance problem is non-linear because the unknown conductivity and potential are multiplied together."

The boundary conditions on Γ, the boundary of Ω, are formed by fixing the normal current, $J_{\hat{\mathbf{n}}}$, at every point of Γ. Representing the normal vector by $\hat{\mathbf{n}}$, we have

$$J_{\hat{\mathbf{n}}} = -\sigma \frac{\partial u}{\partial \hat{\mathbf{n}}} \quad \text{on } \Gamma \tag{2.6}$$

The presence of the electrodes is taken into account via appropriate boundary conditions which will appear as modifications to the equation for normal current, 2.6, on Γ. Electrode models are discussed in section 2.3.3. Equations 2.2 and 2.6 comprise the *forward problem* in EIT and are used to find the voltage distribution within the medium. Analytic methods using series approximations [76][33] have been used to solve the forward problem for simplified models such as a single contrast in a circular medium. However, solving the forward problem for models with arbitrary geometries requires numerical techniques such as the finite element method. With such methods continuum problems of 2.2 and 2.6 are converted into discrete algebraic problems that can be solved with a computer.

2.3 Finite Element Method

The Finite Element Method (FEM) is a numerical analysis technique for obtaining approximate solutions to a wide variety of engineering problems. It was originally developed as a tool for aircraft design but has since been extended to many other fields including the modeling of electromagnetic and electrostatic fields [106]. Due to its ability to model arbitrary geometries and various boundary conditions the Finite Element Method is the most common method currently used for the numerical solution of EIT problems [92][100]. The following paragraphs borrow heavily from [75].

In a continuum problem of any dimension the field variable, such as the electric potential in EIT, is defined over an infinite number of values because it is a function of the infinite number of points in the body. The finite element method first discretizes the medium under analysis into a finite number of elements collectively called a finite element *mesh*. Within each element the field variable is approximated by simple functions that are defined only within the individual element. The approximating functions (sometimes called interpolation or shape functions) are defined in terms of the values of the field variables at specified points on the element called nodes. Most EIT work uses linear shape functions in which all nodes lie on the element boundaries where adjacent elements are connected. Higher order shape functions will have interior nodes. In summary, the finite element method reduces a continuum problem of infinite dimension to a discrete problem of finite dimension in which the nodal values of the field variable and the interpolation functions for the elements completely define the behaviour of the field variable within the elements and the individual elements collectively define the behaviour of the field over the entire medium.

There are three different methods typically used to formulate Finite Element problems:

1. Direct approach. The Direct approach is so called because of its origins in the direct stiffness method of structural analysis. The method is limited, however it is the most intuitive way to understand the finite element method.

2. Variational approach. Element properties obtained by the direct approach can also be determined by the Variational approach which relies on the calculus of variations and involves extremizing a functional such as the potential energy. The variational approach is necessary to extend the finite element method to a class of problems that cannot be handled by direct methods. For example problems involving elements with non-constant conductivity, for problems using higher order interpolation functions and for element shapes other than triangles and tetrahedrons.

3. Method of Weighted Residuals (MWR). The most versatile approach to deriving element properties is the Method of Weighted Residuals. The weighted residuals approach begins with the governing equations of the problem and proceeds without

relying on a variational statement. This approach can be used to extend the finite element method to problems where no functional is available. The method of weighted residuals is widely used to derive element properties for non-structural applications such as heat transfer and fluid mechanics.

Regardless of the particular finite element method selected, the solution of a continuum problem by the finite element method proceeds with following general sequence of operations:

1. Discretize the continuum. The FE method consists of discretizing the spatial domain, denoted Ω, into a number of non-uniform, non-overlapping, elements connected via nodes. Triangles and rectangles are used in 2D problems while tetrahedral and hexahedral elements are used for 3D. Additionally meshes using a mixture of different types of elements are possible. In this thesis only simplices (triangles for 2D and tetrahedrons for 3D) are used. Figure 2.5(a) shows a 2D mesh constructed of triangles while figure 2.5(b) is a 3D mesh constructed of tetrahedrons.

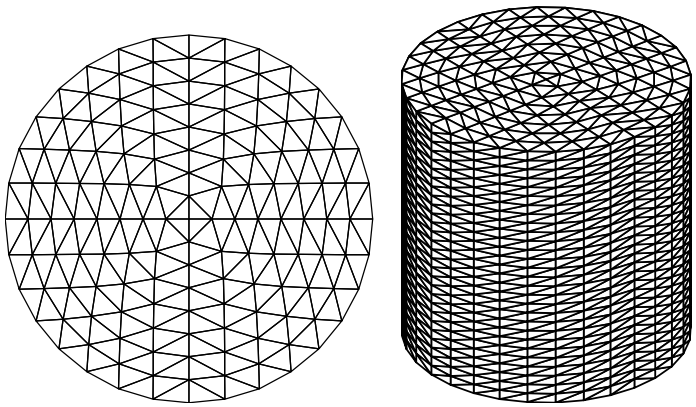

(a) *2D Mesh with 256 Elements* (b) *3D Mesh with 21504 Elements*

Figure 2.5: *Example 2D and 3D discretizations*

2. Select interpolation functions. The field variable is approximated within each element by an interpolating function that is defined by the values of the field variable at the nodes of the element. Interpolation functions can be any piecewise polynomial function defined at a number of nodes. Linear interpolation functions are used for most of the work in this thesis. Other interpolation functions have been used with EIT, for example Marko *et al* use quadratic interpolation functions in [116].

3. Find the element properties. This means calculating the local matrix for each element. The symbol Y with appropriate subscripts is used to denote the components of local matrices throughout this thesis.

4. Assemble the element properties to obtain a system equations. This means combining the local matrices into a single master or global matrix. The symbol $\mathbf{Y}$ or $\mathbf{A}$ without subscripts are used throughout to denote the global matrix.

5. Impose the Boundary Conditions (BC). Boundary conditions can be fixed (also known as Type I, Dirichlet, or essential boundary conditions), derivative (also known as Type

II, Neumann, or natural boundary conditions), or a combination of both (mixed, also known as Type III boundary conditions). With Dirichlet boundary conditions the value of the field variable is prescribed for selected boundary nodes. For Neumann conditions the derivative of the field variable is prescribed at selected boundary nodes.

6. Solve the system of equations. The algebraic system is of the form $\mathbf{YV} = \mathbf{I}$. The system is solved by Linear Algebra software such as Matlab.

7. Make additional computations if desired. This would be required for iterative algorithms, algorithms that use adaptive currents and adaptive mesh refinement.

In the next two sections the Direct approach and the MWR are described by expanding the above items. Hua *et al* provide a derivation of the Variational method for EIT in [74].

2.3.1 Direct Approach

The following section is derived from material in [106][74][92][69] and [70]. The Direct Approach can only be used for relatively simple problems and simple element shapes. For EIT this means the direct method can only be used for finite elements of constant conductivity with linear shape functions. In this case the finite element model for EIT is equivalent to a linear electrical network (lumped resistor network) that connects the nodes [92]. In the 2D

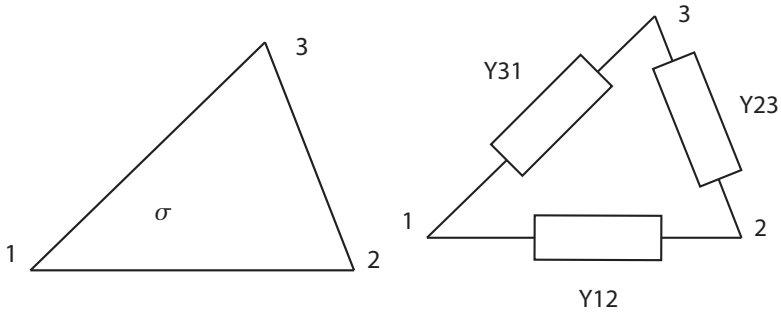

(a) *Triangular Element* (b) *Equivalent Circuit*

Figure 2.6: *Derivation from Resistor Network*

case a triangle such as figure 2.6(a) is equivalent to the electrical network of figure 2.6(b). In this conversion each edge of the triangle is replaced by a resistor whose conductance is $\sigma\cot\theta_j$ where resistor j is the resistor opposite the j^{th} angle [69]. The three dimensional case is similar with θ_j being the angle between the two faces meeting at the j^{th} edge. In terms of nodal coordinates, the conductance Y_{ij}, between node i and node j is determined by the triangle-to-network conversion as

$$Y_{ij} = \frac{\sigma_e}{2A_e}(b_i b_j + c_i c_j), (i \neq j) \tag{2.7}$$

with $b_1 = y_2 - y_3,\ b_2 = y_3 - y_1,\ b_3 = y_1 - y_2$ and $c_1 = x_3 - x_2,\ c_2 = x_1 - x_3,\ c_3 = x_2 - x_1$ where $(x_i, y_i)(i = 1, 2, 3)$ denotes a coordinate of each node, A_e indicates the area of an element and σ_e is the element conductivity (sheet conductivity) which is assumed to be constant over the element. Superscript e refers to element e. Kirchoff's current law for the circuit is written as

$$\begin{bmatrix} Y_{11} & Y_{12} & Y_{13} \\ Y_{21} & Y_{22} & Y_{23} \\ Y_{31} & Y_{32} & Y_{33} \end{bmatrix} \begin{bmatrix} u_1 \\ u_2 \\ u_3 \end{bmatrix} = \begin{bmatrix} c_1 \\ c_2 \\ c_3 \end{bmatrix} \text{ or } \mathbf{Y}^e\mathbf{U}^e = \mathbf{I}^\mathbf{e}$$

with $Y_{11} = -Y_{12} - Y_{13},\ Y_{22} = -Y_{21} - Y_{23}, Y_{33} = -Y_{31} - Y_{32},\ Y_{ij} = Y_{ji},$ for $i, j = 1, 2, 3$ where $u_i (i = 1, 2, 3)$ are the nodal potentials and $c_i (i = 1, 2, 3)$ is the prescribed current which flows in the i^{th} node.

2.3.1.1 Assemble the element properties to obtain the system equations

The two element mesh of figure 2.7 is used to illustrate the assembling of the global admittance matrix. The master matrix $\mathbf{Y}$ is assembled with the conductances between adjacent elements adding in parallel as in figure 2.7. These two elements share nodes 2 and 4, however Y_{24} will be different for each triangle since the conductivity, σ_e, and the geometry is different for each element. For the mesh of figure 2.7 the local matrices are:

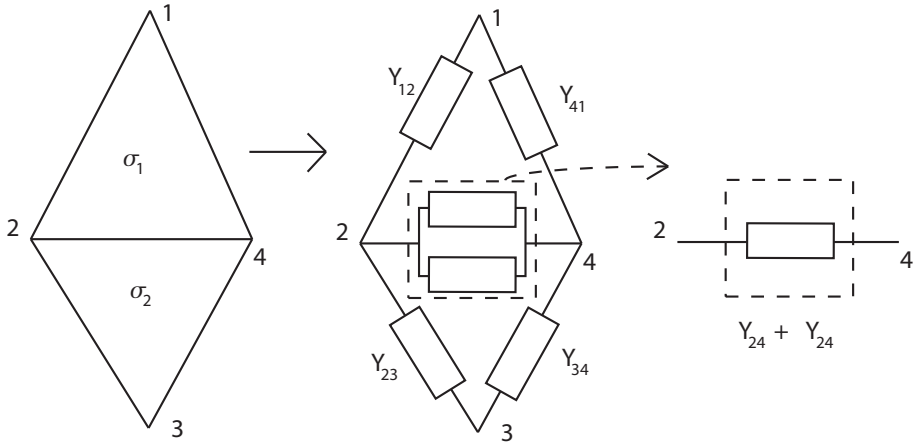

Figure 2.7: *Connection of Two Elements [92]*

$$Y_{ij}^{(1)} = \begin{bmatrix} Y_{11} & Y_{12} & Y_{14} \\ Y_{21} & Y_{22} & Y_{24} \\ Y_{41} & Y_{42} & Y_{44} \end{bmatrix} \quad i, j \in [1, 2, 4] \text{ are the global node indices for element 1}$$

$$Y_{ij}^{(2)} = \begin{bmatrix} Y_{22} & Y_{23} & Y_{24} \\ Y_{32} & Y_{33} & Y_{34} \\ Y_{42} & Y_{43} & Y_{44} \end{bmatrix} \quad i, j \in [2, 3, 4] \text{ are the global node indices for element 2}$$

These are combined as follows:

$$\mathbf{Y} = \begin{bmatrix} Y_{11} & Y_{12} & Y_{13} & Y_{14} \\ Y_{21} & Y_{22} + Y_{22} & Y_{23} & Y_{42} + Y_{42} \\ Y_{31} & Y_{32} & Y_{33} & Y_{34} \\ Y_{41} & Y_{42} + Y_{42} & Y_{43} & Y_{44} + Y_{44} \end{bmatrix} \quad i, j \in [1:4]$$

2.3.1.2 Impose Boundary Conditions

There are four common boundary conditions known as electrode models in EIT. They are the Continuum, Gap, Shunt and Complete Electrode Models [112]. We describe the Gap electrode model which is simplest model to implement numerically. In the Gap electrode model electrodes are connected directly to selected nodes on the boundary of the FEM. With the adjacent drive protocol current is applied at the two boundary nodes that represent a pair of electrodes while the currents at the remaining nodes are set to 0 in accordance with

Kirchoff's current law. The resulting potential field is calculated by solving the following algebraic system of equations:

$$\mathbf{YV} = \mathbf{I} \tag{2.8}$$

where $\mathbf{Y}$ is the global admittance matrix which is a function of the FEM and the conductivity, $\mathbf{V}$ is a vector of nodal voltages

$$\mathbf{V} = [u_1, u_2, ..., u_N]^T \tag{2.9}$$

and $\mathbf{I}$ is the current vector which for the adjacent drive is a permutation of

$$\mathbf{I} = [0, 0, ..., -1, 1, ...0]^T \tag{2.10}$$

The non-zeros represent the current driven between a pair of electrodes while the zeros represent the current at each node which is zero by Kirchoff's current law. The two non-zero elements of equation 2.10 are not necessarily adjacent elements of the vector $\boldsymbol{I}$. By convention ± 1 are used as the current values, however when matching lab equipment one uses the current values injected by the equipment, for example $5mA$ for the equipment in our lab. Equation 2.8 is solved for the nodal voltages as $\mathbf{V} = \mathbf{Y}^{-1}\mathbf{I}$. Thus using the Direct approach with the Gap model the forward problem can be viewed as using Kirchoff's current law to solve a large network assembled as a set of simultaneous linear equations.

With the adjacent current pattern equation 2.8 is solved once for each pair of electrodes being driven thus $\mathbf{I}$ can be assembled as a matrix where each column is a permutation of the vector equation 2.10 and $\mathbf{V}$ then becomes a matrix in which each column contains the nodal voltage for a single current injection. The entire algebraic system has the form:

$$\begin{bmatrix} u_{11} & \cdots & \cdots & u_{1M} \\ \vdots & \ddots & u_{ij} & \vdots \\ \vdots & u_{ij} & \ddots & \vdots \\ u_{1M} & \cdots & \cdots & u_{NM} \end{bmatrix} = \begin{bmatrix} 1 & 0 & \cdots & 0 \\ 0 & Y_{22} & \cdots & Y_{2N} \\ \vdots & \vdots & \ddots & \vdots \\ 0 & Y_{N2} & \cdots & Y_{NN} \end{bmatrix}^{-1} \begin{bmatrix} c_{11} & \cdots & \cdots & c_{1M} \\ \vdots & \ddots & c_{ij} & \vdots \\ \vdots & c_{ij} & \ddots & \vdots \\ c_{1M} & \cdots & \cdots & c_{NM} \end{bmatrix} \tag{2.11}$$

Thus u_{ij} is the voltage at the i^{th} node due to the j^{th} current injection pattern while c_{ij} is the current at the i^{th} node during the j^{th} current injection pattern. As with equation 2.10 each column of i has only two non-zero entries and is a permutation of $\mathbf{I} = [0, 0, ..., -1, 1, ...0]^T$. Since electrodes in the Gap model map to a single node each the voltages measured between a pair of electrodes is determined by the difference between two nodal values where the specific nodes are those corresponding to the electrodes. The voltages measured between adjacent electrodes are collected into a column vector through the use of an extraction operator, $T[]$. For example if v_9 is defined to be the voltage measured between electrodes 4 and 5 during injection pattern 2, then the operator T will give $T[\mathbf{V}]_9 = \mathbf{V}_{42} - \mathbf{V}_{52}$.

Solving equation 2.8 for $\mathbf{V}$ requires the inversion of $\mathbf{Y}$. Although $\mathbf{Y}$ is square and sparse it is also singular. To make the system non-singular a reference node is selected. This is the same as choosing an arbitrary ground. For convenience node 1 is arbitrarily selected. To implement this in the linear equation all entries in row 1 and column 1 of the admittance matrix are set to 0 and the diagonal elements is set to 1. To ensure that the potential will remain zero at that node during each injection pattern the corresponding element of each current vector in $\mathbf{I}$ is set to zero.

Solution of equation 2.11 provides the potential values at the nodes. Interpolation functions are used to calculate the potential within each element. The following discussion derives the linear interpolation function over a triangular element. The derivation for a tetrahedron is similar and is included in the subsequent section.

2.3.1.3 Derivation of Linear Interpolation Functions, ϕ_i

Before proceeding to the Method of Weighted Residuals the one must derive the linear interpolation functions of the field variable. The following derivation is based on [106]. The potential within a typical triangular element can be approximated by the linear function:

$$U(x,y) = a + bx + cy = \begin{bmatrix} 1 & x & y \end{bmatrix} \begin{bmatrix} a \\ b \\ c \end{bmatrix} \tag{2.12}$$

Thus the true continuous potential distribution over the x-y plane is modelled by a piecewise planar function U. The equation must hold at each node i where $U = U_i$ when $(x,y) = (x_i, y_i)$ thus the coefficients a, b, c in equation 2.12 are found from the three independent simultaneous equations, which are obtained by requiring the potential to assume the values U_1, U_2, U_3 at the three nodes. Substituting each of these three potentials and their geometric nodal positions into equation 2.12 yields three equations which can be collected to form the matrix equation

$$\begin{bmatrix} U_1 \\ U_2 \\ U_3 \end{bmatrix} = \begin{bmatrix} 1 & x_1 & y_1 \\ 1 & x_2 & y_2 \\ 1 & x_3 & y_3 \end{bmatrix} \begin{bmatrix} a \\ b \\ c \end{bmatrix} \tag{2.13}$$

The coefficients a, b, c are determined by

$$\begin{bmatrix} a \\ b \\ c \end{bmatrix} = \begin{bmatrix} 1 & x_1 & y_1 \\ 1 & x_2 & y_2 \\ 1 & x_3 & y_3 \end{bmatrix}^{-1} \begin{bmatrix} U_1 \\ U_2 \\ U_3 \end{bmatrix} \tag{2.14}$$

Denote the inverse of the coefficient matrix by $\mathbf{C}$ which is

$$\mathbf{C} = \begin{bmatrix} 1 & x_1 & y_1 \\ 1 & x_2 & y_2 \\ 1 & x_3 & y_3 \end{bmatrix}^{-1} = \begin{bmatrix} x_2y_3 - x_3y_2 & y_1x_3 - x_1y_3 & x_1y_2 - y_1x_2 \\ y_2 - y_3 & y_3 - y_1 & y_1 - y_2 \\ x_3 - x_2 & x_1 - x_3 & x_2 - x_1 \end{bmatrix} / det(\mathbf{C})$$

In 2D the determinant is equal to twice the triangle's area. The determinant of $\mathbf{C}$ is

$$det(\mathbf{C}) = 2A = x_2y_3 - x_3y_2 - x_1y_3 + x_3y_1 + x_1y_2 - x_2y_1$$

Substitution into 2.12 yields the potential function over the element:

$$U(x,y) = \begin{bmatrix} 1 & x & y \end{bmatrix} \begin{bmatrix} a \\ b \\ c \end{bmatrix} = \begin{bmatrix} 1 & x & y \end{bmatrix} \begin{bmatrix} c_{11} & c_{12} & c_{13} \\ c_{21} & c_{22} & c_{33} \\ c_{31} & c_{32} & c_{23} \end{bmatrix} \begin{bmatrix} U_1 \\ U_2 \\ U_3 \end{bmatrix}$$

where c_{ij} are the elements of $\mathbf{C}$. This can be more easily written as a summation:

$$U(x,y) = \sum_{i=1}^{3} U_i \phi_i(x,y) \tag{2.15}$$

where the interpolation functions, $\phi_i(x,y)$ $i \in (1,2,3)$ are given by:

$$\phi_i = c_{1i} + c_{2i}x + c_{3i}y$$

which are explicitly:

$$\begin{array}{l}\phi_1 = \frac{1}{2A}\{(x_2y_3 - x_3y_2) + (y_2 - y_3)x + (x_3 - x_2)y\} \\ \phi_2 = \frac{1}{2A}\{(x_3y_1 - x_1y_3) + (y_3 - y_1)x + (x_1 - x_3)y\} \\ \phi_3 = \frac{1}{2A}\{(x_1y_2 - x_2y_1) + (y_1 - y_2)x + (x_2 - x_1)y\}\end{array} \tag{2.16}$$

These newly defined functions are interpolatory on the three vertices of the triangle and are identical to equation 2.7 shown in the direct method of section 2.3.1. Each function, ϕ_i is zero at all vertices except one where it's value is one:

$$\begin{array}{ll}\phi_i(x_j, y_j) & = 0 \quad i \neq j \\ & = 1 \quad i = j\end{array}$$

Equation 2.15 completely defines the potential within the triangular element as a function of the values of the potential at the element's three nodes. In an analogous manner the linear interpolation functions for a 3D model are derived in the next section.

2.3.1.4 Derivation of Linear Interpolation Functions in 3D

The potential within a typical tetrahedral element can be approximated by the linear function:

$$U(x, y, z) = a + bx + cy + dz = \begin{bmatrix} 1 & x & y & z \end{bmatrix} \begin{bmatrix} a \\ b \\ c \\ d \end{bmatrix} \tag{2.17}$$

Thus the true continuous potential distribution over three space is modelled by a piecewise hyper-planar function U.

The equation must hold at each node i where $U = U_i$ when $(x, y, z) = (x_i, y_i, z_i)$ thus the coefficients a, b, c, d in equation 2.17 are found from the four independent simultaneous equations, which are obtained by requiring the potential to assume the values U_1, U_2, U_3, U_4 at the four nodes. Substituting each of these four potentials and their geometric nodal positions into equation 2.17 yields four equations which can be collected to form the matrix equation

$$\begin{bmatrix} U_1 \\ U_2 \\ U_3 \\ U_4 \end{bmatrix} = \begin{bmatrix} 1 & x_1 & y_1 & z_1 \\ 1 & x_2 & y_2 & z_2 \\ 1 & x_3 & y_3 & z_3 \\ 1 & x_4 & y_4 & z_4 \end{bmatrix} \begin{bmatrix} a \\ b \\ c \\ c \end{bmatrix} \tag{2.18}$$

The coefficients a, b, c, d are determined by

$$\begin{bmatrix} a \\ b \\ c \\ d \end{bmatrix} = \begin{bmatrix} 1 & x_1 & y_1 & z_1 \\ 1 & x_2 & y_2 & z_2 \\ 1 & x_3 & y_3 & z_3 \\ 1 & x_4 & y_4 & z_4 \end{bmatrix}^{-1} \begin{bmatrix} U_1 \\ U_2 \\ U_3 \\ U_4 \end{bmatrix}$$

Denote the inverse of the coefficient matrix by $\mathbf{C}$ which is

$$\mathbf{C} = \begin{bmatrix} 1 & x_1 & y_1 & z_1 \\ 1 & x_2 & y_2 & z_2 \\ 1 & x_3 & y_3 & z_3 \\ 1 & x_4 & y_4 & z_4 \end{bmatrix}^{-1} = \begin{bmatrix} C_1 & C_2 & C_3 & C_4 \end{bmatrix} / det(\mathbf{C})$$

with C_i being the following column vectors

$$C_1 = \begin{bmatrix} -(x_2y_3z_4 - x_2z_3y_4 - x_3y_2z_4 + x_3z_2y_4 + x_4y_2z_3 - x_4z_2y_3) \\ (y_3z_4 - z_3y_4 - y_2z_4 + z_2y_4 + y_2z_3 - z_2y_3) \\ -(x_3z_4 - z_3x_4 - x_2z_4 + z_2x_4 + x_2z_3 - z_2x_3) \\ (x_3y_4 - y_3x_4 - x_2y_4 + y_2x_4 + x_2y_3 - y_2x_3) \end{bmatrix}$$

$$C_2 = \begin{bmatrix} (x_1y_3z_4 - x_1z_3y_4 - x_3y_1z_4 + x_3z_1y_4 + x_4y_1z_3 - x_4z_1y_3) \\ -(y_3z_4 - z_3y_4 - y_1z_4 + z_1y_4 + y_1z_3 - z_1y_3) \\ (x_3z_4 - z_3x_4 - x_1z_4 + z_1x_4 + x_1z_3 - z_1x_3) \\ -(x_3y_4 - y_3x_4 - x_1y_4 + y_1x_4 + x_1y_3 - y_1x_3) \end{bmatrix}$$

$$C_3 = \begin{bmatrix} -(x_1y_2z_4 - x_1z_2y_4 - x_2y_1z_4 + x_2z_1y_4 + x_4y_1z_2 - x_4z_1y_2) \\ (y_2z_4 - z_2y_4 - y_1z_4 + z_1y_4 + y_1z_2 - z_1y_2) \\ -(x_2z_4 - z_2x_4 - x_1z_4 + z_1x_4 + x_1z_2 - z_1x_2) \\ (x_2y_4 - y_2x_4 - x_1y_4 + y_1x_4 + x_1y_2 - y_1x_2) \end{bmatrix}$$

$$C_4 = \begin{bmatrix} (x_1y_2z_3 - x_1z_2y_3 - x_2y_1z_3 + x_2z_1y_3 + x_3y_1z_2 - x_3z_1y_2) \\ -(y_2z_3 - z_2y_3 - y_1z_3 + z_1y_3 + y_1z_2 - z_1y_2) \\ (x_2z_3 - z_2x_3 - x_1z_3 + z_1x_3 + x_1z_2 - z_1x_2) \\ -(x_2y_3 - y_2x_3 - x_1y_3 + y_1x_3 + x_1y_2 - y_1x_2) \end{bmatrix}$$

In 3D the determinant is equal to six times the tetrahedron's volume. The determinant of C is

$$det(\mathbf{C}) = 6A = \begin{array}{l} x_2y_3z_4 - x_2z_3y_4 - x_3y_2z_4 + x_3z_2y_4 + x_4y_2z_3 - x_4z_2y_3 - x_1y_3z_4 \\ \cdots + x_1z_3y_4 + x_3y_1z_4 - x_3z_1y_4 - x_4y_1z_3 + x_4z_1y_3 + x_1y_2z_4 - x_1z_2y_4 \\ \cdots - x_2y_1z_4 + x_2z_1y_4 + x_4y_1z_2 - x_4z_1y_2 - x_1y_2z_3 + x_1z_2y_3 + x_2y_1z_3 \\ \cdots - x_2z_1y_3 - x_3y_1z_2 + x_3z_1y_2 \end{array}$$

Substitution of this into 2.17 yields the potential function over the element

$$U(x,y,z) = \begin{bmatrix} 1 & x & y & z \end{bmatrix} \begin{bmatrix} a \\ b \\ c \\ d \end{bmatrix} = \begin{bmatrix} 1 & x & y & z \end{bmatrix} \begin{bmatrix} c_{11} & c_{12} & c_{13} & c_{14} \\ c_{21} & c_{22} & c_{23} & c_{24} \\ c_{31} & c_{32} & c_{33} & c_{34} \\ c_{41} & c_{42} & c_{43} & c_{44} \end{bmatrix} \begin{bmatrix} U_1 \\ U_2 \\ U_3 \\ U_4 \end{bmatrix}$$

where c_{ij} are the elements of $\mathbf{C}$. This can be more easily written as a summation:

$$U(x,y,z) = \sum_{i=1}^{4} U_i \phi_i(x,y,z) \tag{2.19}$$

where the interpolation functions, $\phi_i(x,y,z)$ $i \in (1,2,3,4)$ are given by:

$$\phi_i = c_{1i} + c_{2i}x + c_{3i}y + c_{4i}z$$

which are explicitly:

$$\phi_1 = \frac{1}{6A} \left\{ \begin{array}{l} -(x_2y_3z_4 - x_2z_3y_4 - x_3y_2z_4 + x_3z_2y_4 + x_4y_2z_3 - x_4z_2y_3) \\ \cdots + (y_3z_4 - z_3y_4 - y_2z_4 + z_2y_4 + y_2z_3 - z_2y_3)x \\ \cdots - (x_3z_4 - z_3x_4 - x_2z_4 + z_2x_4 + x_2z_3 - z_2x_3)y \\ \cdots + (x_3y_4 - y_3x_4 - x_2y_4 + y_2x_4 + x_2y_3 - y_2x_3)z \end{array} \right\}$$

with the remaining interpolation functions, ϕ_2, ϕ_3, ϕ_4, following through cyclic interchange of subscripts.

These newly defined functions are interpolatory on the four vertices of the tetrahedron. Each function, ϕ_i is zero at all vertices except one where it's value is one:

$$\begin{aligned} \phi_i(x_j, y_j) &= 0 \quad i \neq j \\ &= 1 \quad i = j \end{aligned}$$

Equation 2.19 completely defines the potential within the tetrahedral element as a function of the values of the potential at the element's four nodes.

2.3.2 Method of Weighted Residuals (MWR)

There are several different methods used in weighted residuals including Collocation, Least Squares, and Galerkin with the latter method being the most common. Much of the material in the following section was interpreted from [69] and [106]. The development of the MWR starts with a discretization in which the field variable is represented as a linear combination of piecewise polynomial interpolation functions of limited support:

$$\tilde{u}(\vec{x}) = \sum_{i=1}^{N} u_i \phi_i(\vec{x}) \quad \text{where} \quad \phi_{\text{i}} = \begin{cases} 1 & \text{on vertex } i \\ 0 & \text{otherwise} \end{cases} \tag{2.20}$$

where ϕ_i are the interpolation functions and N is the number of nodes in the FEM. Equation 2.20 is general, however, in the case of linear interpolation functions in 2D, ϕ will turn out to be identical to equation 2.16. Since $\tilde{u}$ represents only a finite approximation of the potential, the Laplacian is not, in general, equal to zero due to the error introduced by using the approximating functions. The method of weighted residuals proceeds by deriving the weak form of the governing equation through the multiplication of Laplace's equation 2.2 by some arbitrary test function v and integration over the domain, Ω:

$$\int_{\Omega} v[\nabla \cdot (\sigma \nabla \tilde{u})] d\Omega = 0 \tag{2.21}$$

Here v is an arbitrary test function that weighs the residual such that it is zero in some weighted or average sense. The Galerkin method of weighted residuals differs from other MWR methods in the choice of weighing function. With the Galerkin method the test function v has the same form as the trial function $\tilde{u}$ in that it uses the same interpolation functions ϕ_i. In other words

$$v(\vec{x}) = \sum_{i=1}^{N} w_i \phi_i(\vec{x}) \tag{2.22}$$

where w_i are the coefficients that weigh the interpolation functions ϕ_i. The problem is to find the u_i that solve equation 2.21.

The "vector derivative identity" (the product rule for vectors) is:

$$\nabla \cdot (fA) = f(\nabla \cdot A) + \nabla f \cdot A \tag{2.23}$$

In terms of the variables in 2.21 the "vector derivative identity" is

$$[\nabla \cdot (v\sigma \nabla \tilde{u})] = \sigma \nabla \tilde{u} \cdot \nabla v + v \nabla \cdot (\sigma \nabla \tilde{u}) \tag{2.24}$$

Substitution of 2.24 into 2.21 yields

$$\int_{\Omega} [\nabla \cdot (v\sigma \nabla \tilde{u}) - \sigma \nabla \tilde{u} \cdot \nabla v] d\Omega = 0 \tag{2.25}$$

Rearranging gives

$$\int_{\Omega} \nabla \cdot (v\sigma \nabla \tilde{u})\, d\Omega = \int_{\Omega} \sigma \nabla \tilde{u} \cdot \nabla v\, d\Omega \tag{2.26}$$

Gauss' Theorem is the older name for the Divergence theorem which is a mathematical statement of the physical fact that, in the absence of the creation or destruction of matter, the density within a region of space can change only by having it flow into or away from the region through its boundary. Gauss' Theorem is valid in any dimension, however in 2D it is $\int_V \nabla \cdot F dV = \int_{\partial V} F dS$ where V is volume and S is surface area.

Invoking Gauss' Theorem on 2.26 permits the introduction of boundary conditions:

$$\int_{\partial\Omega} v\sigma \nabla \tilde{u} \cdot \hat{n}\, d\Gamma = \int_{\Omega} \sigma \nabla \tilde{u} \cdot \nabla v\, d\Omega \tag{2.27}$$

Note that $\nabla \phi \cdot \hat{n} = \frac{\partial \phi}{\partial \hat{n}}$ so 2.27 could also be written

$$\int_{\Omega} \sigma \nabla \tilde{u} \cdot \nabla v\, d\Omega = \int_{\partial\Omega} v\sigma \frac{\partial \tilde{u}}{\partial \hat{n}} d\Gamma \tag{2.28}$$

The boundary integral only needs to be carried out for elements underneath electrodes. The left side of 2.28 is for the entire mesh. When examined for a single triangular 2D element, k, the left side is

$$\int_{E_k} \sigma_k \nabla \tilde{u} \cdot \nabla v\, d\Omega \tag{2.29}$$

Substituting the definitions of the interpolating versions of v and u yields

$$\int_{E_k} \sigma_k \nabla \sum_{i=1}^{3} u_i \phi_i \cdot \nabla \sum_{i=1}^{3} w_j \tilde{u}_j\, d\Omega \tag{2.30}$$

If the conductivity, σ_k, is constant over a single element then the nodal voltages u_i, the coefficients for the weighing functions, and the summations can be moved outside of the integral:

$$\sigma_k \sum_{i=1}^{3} u_i \sum_{j=1}^{3} w_j \int_{E_k} \nabla \phi_i \cdot \nabla \phi_j\, d\Omega \tag{2.31}$$

It is common to break out the integral part of the equation as

$$S_{ij}^{k} = \int_{E_k} \nabla \phi_i \cdot \nabla \phi_j\, d\Omega \tag{2.32}$$

Allowing equation 2.31 to be rewritten as

$$\sigma_k \sum_{i=1}^{3} u_i \sum_{j=1}^{3} w_j S_{ik}^k \tag{2.33}$$

Thus each triangular element of the mesh produces a 3 by 3 matrix. In 3D this will be a 4 by 4 matrix.

The right side of equation 2.28 represents the boundary conditions. In terms of the interpolating functions the boundary conditions are:

$$\int_{\partial\Omega} v\sigma \frac{\partial \tilde{u}}{\partial \hat{n}} d\Gamma = \sigma_k \sum_{i=1}^{3} w_i \sum_{j=1}^{3} u_i \int_{\partial\Omega} \phi_i \nabla\phi_j \cdot \hat{n} d\Gamma \tag{2.34}$$

The ability to formulate solutions for individual elements before putting them together to represent the entire problem is an important advantage of the finite element method. For a single element of the FEM 2.27 becomes

$$\sigma_k \sum_{i=1}^{3} u_i \sum_{j=1}^{3} w_j S_{ik}^k = \sigma_k \sum_{i=1}^{3} w_i \sum_{j=1}^{3} u_i \int_{\partial\Omega} \phi_i \nabla\phi_j \cdot \hat{n} d\Gamma \tag{2.35}$$

Both sides can be divided through by the summation of the weighing function coefficients to yield:

$$\sigma_k \sum_{i=1}^{3} u_i \sum_{j=1}^{3} S_{ik}^k = \sigma_k \sum_{i=1}^{3} \sum_{j=1}^{3} u_i \int_{\partial\Omega} \phi_i \nabla\phi_j \cdot \hat{n} d\Gamma \tag{2.36}$$

In terms of the entire domain, the left side of 2.28 will be

$$\int_{\Omega} \sigma \nabla\tilde{u} \cdot \nabla\phi dV = \sum_{E=1}^{K} \sigma_k \sum_{i=1}^{3} \sum_{j=1}^{3} u_i S_{ij}^k \; i, j = 1, ...N \tag{2.37}$$

2.3.2.1 Calculating Local Matrices

The potential gradient within the element may be found from the linear interpolation equations 2.15 or 2.19 as

$$\nabla U = \sum_{i=1}^{3} U_i \nabla\phi_i \tag{2.38}$$

Taking the divergence of 2.38 yields:

$$\nabla \cdot \nabla U = \sum_{i=1}^{3} \sum_{j=1}^{3} U_i \int \nabla\phi_i \cdot \nabla\phi_j \, d\Gamma \, U_j$$

For convenience define matrix elements (local stiffness matrix)

$$S_{ij}^{(e)} = \int \nabla\phi_i \cdot \nabla\phi_j \, d\Gamma \tag{2.39}$$

where the superscript identifies the element. Equation 2.39 is recognizable as equation 2.32 and may be written in matrix quadratic form as

$$\nabla \cdot \nabla U = S^{(e)} U$$

The gradient of the linear interpolation functions, equation 2.16, becomes the vector:

$$\nabla \phi_i = \frac{1}{2A} \left(y_2 - y_3, x_3 - x_2 \right) \tag{2.40}$$

which, in terms of the local matrix for an element is the same as the matrices derived from the direct method. That is $S_{ij} = Y_{ij}$ with $\mathbf{Y}$ as in equation 2.7.

2.3.3 Impose Boundary Conditions

If the Gap model is used then the algebraic system of equations is identical to those of the direct method, as it must be. In terms of the derivation of MWR the Gap model boundary conditions are analytically contained in the right side of 2.28:

$$\int_{\Gamma} u\sigma \frac{\partial \tilde{u}}{\partial \hat{\mathbf{n}}} \, d\Gamma \tag{2.41}$$

Away from the electrodes where no current flows $\partial u / \partial \mathbf{n} = 0$. This mixed boundary value problem is well-posed, and the resulting currents are $I = \int_{E_l} \sigma \partial u / \partial \mathbf{n}$. With the Gap model current is injected between two nodes of the FEM. The boundary conditions are then:

$$\int_{\Gamma} u\sigma \frac{\partial \tilde{u}}{\partial \hat{\mathbf{n}}} \, d\Gamma = u_a I_a + u_b I_b \tag{2.42}$$

where I_a and I_b are injected current and u_a and u_b are the voltages at the current injection electrodes.

There are 3 other electrode models in the literature, Continuum, Shunt and Complete.

2.3.3.1 Continuum Model

The continuum model assumes that there are no electrodes and injected current j is a continuous function on the boundary of the medium. The current is a continuous function of the angle, θ, in the plane, that is

$$j\left(\theta\right) = C \cos\left(k\theta\right)$$

where C is constant. With experimental data it has been shown that this model underestimates the conductivities as much as 25% due to the fact that presence of electrodes is ignored [112].

2.3.3.2 Shunt Electrode Model

The Shunt Electrode Model [69] is a refinement of the Gap Electrode model in which the effect of perfectly conducting finite length electrodes is added. A complete mathematical statement of the shunt model is equation 2.2 along with the following boundary conditions:

$$\int_{E_\ell} \sigma \frac{\partial u}{\partial \hat{\mathrm{n}}} d\Gamma = I_\ell \quad \text{on } \ell = 1, ..., L \tag{2.43}$$

$$\frac{\partial u}{\partial \hat{\mathrm{n}}} = 0 \qquad \text{on } \Gamma' \tag{2.44}$$

$$u = U_\ell \qquad \text{on } \Gamma \tag{2.45}$$

where $\Gamma = \cup_\ell E_\ell$ and $\Gamma' = \partial\Omega - \Gamma$ on Γ. Equation 2.43 states that the net flux of the current density through the electrode contact surface is equal to the injected current. Equation 2.44 means that away from the electrodes no current flows. Equation 2.45 means that the voltage on each electrode, U_ℓ, is constant on electrodes. This is a mixed boundary problem that is well posed but seldom used.

2.3.3.3 Complete Electrode Model

In medical applications with electrodes applied to skin, and in phantom tanks with ionic solutions in contact with metal electrodes a contact impedance layer exists between the solution or skin and the electrode. This modifies the shunting effect so that the voltage under the electrode is no longer constant; the voltage is constant on the electrode because it is metallic (higher conductivity than the medium) however there is now a voltage drop across the contact impedance layer. The contact impedance z_ℓ could vary over the electrode but it is usually assumed to be constant. This electrode-skin contact impedance is high for the frequencies used in EIT, thus, the voltage drop across the contact impedance is large [72]. Ignoring this voltage drop introduces a large modeling error, which results in errors in the reconstructed conductivity. The complete electrode model includes the effect of the contact impedance and is accordingly the most accurate description of the physical situation [112]. This model is able to predict tank measurements within the accuracy of a data acquisition system [34]. Note that in the following it is assumed that the contact impedances z_ℓ are known and are not part of the inverse problem.

The Complete Electrode Model is defined by the Laplacian, Equation 2.2 and the following Boundary Conditions [69][112].

$$u + z_\ell \sigma \frac{\partial u}{\partial \hat{\mathbf{n}}} = U_\ell \quad \text{on } E_\ell, \ell = 1, 2, \ldots, L \tag{2.46}$$

$$\int_{E_\ell} \sigma \frac{\partial u}{\partial \hat{\mathbf{n}}} d\Gamma = I_\ell \qquad \ell = 1, 2, \ldots, L \tag{2.47}$$

$$\sigma \frac{\partial u}{\partial \hat{\mathbf{n}}} = 0 \qquad \text{on } d\Gamma \setminus \bigcup_{\ell=1}^{L} E_\ell \tag{2.48}$$

In these equations I_ℓ is the current sent to the ℓ^{th} electrode, E_ℓ denotes the part of Γ that corresponds to the ℓ^{th} electrode and U_ℓ is the constant potential on electrode ℓ. Equation 2.46 accounts for the electrode contact impedance which is characterized by z_ℓ. Equation 2.46 means that the measured voltages on the boundary consist of the voltage on the boundary plus the voltage dropped across the electrode impedance. The outward unit normal term, $\frac{\partial u}{\partial \hat{\mathbf{n}}}$, means that the contact impedance is only a factor for current passing across the electrode-skin boundary. Equation 2.47 says that the integral of the current density over the electrode is equal to the total current that flows to that electrode. Finally, equation 2.48 means that there is no current entering or leaving the object where there is no electrode (i.e. on the inter-electrode gap). The complete electrode model consists of equations 2.2 and 2.46-2.48 together with the conditions for conservation of charge:

$$\sum_{\ell=1}^{L} I_\ell = 0$$

and an arbitrary choice of a ground:

$$\sum_{\ell=1}^{L} V_\ell = 0$$

2.3.3.4 Numerical Implementation of CEM

The following section is based on material from [69],[93], and [114]. The CEM model of equations 2.46-2.48 can be formed numerically as

$$\mathbf{A}\mathbf{V}_c = \mathbf{I}_c \tag{2.49}$$

where $\mathbf{A}$ is the global conductance (also called stiffness) matrix, $\mathbf{I}_c$ contains the injected currents and $\mathbf{V}_c$ is the vector of voltages at the FEM nodes and the electrodes as follows:

$$\mathbf{A} = \begin{bmatrix} \mathbf{A}_{c1} + \mathbf{A}_{c2} & \mathbf{A}_e \\ \mathbf{A}_e^T & \mathbf{A}_d \end{bmatrix} \tag{2.50}$$

$\mathbf{V}_c = \begin{bmatrix} v \\ \mathbf{U} \end{bmatrix}$ $v \in N$, $\mathbf{U} \in L$ are the voltages on the, L, electrodes, and

$\mathbf{I}_c = \begin{bmatrix} \mathbf{0} \\ \mathbf{I} \end{bmatrix}$ $0 \in N$, $\mathbf{I} \in L$

In equation 2.50 $\mathbf{A}_{c1}$ is

$$\mathbf{A}_{c1}(i,j) = \int_{\Omega} \sigma \nabla\phi_i \nabla\phi_j dA \tag{2.51}$$

and represents equation 2.2. The integral is carried out over the area or volume of each element. Numerically this is the same as the matrix $\mathbf{Y}$ derived using the direct method in section 2.3.1. $\mathbf{A}_{c2}$ adds the effect of contact impedance to nodes situated underneath the electrodes:

$$\mathbf{A}_{c2}(i,j) = \sum_{l=1}^{L} \frac{1}{z_j} \int_{e_\ell} \phi_i \phi_j d\Gamma \tag{2.52}$$

In 2.50 component A_e is

$$\mathbf{A}_e(i,j) = -\frac{1}{z_j} \int_{e_\ell} \phi_i d\Gamma \quad i \in [1,N] \text{ and } j \in [1,L]$$

and adds the effect of the contact impedance to the nodes situated under the electrodes. Finally, component A_d is

$$\mathbf{A}_d(i,j) = \begin{cases} |e_\ell| \frac{1}{z_j} & \text{for } i,j \in [1,L] \\ 0 & \text{otherwise} \end{cases} \qquad |e_\ell| \text{ is the length of the electrode}$$

which connects the contact layer to the electrode. So matrix $\mathbf{A}$ is first assembled as though we were solving the natural boundary conditions (such as the gap-shunt electrode model) and augmented by the CEM blocks $\mathbf{A}_e$ and $\mathbf{A}_d$.

One additional constraint is required as potentials are only defined up to an added constant. This is manifested in the problem in that the matrix $\mathbf{A}$ is singular. One choice described in [112] is to change the basis used for the vectors $\mathbf{V}$ and $\mathbf{I}$ to a basis for the subspace S orthogonal to constants, while another choice is to "ground" an arbitrary vertex i by setting $\phi_i = 0$. The resulting solution $\mathbf{V}$ can then have any constant added to produce a different grounded point.

2.4 Algorithms to solve the Forward Model

The systems of equations 2.8 and 2.49 have the following special features [69][116]: The admittance matrix for the Gap electrode model, $\mathbf{Y}$, has dimension $N \times N$. For the CEM the matrix $\mathbf{A}$ has dimension $(N + L) \times (N + L)$. The matrices $\mathbf{A}$ and $\mathbf{Y}$ are sparse, the number of non-zeros in each row of the main block depends on the number of neighbouring vertices connected to any given vertex by an edge, they are symmetric and positive definite. Positive definiteness allows a matrix to be decomposed into two triangular factors using Cholesky factorization. With Cholesky factorization the matrix is expressed as the product of lower and upper triangular factors which are transposes of one another. The solution of the equations 2.8 and 2.49 is calculated by Cholesky factorization with back substitutions:

$$\mathbf{AV} = \mathbf{U}^T\mathbf{UV} = \mathbf{C} \tag{2.53}$$

by using a dummy variable:

$$\mathbf{U}^T\mathbf{q} = \mathbf{C} \tag{2.54}$$

solving with respect to $\mathbf{q}$ then substituting $\mathbf{q}$ to calculate $\mathbf{V}$ by

$$\mathbf{UV} = \mathbf{q} \tag{2.55}$$

The factorization process is essentially Gaussian elimination and has a computational cost $O(n^3)$ [69]. For large 3D systems direct methods can be expensive and iterative methods such as the Conjugate Gradient (CG) method may be required where each iteration has computational cost $O(n^2k)$ and requires fewer than n iterations to converge. The CG method searches for a minimum of the functional by taking conjugate search directions for every iteration step and requires the computation of the gradient only, instead of the full second derivative. Different choices for finding the minimum along a search direction, such as the inexact line search algorithm, exist [69].

2.5 Variations on the Forward Model

2.5.1 Current Patterns

A variety of protocols for injecting current and collecting measurements have been proposed over the years. With some minor exceptions protocols can be categorized as either pair drive or multiple drive [23]. Pair drive scanners have a single current source whose terminals are sequentially connected to the driving electrode pairs with voltages measured between the remaining pairs of electrodes. The current source is then switched to another pair of electrodes and the voltage measurement process repeated until a complete set of measurements has been collected. Multiple drive systems are more complex and expensive but have the ability to drive current in more than two electrodes at a time, while the obvious advantage of a pair drive system is that only one current source is needed.

Number of available measurements. There are $N(N-1)$ ways to connect a pair of leads to a set of N electrodes, including reversal of electrodes. When using alternating currents, as in EIT, this is reduced to $N(N-1)/2$. It is common in pair drive systems to avoid using measurements that involve one of the driving electrodes. This is often referred to as the four electrode or *tetrapolar* measurement scheme. Once a pair of driving electrodes

is selected, measurements are taken using only the remaining $N-2$ electrodes. This allows $N-3$ possible voltage measurements to be made using a single reference. The total number of measurements possible is therefore $N(N-1)(N-3)/2$. For $n = 16$ this is 1560 individual measurements. Any combination of electrode pair voltages can be reconstructed from this basic set. This number of measurements is valid for any electrode spatial arrangement such as 2D tomographic, 3D, and planar. Of these possible pairs only a subset are typically used. The typical subsets used have been dictated in the past more by timing and system design configurations more than anything else.

The next sections discuss the most well known current injection patterns for 2D configurations. In 2D configurations the electrodes define a boundary encompassing the domain of interest. Here there are as many electrodes as there are electrode pairs, with each pair defined as being the neighbours along the boundary path. The electrodes in this configuration also define a plane of intersection with the object being imaged.

2.5.1.1 Adjacent Pattern

The adjacent drive method [16], also known as the neighbouring method, is the most common pair drive protocol. As can be seen in figure 2.2, current is applied through two adjacent electrodes and the voltages measured from successive pairs of adjacent electrodes. Current is then applied through the next pair of electrodes and the voltage measurements repeated. The procedure is repeated until each possible pair of adjacent electrodes has been used to inject current.

The adjacent measurement strategy provides N^2 measurements, where N is the number of electrodes. However to avoid the problem of unknown contact impedance, the voltage is not measured at a current injecting electrode thus the number of measurements is reduced to $N(N-3)$. The four-electrode reciprocity theorem [38][55] states that for any measurement set the mutual impedance is preserved under an interchange of injection and measurement pairs. Therefore only $N(N-1)/2$ of the measurements are independent. However, it is common to use all $N(N-3)$ measurements in most reconstruction algorithms. Thus a 16 electrode system will produce 208 measurements of which 104 are independent but all 208 are used in the reconstruction algorithm.

The adjacent strategy requires minimal hardware to implement. With the adjacent strategy current is driven mainly in the outer region of the imaged object. The current density is highest between the injecting electrodes, and decreases rapidly as a function of distance. The method is therefore very sensitive to conductivity contrasts near the boundary and insensitive to central contrasts. It is also sensitive to perturbations in the boundary shape of the object, in the positioning of the electrodes and is quite sensitive to measurement error and noise [43].

A feature of adjacent drive protocol is that on a two dimensional domain the adjacent voltage measurements are all positive. This can be seen in figure 2.8(a) which shows that the potential is monotonically decreasing from source to sink. The resulting measurements will have a 'U' shaped graph for each drive as shown in figure 2.8(b).

2.5.1.2 Opposite Pattern

The opposite or polar drive pattern [14], which is commonly used in brain EIT [20], applies current through electrodes that are 180° apart while voltage differences are measured on the remaining electrodes. There are various ways to collect the voltage measurements. The most common appears to be to use the electrode adjacent to the current-injecting electrode

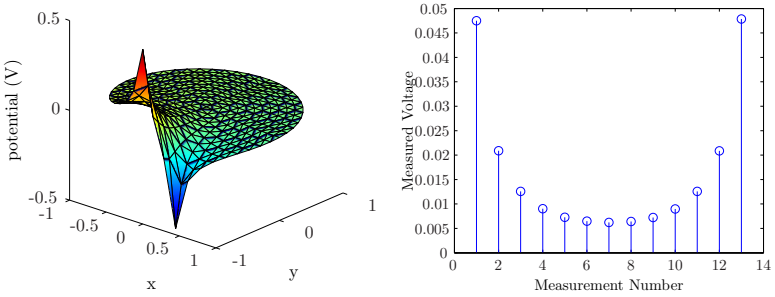

(a) *3D spatial plot of the potential field of a homogenous disk with current injected between two adjacent electrodes.*

(b) *The 13 measurements for a single drive pair are all positive quantities.*

Figure 2.8: *Nodal and Measured voltages for a homogenous disk of conductive material with adjacent drive.*

as a voltage reference and measure the voltages between the reference and the remaining non-current electrodes, except from the current injecting electrodes. With a 16 electrode machine this will provide 13 voltage measurements per injection. The next set of 13 voltage measurements are obtained by shifting the current injecting pair. This is done 8 times, since injecting current between electrodes (1,9) will produce identical data as injecting current between electrodes (9,1) under the assumption of isotropic medium. Thus with 16 electrodes the opposite method yields $8 \times 13 = 104$ measurements of which half are independent. Thus the opposite strategy suffers from the disadvantage that for the same number of electrodes, the number of available current injections that can be applied is less than for the adjacent strategy.

The opposite drive method offers a better distribution of the sensitivity, as the current travels with greater uniformity through the imaged body. Therefore compared to the adjacent strategy, the opposite strategy is less sensitive to conductivity changes at the boundary. The ideal angular position of the driving electrodes has been studied in [103] for a circular object with a circular inclusion of known position and radius. The larger and deeper the expected anomaly is, the larger the angular separation of the electrodes should be. Thus the opposite strategy optimizes the sensitivity for a contrast in the centre of the imaged object.

2.5.1.3 Cross Pattern

The cross or diagonal drive pattern [73] is rarely used. In the cross method, adjacent electrodes are selected as current and voltage references. Current is first injected between electrodes 16 and 2, while 13 voltage measurements are taken using electrode 1 as the reference against the other 13 electrodes. Next current is applied to electrodes 16 and 4 while 13 voltage measurements are taken using electrode 1 as the reference. This is repeated for currents injected between electrodes (16 ,8), (16, 10), (16,12), (16, 14). Since each of these injections produces 13 measurements the sequence produces $7 \times 134 = 91$ measurements for a 16 electrode scanner. The entire sequence is repeated once more, with the reference electrodes changed to electrodes 3 and 2. Thus current is applied between electrode 3 and $(5, 7, 9, 11, ..., 1)$ with voltage measured at the other 13 electrodes with electrode 2 as a reference. This produces a further 91 measurements for a total of 182

measurements of which only 104 are independent. The cross method does not have as good a sensitivity in the periphery as does the adjacent method, but has better sensitivity over the entire region.

2.5.1.4 Optimal Patterns

There have been several attempts to explore optimal patterns in EIT. The problem of optimizing the drive patterns in EIT was first considered by Seagar [69] who calculated the optimal placing of a pair of point drive electrodes on a disk to maximize the voltage differences between the measurement of a homogeneous background and an offset circular anomaly.

Gisser *et al* [57] studied the problem of optimizing measurements in terms of distinguishability. Isaacson [76] defined distinguishability δ as the ability of a pattern of currents to distinguish between two conductivities. Two conductivities σ_1 and σ_1 are distinguishable in the mean-square sense by measurements of precision ϵ if there is a current j for which

$$\delta = \delta(j) = \frac{\|R(\sigma) - R(\tau)\|}{\|j\|} \geq \varepsilon \tag{2.56}$$

where $R(\sigma)$ denotes a nonlinear functional associated with the resultant boundary voltage.

In [42] Demidenko *et al* argue that although the distinguishability criterion of Isaacson [76] seems intuitively appealing it is not directly associated with the quality of the image reconstruction. Instead of the distinguishability criterion they propose a statistical criterion for optimal patterns in planar circular electrical impedance tomography that lead to the best estimation of electromagnetic properties. A current (voltage) pattern is considered optimal if it yields the minimum total variance of the resistance (conductance) matrix.

Optimal Patterns: Trigonometric Pattern An example of an optimal pattern is the trigonometric current pattern [76] which is optimal for a centered circular contrasts located in a larger circular object. In this pattern current is injected on all electrodes and voltages are measured on all electrodes.

$$I_l^k = \left\{ \begin{array}{cc} \cos(k\psi) & l = 1, 2..., 16, k = 1, ..., 8 \\ \sin((k-16)\psi) & l = 1, 2, ..., 16, k = 9, ..., 16 \end{array} \right\} \text{where } \psi = 2\pi l/16$$

The obvious disadvantage of this method is that current drivers are needed for each electrode and the unknown contact impedance will have an effect on the reconstruction.

The trigonometric pattern is optimal in the sense of satisfying Isaacsons [76] distinguishability criterion. However, Demidenko *et al* [42] show that the trigonometric patterns are also a special case of their optimal statistical patterns.

Optimal Patterns: Problems Researchers have pointed out some issues with optimal patterns. In [23] Borsic notes that the use of multiple drive optimal patterns does not necessarily guarantee a better accuracy over pair drive systems. With the pair drive system the stimuli are generated by a single driver and are repeatable through the whole set of patterns. A gain error in such a device will affect all the measurements equally and manifest itself as an insignificant scaling factor in the reconstruction. The use of multiple current sources requires a precise matching of the devices, otherwise unmatched gains will distort the applied patterns, and cause artefacts in the reconstruction [59] [60].

Eyüboglu and Pilkington [47] argue that the definition of optimality in 2.56 is not based on practical considerations. For example in a medical application safety regulations restrict

the total amount of applied current. In this environment the distinguishability should be maximized with respect to this constraint. This is furthered by Lionheart in [69] where he points out that the maximum Ohmic power dissipated in the body must be limited.

2.5.1.5 Other Patterns

In [99] Polydorides and McCann described a novel "scrolling" current injection pattern using a single current source instrument. The current source is simultaneously connected to several neighbouring electrodes while voltages are measured between single electrodes. The current injection electrodes are then "scrolled" around the object by connecting new electrodes at one side and leaving some free at the other. Voltage measurements are repeated for each new configuration.

2.5.1.6 Compound Electrodes

In [72] Hua *et al* introduced compound electrodes comprised of a larger outer electrode with a small, electrode in the centre. Current is injected in the larger outer electrode, and voltage us measured from a small inner electrode. They show that using compound electrodes can make reconstructions less dependent on the contact impedance value thus minimizing its effects.

Chapter 3

Reconstruction

The process of calculating an image from the EIT signal is called reconstruction. Reconstruction algorithms can be classified into several categories each of which is intended to image a different aspect of impedance:

1. *Time Difference* imaging systems are used to generate images of the change in impedance over time. This method is discussed in the next section.

2. Absolute or *static* systems are used to obtain images of the absolute impedance distribution. This method is discussed in a subsequent section.

3. Multiple frequency imaging systems are used to construct images of frequency-dependent impedance changes. Griffiths and Zhang [61] describe imaging the difference in impedance between two frequencies. Brown *et al* [28] discuss injecting current at many frequencies and deriving parameters, such as Cole-Cole parameters, from measurements taken from 9.6 kHz to 1.2 MHz.

4. Dynamic imaging systems are used to reconstruct fast conductivity changes. In these systems the conductivity is assumed to change rapidly compared to the acquisition interval between signals [112] but slow with respect to the acquisition period of a frame of data. In another example Seppänen applied dynamic methods to imaging fast flowing liquids transporting resistive objects [104][105] while Vauhkonen used the method to image cardiac function. Dynamic imaging is sometimes known by other names, for example the Goettingen group calls it functional imaging [49].

3.1 Difference Imaging

The aim of difference imaging is to reconstruct the change in impedance or conductivity that occurs over some time interval. A data set $\mathbf{v}_1$ is acquired at a time t_1 and a second data set $\mathbf{v}_2$ is acquired at a later time t_2. The algorithm then calculates the change in conductivity from time t_1 to time t_2. The method is commonly used for imaging temporal phenomena in medical applications, such as impedance changes during respiration [5][4]. Difference imaging is widely understood to improve reconstructed image stability in the presence of problems such as unknown contact impedance, inaccurate electrode positions, poorly known boundary shape, non linearity, and the use of 2D approximations for 3D electrical fields [18][87].

The calculation of the change in conductivity is performed using a linear approximation operator. In the case where the full non-linear solution is desired the non-linear problem

is solved iteratively with the linearized operator being updated and re-applied at each iteration. However most difference image applications assume that the conductivity change over the time interval is small so that a single step with the linearized operator is sufficient to produce a solution that is "good enough." The linear operator is developed as a Jacobian or sensitivity matrix. On a model with E elements and M boundary measurements the Jacobian is a $M \times E$ matrix. The Jacobian matrix is calculated column by column with the i^{th} column describing the effect of the change in conductivity of the i^{th} element on the signal, $\mathbf{z}$ measured between electrode pairs.

3.2 Jacobian Derivation

In section 2.1.2 both static and difference image reconstructions were modelled as $\hat{\mathbf{x}} = B\mathbf{z}$. For difference imaging $\hat{\mathbf{x}} = \Delta\boldsymbol{\sigma} = \boldsymbol{\sigma_2} - \boldsymbol{\sigma_1}$ is the change in a finite element conductivity distribution due to a change in difference signal, $\mathbf{z} = \mathbf{v_2} - \mathbf{v_1}$, over a time interval (t_1, t_2). By convention the signal at t_1 is considered to be the *reference* frame and the signal at t_2 is the *data* frame. Since $\boldsymbol{\sigma}_1$ is unknown, $\hat{\mathbf{x}}$ is interpreted as the change in conductivity with respect to the unknown initial conductivity $\mathbf{x} = \boldsymbol{\Delta\sigma}$.

The Jacobian for a linearized forward problem is developed as follows using the notation of difference imaging: Construct a matrix $\mathbf{H}$ such that

$$\mathbf{z} = \mathbf{Hx} + \mathbf{n} \tag{3.1}$$

where $\mathbf{H}$ is the Jacobian or sensitivity matrix and $\mathbf{n}$ is the measurement system noise, assumed to be uncorrelated additive white Gaussian (AWGN). Each element i, j, of $\mathbf{H}$ is calculated as $\mathbf{H}_{ij} = \left.\frac{\partial z_i}{\partial x_j}\right|_{\sigma_0}$ and relates a small change in the i^{th} difference measurement to a small change in the conductivity of j^{th} element [4]. $\mathbf{H}$ is a function of the FEM, the current injection pattern, and the background conductivity. A homogenous background conductivity with $\boldsymbol{\sigma}_0 = \mathbf{1}$ for each of the elements is used.

In order to calculate the linear approximation matrix, $\mathbf{H}$, the signal

$$\mathbf{z} = \mathbf{v_2} - \mathbf{v_1} \tag{3.2}$$

is expressed in terms of the forward model as $\mathbf{z} = T[\mathbf{V}(\boldsymbol{\sigma}_2)] - T[\mathbf{V}(\boldsymbol{\sigma}_1)]$. $T[]$ is an extraction operator that produces the measurements between electrodes from the nodal voltage matrix $\mathbf{V}$. Under the assumption that the conductivity changes by only a small amount between the two times we can use $\boldsymbol{\sigma}_1 = \boldsymbol{\sigma}$ and $\boldsymbol{\sigma}_2 = \boldsymbol{\sigma} + \Delta\boldsymbol{\sigma}$ which gives $\mathbf{z} = T\left[\mathbf{V}(\boldsymbol{\sigma}) - \mathbf{V}(\boldsymbol{\sigma} + \Delta\boldsymbol{\sigma})\right]$. Further algebraic manipulation gives

$$\mathbf{z} = T\left[-\frac{\mathbf{V}(\boldsymbol{\sigma} + \Delta\boldsymbol{\sigma}) - \mathbf{V}(\boldsymbol{\sigma})}{\Delta\boldsymbol{\sigma}}\Delta\boldsymbol{\sigma}\right]$$

In the limit as $\Delta\boldsymbol{\sigma} \to 0$:

$$\lim_{\Delta\boldsymbol{\sigma}\to 0} \frac{\mathbf{V}(\boldsymbol{\sigma} + \Delta\boldsymbol{\sigma}) - \mathbf{V}(\boldsymbol{\sigma})}{\Delta\boldsymbol{\sigma}} = \frac{\partial\mathbf{V}(\boldsymbol{\sigma})}{\partial\boldsymbol{\sigma}}$$

Neglecting noise, this allows us to write the linearized form, equation 3.1, as

$$\mathbf{z} = T\left[-\frac{\partial\mathbf{V}(\boldsymbol{\sigma})}{\partial\boldsymbol{\sigma}}\right]\Delta\boldsymbol{\sigma}$$

where the Jacobian is

$$\mathbf{H} = T\left[-\frac{\partial \mathbf{V}(\boldsymbol{\sigma})}{\partial \boldsymbol{\sigma}}\right]$$

In terms of the Finite Element Model

$$\frac{\partial \mathbf{V}(\boldsymbol{\sigma})}{\partial \boldsymbol{\sigma}} = \frac{\partial}{\partial \boldsymbol{\sigma}}\left(\mathbf{Y}^{-1}(\boldsymbol{\sigma})\right) I$$

> Derivative of an inverse matrix: Assume that $\mathbf{A}$ an invertible matrix dependent on a parameter t and differentiable with respect to t. Then $\frac{\partial}{\partial t}\left(\mathbf{A}^{-1}\right) = -\mathbf{A}^{-1}\frac{\partial \mathbf{A}}{\partial t}\mathbf{A}^{-1}$

Invoking the chain rule provides the final form of the Jacobian in terms of the FEM which can be used as the basis for an algorithm to calculate the Jacobian matrix.

$$\mathbf{H} = T\left[-\frac{\partial}{\partial \boldsymbol{\sigma}}\mathbf{Y}^{-1}(\boldsymbol{\sigma})I\right] = T\left[\mathbf{Y}^{-1}(\boldsymbol{\sigma})\frac{\partial}{\partial \boldsymbol{\sigma}}\mathbf{Y}(\boldsymbol{\sigma})\mathbf{Y}^{-1}(\boldsymbol{\sigma})I\right]$$

The only derivative that must be calculated is the derivative of the stiffness matrix:

$$\frac{\partial}{\partial \boldsymbol{\sigma}}\left(\mathbf{Y}^{-1}(\boldsymbol{\sigma})\right)$$

With linear basis functions the derivative is a constant for matrix elements of the given element and zero elsewhere. The resulting answer for each operation is another vector representing the change in the M voltages due to a small change in $\boldsymbol{\sigma}_i$

$$\frac{\partial}{\partial \boldsymbol{\sigma}_i}\left(\mathbf{Y}^{-1}(\boldsymbol{\sigma})\right) i \in E$$

The solution is organized in columns of length M with each column being $\frac{\partial}{\partial \boldsymbol{\sigma}_i}\left(\mathbf{Y}^{-1}(\boldsymbol{\sigma})\right)$. Thus $\mathbf{H}$ is $M \times E$.

The calculation of the Jacobian algorithm has historically been done following the *standard method* [114][116]. However a more efficient method to calculate the Jacobian involves the concept of *measurement fields* [26]. The measurement fields are defined as the fields that would have been developed if currents were injected from the measurement electrodes. If we denote $\nabla\Phi$ as the gradient of the current fields obtained by normal forward solution and $\nabla\Psi$ as the gradient of the measurement fields then the i^{th} column of the Jacobian corresponding to the i^{th} element is given by the dot product of the two fields integrated over each mesh element as:

$$\frac{\partial U_\ell^k}{\partial \sigma_i} = -\int_i \nabla\Phi \cdot \nabla\Psi \tag{3.3}$$

In [98] Polydorides describes an implementation of this product that is currently the most computationally efficient way to calculate the Jacobian.

3.2.1 Naïve Least Squares Solutions

The naïve approach to solving the linearized problem, equation 3.1, for $\mathbf{x}$ is to find the least squares solution which minimizes $\|\mathbf{Hx} - \mathbf{z}\|$. This is found through the generalized least squares solution

$$\hat{\mathbf{x}} = (\mathbf{H}^T\mathbf{H})^{-1}\mathbf{H}^T\mathbf{z} \tag{3.4}$$

Unfortunately the equation cannot be solved this way because $\mathbf{H}^T\mathbf{H}$ is rank deficient and ill-conditioned. An ill-conditioned problem is one with the property that a small perturbation of the input data leads to a large change in the output, and even if the solution exists and it is unique it can be completely corrupted by a small error in the data or by noise.

3.2.2 Ill Posed Problems

In 1902 Jacques Hadamard classified all mathematical problems as either "well-posed" or "ill-posed" [63]. The solution to a well-posed problem is unique and has a solution that depends continuously on the data. In other words, for a problem to be well posed a solution must exist, the solution must be unique, and small changes in the data must not result in a large change in the solution. A problem is ill-posed if at least one of the three conditions (existence, uniqueness, stability) is not satisfied.

From a practical point of view violation of the first condition, existence of a solution, is not a concern. Existence can be usually be enforced by relaxing the notion of a solution to that of an approximate solution through regularization. Violation of solution uniqueness is more serious in that the existence of multiple solutions requires some other criteria from which to select one of the solutions. For example one could obtain a unique solution by preferring the solution of smallest norm or by adding some other additional information to the problem. Lack of stability is the most onerous problem. A problem whose solution does not depend continuously on the data will lead to an unstable numerical solution. In terms of EIT this means that the inverse solution will be dominated by noise unless additional conditions are imposed.

Strictly speaking ill-posed problems can only exist in the continuous domain in that, under the assumption of infinite precision arithmetic, the discrete problem $\mathbf{z} = \mathbf{Hx}$ is never ill-posed [Hansen 94]. However with finite precision arithmetic the discretization of an ill-posed problem leads to a numerical problem that is ill-conditioned. The ill-conditioning of a problem is defined by condition number of its matrix. To define the condition number requires an understanding of the Singular Value Decomposition (SVD) of a matrix. Detailed theory and examples of linear ill-posed problems can be found in [117], [10] and [63].

3.2.3 SVD

The singular value decomposition is a way of factoring a matrix that does not require the matrix to be either symmetric or have full rank. The SVD has many properties some of which are useful in discussing inverse problem characteristics and solutions [65]. Let $\mathbf{A} \in \Re^{m\times n}$ be a rectangular matrix with $m \geq n$. Then the SVD of $\mathbf{A}$ is a decomposition of the form

$$\mathbf{A} = \mathbf{U}\Sigma\mathbf{V}^T = \sum_{i=1}^{n} \mathbf{u}_i \sigma_i \mathbf{v}_i^T \tag{3.5}$$

where $\mathbf{U} = (\mathbf{u}_1, ..., \mathbf{u}_n)$ and $\mathbf{V} = (\mathbf{v}_1, ..., \mathbf{v}_n)$ are matrices with orthonormal columns, $\mathbf{U}^T\mathbf{U} = \mathbf{V}^T\mathbf{V} = \mathbf{I}_n$, and where $\Sigma = diag\,(\sigma_1, ..., \sigma_n)$ has non-negative diagonal elements, which by convention, are arranged in non-increasing order such that

$$\sigma_1 \geq ... \geq \sigma_n \geq 0$$

The numbers σ_i are the *singular values* of $\mathbf{A}$ while $\mathbf{u}$ and $\mathbf{v}$ are, respectively, the left and right *singular vectors* of $\mathbf{A}$. The condition number of $\mathbf{A}$ is equal to the ratio σ_1/σ_n.

The condition number of a matrix is relative, as it is related to the precision level of the computations and is a function of the size of the problem [37]. A problem with a low condition number is said to be well-conditioned, while a problem with a high condition number is said to be ill-conditioned.

In [65] Hansen discusses two observations concerning the singular values of discrete ill-conditioned matrices derived from practical applications. By plotting the singular values of an ill-posed matrix, as in figure 3.1, one will observe that:

1. The singular values σ_i decay gradually to zero with no particular gap in the spectrum. An increase of the dimensions of $\mathbf{A}$ will increase the number of small singular values.

2. The left and right singular vectors $\mathbf{u}_i$ and $\mathbf{v}_i$ tend to have more sign changes in their elements as the index i increases, i.e., as σ_i decreases.

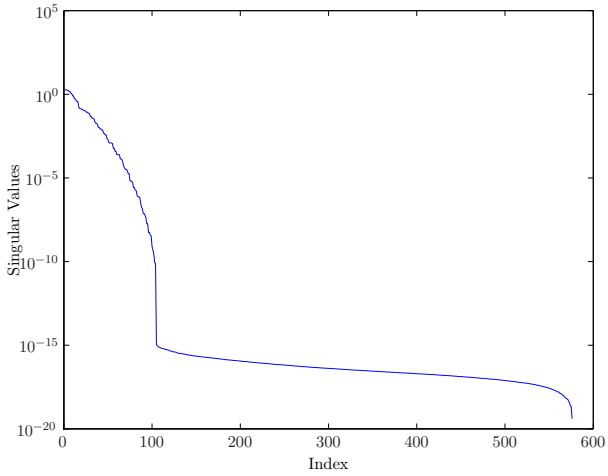

Figure 3.1: *Singular Values of* $\mathbf{H}^T\mathbf{H}$ *for an EIT example.*

The following material is taken from [65] which is one of the better descriptions of SVD. To see how the SVD gives insight into the ill-conditioning of $\mathbf{A}$, consider the following relations which follow directly from equation 3.5:

$$\left.\begin{array}{rcl} \mathbf{A}\mathbf{v}_i & = & \sigma_i \mathbf{u}_i \\ \|\mathbf{A}\mathbf{v}_i\|_2 & = & \sigma_i \end{array}\right\} \; i = 1, ..., n$$

A small singular value σ_i, compared to $\|\mathbf{A}\mathbf{v}_i\|_2 = \sigma_i$, means that there exists a certain linear combination of the columns of $\mathbf{A}$, characterized by the elements of the right singular vector $\mathbf{v}_i$, such that $\|\mathbf{A}\mathbf{v}_i\|_2$ is small. In other words, one or more small σ_i implies that $\mathbf{A}$ is nearly rank deficient, and the vectors $\mathbf{v}_i$ associated with the small σ_i are numerical null-vectors of $\mathbf{A}$. From this and the characteristic features of $\mathbf{A}$ we conclude that the matrix in a discrete ill-posed problem is always highly ill-conditioned, and its numerical null-space is spanned by vectors with many sign changes. The SVD also gives important insight into another aspect of discrete ill-posed problems, namely the smoothing effect typically associated with the measurement process. As σ_i decreases, the singular vectors $\mathbf{u}_i$ and $\mathbf{v}_i$ contain higher and higher frequency components. Consider now the mapping $\mathbf{A}\mathbf{x}$ of an arbitrary vector $\mathbf{x}$. Using the SVD, we get $\mathbf{x} = \sum_{i=1}^{n} (\mathbf{v}_i^T\mathbf{x})\mathbf{v}_i$ and

$$\mathbf{A}\mathbf{x} = \sum_{i=1}^{n} \sigma_i \left(\mathbf{v}_i^T\mathbf{x}\right) \mathbf{u}_i \tag{3.6}$$

This shows that due to the multiplication with the σ_i the high-frequency components of $\mathbf{x}$ are more damped in $\mathbf{Ax}$ than then low-frequency components. The inverse problem, that of computing $\mathbf{x}$ from $\mathbf{Ax} = \mathbf{b}$ has the form

$$\hat{\mathbf{x}} = \mathbf{A}^{-1}\mathbf{b} = \sum_{i=1}^{n} \frac{\left(\mathbf{u}_i^T \mathbf{b}\right) \mathbf{v}_i}{\sigma_i}$$

which clearly shows that the high-frequency oscillations in $\mathbf{b}$ will be amplified by the small singular values.

In terms of EIT reconstruction the noise in the data will be amplified by the inversion of the small singular values. Consequently the solution to equation 3.4 will be dominated by the noise in the signal. To overcome the ill-conditioning of $\mathbf{H}^T\mathbf{H}$ requires the use of regularization techniques. These techniques generally involve either truncating or filtering the singular values corresponding to the singular vectors with high frequency components.

3.2.4 Regularization

A regularization method, of which there are a wide variety, is often formally defined as an inversion method depending on a single real parameter $\lambda \geq 0$, which yields a family of approximate solutions [81]. Discrete regularization techniques include truncated singular value decomposition, maximum entropy, and a number of generalized least squares schemes including Twomey and Tikhonov regularization methods[37]. All of these methods attempt to reduce the effects of solving an ill-conditioned system by restoring continuity of the solution on the data [37].

The most widely referenced regularization method is the Tikhonov or Tikhonov-Phillips method. With Tikhonov regularization additional information about the solution, commonly referred to as prior information, is incorporated into the solution as an additional term in the least squares minimization. That is rather than minimize $\|\mathbf{Hx} - \mathbf{z}\|$ one minimizes an expression of the form:

$$\hat{\mathbf{x}} = \arg\min_{\mathbf{x}} \left\{ \|\mathbf{Hx} - \mathbf{z}\|^2 + \lambda^2 \|\mathbf{Rx}\|^2 \right\} \tag{3.7}$$

Here $\mathbf{R}$ is a regularization matrix that is often diagonal or banded diagonal and the expression $\lambda^2 \|\mathbf{Rx}\|^2$ represents some prior information about the conductivity. This is a quadratic minimization that is guaranteed to have a unique solution for $\lambda > 0$. The most often used regularization matrices in EIT are the identity matrix and the matrices corresponding to the first and second difference operators [114]. The corresponding implied prior assumptions when these matrices are used are that $\mathbf{x}$ is either small, slowly changing or smooth, respectively. Classic Tikhonov regularization refers to the case where $\mathbf{R} = \mathbf{I}$, however the term Tikhonov is often applied to any solution of equation 3.7 regardless of the choice of $\mathbf{R}$. The solution to equation 3.7 is calculated from the regularized inverse

$$\hat{\mathbf{x}} = (\mathbf{H^T H} + \lambda^2 \mathbf{R}^T \mathbf{R})^{-1} \mathbf{H^T z} = \mathbf{Bz} \tag{3.8}$$

Here $\mathbf{B}$ is the symbol used for the regularized linearized reconstruction operator of equation 2.1. Equation 3.8 is a linear equation which must be solved iteratively for the non-linear solution [68]. The regularized inverse has two important properties:

1. For large enough λ the regularized solution, $\hat{\mathbf{x}}(\lambda)$, is stable in the face of perturbations or noise in the data (unlike the generalized solution) and,

2. As λ goes to zero, the un-regularized generalized solution, which is dominated by noise, is recovered: $\hat{\mathbf{x}}(\lambda) \rightarrow \mathbf{x}$ as$\lambda \rightarrow 0$.

The parameter λ is called the "regularization parameter" or "hyperparameter" and controls the trade-off between solution stability and nearness of the regularized solution [4], $\hat{\mathbf{x}}(\lambda)$, to the un-regularized solution, $\mathbf{x}$. This can be understood as the approximation error in the absence of measurement noise and the discretization noise due to finite precision arithmetic. Chapter 4 of this work explores hyperparameter selection methods in detail.

Equation 3.8 is the most general form of the reconstruction model for EIT. Most EIT reconstruction algorithms can be built from this framework. The MAP Regularized Inverse Model of the next section is one such example.

In terms of the SVD the effect of Tikhonov regularization with $\mathbf{R} = \mathbf{I}$ is that the singular values are filtered as follows [63]:

$$\hat{\mathbf{x}} = \mathbf{A}^{-1}\mathbf{b} = \sum_{i=1}^{n} f_i \frac{\left(\mathbf{u}_i^T \mathbf{b}\right) \mathbf{v}_i}{\sigma_i} \tag{3.9}$$

with *filter factors*

$$f_i = \frac{\sigma_i^2}{\sigma_i^2 + \lambda^2}$$

This filter function decays smoothly from $f_1 \approx 1$ for $\sigma_i \gg \lambda$ to $f_1 \approx 0$ for $\sigma_i \ll \lambda$. In other words the right singular vectors with singular values smaller than λ are effectively filtered out. The Tikhonov filter function is structurally identical to the Wiener filter, which is the optimal filter to separate noise of spectral density λ^2 from a signal of spectral density σ_i^2 [81].

3.3 Static Imaging

Static reconstruction in EIT has been proposed by various groups [128][35][123]. The basic technique is to use a modified Gauss-Newton algorithm with Tikhonov style regularization. With such techniques an error function f is defined such that

$$f(\boldsymbol{\sigma}) = \tfrac{1}{2}\left(\left\|T[\mathbf{V}(\boldsymbol{\sigma})] - \mathbf{v}_{measured}\right\|^2 + \lambda^2 \left\|\mathbf{R}(\boldsymbol{\sigma} - \boldsymbol{\sigma_0})\right\|^2\right) \tag{3.10}$$

where $\mathbf{v}_{measured}$ is a vector of voltage measurements from the physical medium, $\boldsymbol{\sigma_0}$ is the initial estimate of the background conductivity, and $\mathbf{V}(\boldsymbol{\sigma})$ is the forward operator which simulates the voltage measurements from a medium with conductivity distribution $\boldsymbol{\sigma}$. The desired reconstructed conductivity distribution is the vector $\boldsymbol{\sigma}$ that minimizes f.

The non-linear solution of equation 3.10 is solved iteratively using a linearized step at each iteration. Figure 3.2 is a functional diagram of one such process [3]. In the figure a set of currents is injected into the medium and the resulting voltages , $\boldsymbol{v}_{measured}$, recorded. This data is compared to voltages, $\mathbf{v}_{simulated} = T[V(\boldsymbol{\sigma})]$, generated by simulating the same process (current injection and voltage measurement) on a Finite Element Model (FEM) of the medium. Initially, the medium is assumed to be homogeneous. If the simulated data approximates the measured data by some measure then the conductivity of the model is assumed to approximate the conductivity of the medium and the problem is solved. If the simulated data does not approximate the medium then another iteration is executed. To summarize the steps of the iterative Gauss-Newton method for static reconstruction are:

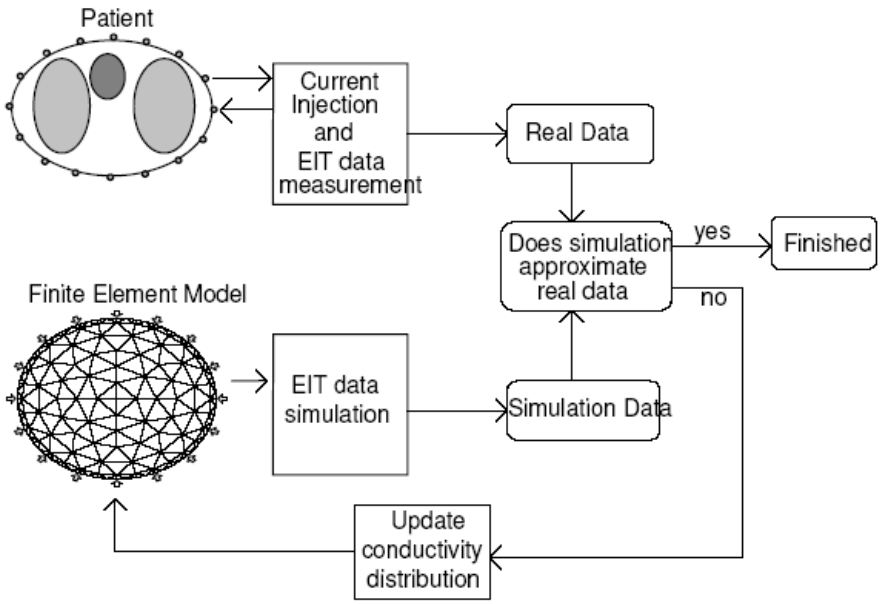

Figure 3.2: *Typical Static Imaging System (from [3]).*

1. Obtain an initial approximation for the conductivity distribution. The initial conductivity, $\boldsymbol{\sigma}_0$, distribution of the model reflects an *a priori* assumption about the conductivity distribution of the medium. However, it is often a crude estimate of the equivalent homogenous conductivity of the medium based on the data [69].

2. Solve the forward problem to determine the simulated measurements, $\mathbf{v}_{simulated}$.

3. Calculate the change in conductivity,

$$\Delta\boldsymbol{\sigma} = (\mathbf{H^T H} + \lambda^2 \mathbf{R}^T\mathbf{R})^{-1}\mathbf{H^T z} \tag{3.11}$$

   where

$$\mathbf{z} = \mathbf{v}_{measured} - \mathbf{v}_{simulated} \tag{3.12}$$

4. Update the absolute conductivity,

$$\boldsymbol{\sigma}_{k+1} = \boldsymbol{\sigma}_k + \Delta\boldsymbol{\sigma} \tag{3.13}$$

   where $\boldsymbol{\sigma}_0$ is a vector of length E and is the initial, *a priori*, conductivity.

   In terms of the Jacobian used for static imaging, each element of the Jacobian is $\mathbf{H}_{ij} = \frac{\partial z_i}{\partial x_j}\Big|_{\sigma_k}$ and relates a small change in the i^{th} error measurement, z_i where $\mathbf{z}$ is as defined in 3.12, to a small change in the conductivity of j^{th} element. $\mathbf{H}$ is a function of current injection pattern and the k^{th} conductivity estimate. Thus calculation of the Jacobian is identical for both difference and static imaging however with static imaging the signal is the error signal, 3.12, and the conductivity change is used in the iterative build up of the absolute conductivity via 3.13.

5. Update the admittance matrix with the current estimation of the conductivity. In other words form $\mathbf{Y}(\boldsymbol{\sigma}_{k+1})$.

6. Evaluate a stopping rule. For example stopping after a single iteration [35], stopping after some fixed number of iterations, or stopping after the difference between the two sets of measurements drops below some threshold [114], i.e. $\varepsilon \leq \|\mathbf{v}_{measured} - \mathbf{v}_{simulated}\|$. If the current solution satisfies the stopping rule then exit, otherwise continue to step 7.

7. Update the Jacobian based on the current estimate of the conductivity. Some researchers update the Jacobian at each iteration, others do not.

8. go to step 2. Note that $v_{simulated}$ calculated at step 2 is a function of the iteration number, k.

Equation 3.11 is similar to the difference image equation 3.7 with $\hat{\mathbf{x}} = \Delta\boldsymbol{\sigma}$ and $\mathbf{z}$ defined as the difference between the measured voltages and the set of simulated voltages, $\mathbf{z} = \mathbf{v}_{measured} - \mathbf{v}_{simulated}$. Although the interpretation of $\mathbf{x}$ and $\mathbf{z}$ are different the Jacobian is the same as those used for difference imaging. Often the regularization matrices are also the same as those used in difference imaging.

3.3.1 MAP Regularized Inverse

The most clearly formulated reconstruction model for 2D difference imaging at the start of this work was the Maximum *a Posteriori* (MAP) algorithm of Adler and Guardo [4]. The MAP approach to image reconstruction defines the solution as the most likely estimate of $\hat{\mathbf{x}}$ given the measured signal $\mathbf{z}$ and certain statistical information about the medium. This approach allows an elegant interpretation of the image reconstruction algorithm in terms of statistical properties of the experimental situation. It is explained in the following section.

In order to simplify the reconstruction algorithm the image statistical properties are modeled by a Gaussian distribution of mean x_∞ and covariance R_x

$$\begin{aligned} x_\infty &= E[x] \\ R_x &= E[x - x_\infty] = E\left[x^T x\right] - x_\infty^T x_\infty \end{aligned} \tag{3.14}$$

With these parameters the distribution function of the image, $f(x)$, is modeled as

$$f(x) = \frac{1}{(2\pi)^{N/2}\sqrt{|R_x|}} e^{-(1/2)(x-x_\infty)^T R_x^{-1}(x-x_\infty)} \tag{3.15}$$

The *a posteriori* distribution function of $\mathbf{z}$ given a conductivity distribution $\mathbf{x}$ is derived from the definition of the inverse problem, equation 3.1:

$$f(\mathbf{z}|\mathbf{x}) = \frac{1}{(2\pi)^{M/2}\sqrt{|R_n|}} e^{-(1/2)(\mathbf{z}-\mathbf{H}\mathbf{x})^T R_n^{-1}(\mathbf{z}-\mathbf{H}\mathbf{x})} \tag{3.16}$$

The difference $(\mathbf{z} - \mathbf{H}\mathbf{x})$ is due entirely to the noise n, which is assumed to be Gaussian, white, zero mean with covariance R_n. Thus

$$R_n = E\left[n^T n\right] = \begin{bmatrix} \sigma_1^2 & 0 & \cdots & 0 \\ 0 & \sigma_2^2 & & 0 \\ \vdots & & \ddots & \vdots \\ 0 & 0 & \cdots & \sigma_M^2 \end{bmatrix} \tag{3.17}$$

where σ in this and all subsequent equations in this section, represents the square root of the variance and not the conductivity.

The MAP estimate, $\hat{\mathbf{x}}$, maximizes the *a posteriori* probability distribution $f(\mathbf{x}|\mathbf{z})$. This can be understood as finding the most likely image, $\mathbf{x}$, to have produced the measured signal, $\mathbf{z}$,

$$\begin{aligned} f(\mathbf{x}|\mathbf{z}) &= \frac{f(\mathbf{z}|\mathbf{x})f(\mathbf{x})}{f(\mathbf{z})} \\ &= \frac{e^{-(1/2)\left[(\mathbf{z}-\mathbf{H}\mathbf{x})^T R_n^{-1}(\mathbf{z}-\mathbf{H}\mathbf{x})+(x-x_\infty)^T R_x^{-1}(x-x_\infty)\right]}}{(2\pi)^{(M+N)/2}\sqrt{|R_x||R_n|}f(z)} \end{aligned} \tag{3.18}$$

$f(\mathbf{x}|\mathbf{z})$ is maximized when the exponent is minimized

$$\hat{x} = \arg\min_x \left[(\mathbf{z}-\mathbf{H}\mathbf{x})^T R_n^{-1}(\mathbf{z}-\mathbf{H}\mathbf{x}) + (x-x_\infty)^T R_x^{-1}(x-x_\infty)\right] \tag{3.19}$$

yielding the estimate

$$\hat{x} = \left(\mathbf{H}^T R_n^{-1}\mathbf{H} + R_x^{-1}\right)^{-1}\left(\mathbf{H}^T R_n^{-1}\mathbf{z} + R_x^{-1}\mathbf{x}_\infty\right) \tag{3.20}$$

3.3.1.1 Parameters of the MAP estimate

The noise covariance, R_n, measures the noise power in each component of the signal. Measurement noise on each channel of the scanner can be determined from the hardware. Adler and Guardo take the case where each channel has equal noise variance σ_n. Using the definition of the signal, $\mathbf{z} = \mathbf{v_2} = \mathbf{v_1}$ (equation 3.2), R_n is calculated as $[R_n]_{ii} = \left(\sigma_n / v_i^h\right)^2$ where v_i^h are the measurements from the medium on which the noise measurements were taken. We define a matrix $\mathbf{W}$ such that $\sigma_n^2\mathbf{W} = R_n^{-1}$

The properties of the image R_x and x_∞ are less concrete than the noise properties and can only be estimated from a knowledge of the experimental configuration. The expected change in the image $E[x]$ is represented by x_∞. Conductivity changes are equally likely to be conductive or non-conductive, consequently the expected image is one of no conductivity change, and is best modelled by $x_\infty = 0$.

The covariance of the image R_x includes information on the amplitude of the image and also on the spatial frequency distribution. The diagonal elements of $[R_x]_{ii}$ represent the variance of the amplitude of each image element, whereas off diagonal elements are a function of the correlation coefficient r between a pixel in element i and a pixel in element j as follows

$$[R_x]_{ij} = r\sqrt{[R_x]_{ii}\,[R_x]_{ij}} \tag{3.21}$$

Since EIT has low spatial resolution due to the small number of measurements, it is unable to detect high spatial frequency contrasts in the image, indicating that the spatial frequency of the reconstructed distribution of conductivity change has little high frequency content. Therefore elements close to each other will have correlated reconstruction values. Adler and Guardo set diagonal elements of R_x to σ_x^2. Off diagonal elements account for the resolution of the medium: using 16 electrodes there is not enough information to see resolution on the order of 5% of the medium diameter. They assume that pixels closer than this distance are highly correlated and pixels further apart are not correlated with a gradual diminishing between the two extremes. Thus R_x is interpreted as a low pass filter. Since the formulation R_x is numerically unstable a regularization matrix, Q, was constructed directly using a high pass filter to represent R_x^{-1}. Derivation of this filter is described in section 5.2.3 with the result that $Q = \sigma_x^2 F^T F$.

Finally Adler and Guardo define the regularization hyperparameter in terms of the statistical standard deviations as $\lambda = \frac{\sigma_x^2}{\sigma_n^2}$ from which they arrive at the MAP regularized inverse

$$\hat{\mathbf{x}} = (\mathbf{H^T W H} + \lambda \mathbf{Q})^{-1} \mathbf{H^T W z} = \mathbf{B}(\lambda)\mathbf{z} \tag{3.22}$$

where $\mathbf{B}(\lambda)$ is the image reconstruction matrix first discussed in equation 2.1. Since noise is uncorrelated in the system, $\mathbf{W}$ is a diagonal matrix with $\mathbf{W}_{ii} = 1/\sigma_i^2$ where σ_i^2 is the noise variance for measurement i. $\mathbf{W}$ can also be modified to account for variable gain settings on each tomograph channel. However, for this work we assume that all measurements have equal noise variance with the result that $\mathbf{W}$ becomes a multiple of the identity matrix.

3.3.1.2 Electrode Errors

One important difficulty with experimental and clinical EIT measurements is the care required to ensure proper electrode measurements. Electrodes can become detached, the contact impedance can change because of sweat or peripheral oedema, and changes in subject posture can move electrodes and corrupt readings [89][5]. In [7], Asfaw and Adler describe a method to detect bad data caused by a single poorly attached electrode. The method appears to be useful for multiple electrode errors however the study is restricted to the former case.

In [6] Adler describes a method to explicitly account for known electrode errors in terms of the parameters of the MAP regularized inverse algorithm of 3.3.1. Electrode errors imply high noise, which is reflected in the measurement noise variance values contained in the diagonal elements of $\mathbf{R}_n$ of equation 3.20. Thus, if measurement i is subject to increased noise (by a factor σ_n^2), $\mathbf{W}_{ii}$ is reduced by the same factor. If an electrode becomes completely disconnected, or noise levels are very high, the noise variance, σ_n, can be assumed to be infinite, and the corresponding elements of $\mathbf{W}$ set to $1/\infty = 0$.

Electrode errors will reduce the number of available measurements. The adjacent pattern provides $N(N-3)$ measurements, however with a single electrode error this is reduced to $(N-4)(N-3)$ measurements. For an eight electrode system this error reduces the number of measurements by 50%, while for a 16 electrode system, the available measurements are reduced by 25%. Other stimulation patterns will have different electrode error patterns [6]. Naturally the quality of the reconstructions will be reduced by the loss of data. Details of the degradation are discussed in [6].

3.4 Variations of the Basic Model

While there are many variations to regularized solutions, the framework of the generalized Tikhonov inverse lends itself to two fundamental variations, that of the regularization matrix and that of the norm of the side constraint.

Due to its differentiability the ℓ^2 norm has been the mainstay of regularized solutions in EIT. However such quadratic optimizations are inherently smooth [69]. Recent work has investigated the use of ℓ^1 norms [25][44][79] in order to recover non-smooth conductivities. Chapter 7 discuss one such method, Total Variation, in greater detail.

With respect to the prior, in EIT, the choice of the regularization matrix $\mathbf{R}$ has traditionally been either the identity matrix [127], a diagonal matrix [35] or an approximation of differential operators [4][71][72][93].

Cheney *et al* introduced a diagonal matrix, $\mathbf{R} = diag(\mathbf{H}^T\mathbf{H})$, as the prior used in their NOSER algorithm [35]. This matrix is diagonal, and with SVD decomposition, the regularized solution can be expressed as

$$\hat{\mathbf{x}} = \sum_{i=1}^{M} f \frac{\mathbf{u}_i^T \mathbf{d}}{\sigma_i} \mathbf{v}_i$$

with

$$f = \frac{\sigma_i^2}{\sigma_i^2 + \lambda r_i^2}$$

f are the "filter factors", r_i are the diagonal elements of $\mathbf{R}$, and σ_i are the singular values of $\mathbf{R}$. For small singular values $f \to 1$ and for large singular values $f \to 0$.

3.4.1 Thoughts on Regularization

The use of Tikhonov style regularization techniques is equivalent to introducing *a priori* information to the reconstruction process. The fundamental prior information of the conductivity solution is that it is a positive function, Such methods provide stability but force solutions to be smooth in some sense thus eliminating the possibility of non-smooth solutions. This is reasonable given that the undesired, noise dominated, solutions contain components with high spatial frequencies.

One way in which the generalized Tikhonov regularization method can be understood to work, is that it draws the solution towards the null space $N(\mathbf{R})$ of the regularization matrix $\mathbf{R}$ [114]. If we use, for example, the first difference matrix, the solution is drawn toward a constant distribution because a constant solution forms the basis for the null space of the first difference matrix. Moreover if we have some information on the true resistivity distribution, the regularization matrix can be constructed in such a way that the solution is drawn towards the known distribution by the regularization. This can be implemented by penalizing the difference between the reconstructed conductivity, $\boldsymbol{\sigma}$, and the *a priori* assumption about the conductivity instead of the just penalizing the solution. Symbolically, rather than minimize equation 3.7 we minimize

$$\hat{\mathbf{x}} = \arg\min_{\mathbf{x}} \left\{ \|\mathbf{Hx} - \mathbf{z}\|^2 + \lambda^2 \|\mathbf{R}(\mathbf{x} - \mathbf{x}^*)\|^2 \right\} \tag{3.23}$$

where $\mathbf{x}^*$ is the *a priori* assumed distribution. This idea was evaluated by Vauhkonen *et al* in [113] and [114]. In [113] the conductivity distribution was approximated as a linear combination of some pre-selected basis functions that were constructed from prior information on the structures and conductivities. The method, called the Basis Constraint Method (BCM), produced good results when the priors were correct but provided misleading results when the prior was incorrect. Here misleading means that the solutions contained structural artefacts due to the prior that were not part of the true conductivity. In [114] Vauhkonen *et al* used the same kind of idea but rather than forcing the solution to be in the subspace spanned by pre-selected basis functions they only "draw" the solution towards the subspace. This method, called the Subspace Regularization Method, provided an improvement over the BCM in that they could partially avoid misleading results even if the prior information was not correct.

3.5 3D Considerations

In EIT it is often assumed that the injected currents stay in the two-dimensional electrode plane [115]. This assumption has been used since the early days of EIT, however, it is obviously incorrect since electric currents will spread out in three dimensions.

Reports of EIT in the clinical literature rarely use 3D EIT possibly due to the difficulty of applying large numbers of electrodes and the high data collection rate needed for monitoring physiological function. 3D reconstruction algorithms concerning medical applications can be found in Gobel *et al* [59], Metherall *et al* [90], Polydorides [98], Polydorides and McCann [99], Blue *et al* [22] and Molinari *et al* [91]. In three dimensions the possibilities for electrode configurations and injection and measurement protocols are much larger than in 2D. With cylindrical tanks a typical configuration is to use equally spaced electrodes arranged on several parallel planes.

The main problem with 3D is computational: with three dimensional EIT the complexity of body shapes and components requires a finite element model with a large number of elements. Since the storage and computing time increase as a function of the number of elements either the mesh discretization must be left too coarse to obtain images unaffected by the element size or the mesh will so large that it causes the computer to run out of memory during solution [91]. One either has to parallelize the problem onto several processors [21], or investigate more efficient algorithms such as dual meshing [95]. The iterative Newton-Raphson method is suitable for small-scale EIT problems. However it can be unsuitable for large 3D problems where the number of elements can easily exceed 5000. This corresponds to a matrix size of 25×10^6 or a memory requirement of 200 MB to store the matrix alone.

3.6 GOE MF Type II System

A detailed analysis on EIT hardware design and analysis can be found in [58][40][129]. The first successful tomographic style impedance imaging was performed by Barber and Brown in the early 80's [15] using the Sheffield Mark 1 system [27] with the filtered backprojection reconstruction algorithm. This is a 16 electrode adjacent drive system that measures 12.5 frames per second. The architecture of medical scanning equipment has not changed much. For example Viasys Healthcare, Höchberg, Germany manufactures the Goe-MF II type tomography system, which like the Sheffield Mk 1 has a single amplification unit and a single detection unit that are multiplexed to 16 electrodes. Both are intended for use with the adjacent constant current drive. The EIT group at Goettingen has improved the basic system by optimizing some analog components and digitizing the signal at an earlier stage of the processing. This has provided a large improvement in signal to noise ratio of the EIT signal. In [62] they reported that the Goe-MF type II provides an order of magnitude improvement in SNR over the Sheffield Mk 1. Like the Sheffield Mk 1 this machine is intended to be used to collect 2D data from a planar set of 16 electrodes equispaced around the thorax. The default reconstruction algorithm is a functional image based on individual frames reconstructed using filtered backprojection [62]. However the raw measurement data can be exported for use with algorithms not included with the Goe-MF II. This machine was used to obtain empirical data used to verify some of the work in this thesis.

3.7 Summary

3.7.1 Reconstruction Summary

Here we summarize the state of the art in EIT difference imaging for clinical applications such as pulmonary imaging. The framework is the non-linear optimization problem, equation 3.7, which is reproduced below:

$$\hat{\mathbf{x}} = \arg\min_{\mathbf{x}} \left\{ \|\mathbf{Hx} - \mathbf{z}\|^2 + \lambda^2 \|\mathbf{Rx}\|^2 \right\} \tag{3.24}$$

This is solved using the MAP regularized framework of equation 3.22 again repeated below:

$$\hat{\mathbf{x}} = (\mathbf{H^T W H} + \lambda^2 \mathbf{R}^T \mathbf{R})^{-1} \mathbf{H^T W z} = \mathbf{B}(\lambda)\mathbf{z} \tag{3.25}$$

where $\mathbf{z} = \mathbf{v}_2 - \mathbf{v}_1$. The framework has several explicit parameters that must be selected by the user:

1. The regularization hyperparameter, λ, is the subject of chapter 4.
2. The norm of the prior, $\|\mathbf{Rx}\|^2$, has historically been the ℓ^2 norm. The ℓ^1 norm has been used for "blocky" reconstructions. An algorithm for solving the ℓ^1 norm is evaluated in chapter 7.
3. The prior matrix, $\mathbf{R}$, has many possibilities as discussed in this chapter.
4. The data weighting matrix $\mathbf{W}$ has the ability to consider noise and erroneous electrode data. However with equal noise variance on each measurement channel and with good electrodes (no accounting for erroneous electrodes), $\mathbf{W}$ becomes a scaled version of the identity matrix.

In addition to these explicit parameters there are several implied parameters that conform to some assumptions:

1. The initial conductivity, σ_0, is typically assumed to be homogenous.
2. The conductivity used to calculate the Jacobian, σ^*, is typically assumed to be homogenous.
3. FEM modeling issues including degree of the shape functions (linear, quadratic), isotropy of element conductivity, and mesh parameters such as number and degree (triangle, quadrilateral) of elements, geometry, shape of the reconstructed mesh dimension (2 or 3).
4. Electrode types, locations and size.
5. Current injection and measurement patterns.

None of these parameters appear explicitly in equations 3.24 or 3.25 but are important parts of the problem. There is much work describing variations of the framework in terms of explicit and implied parameters, however, there is little quantitative information on how they compare and how important any one of them is.

Chapter 4

Objective Selection of Hyperparameter

This chapter is the text, with minor revisions, of a paper titled "Objective Selection of Hyperparameter" by Bradley GRAHAM and Andy ADLER published in Physiological Measurement 27 (2006) S65-79.

This paper addresses the issue of hyperparameter selection in EIT (section 1.3 objective O1 and section 1.4.1 Contributions by Objective O1): improve the method of hyperparameter selection in order to eliminate case by case tweaking of parameters, provide repeatability of experiments, and reduce number of reconstructions needed to find the best reconstruction for a given data set. The main contribution of this paper is the development of the *BestRes* hyperparameter selection method which is demonstrated to be as good or better than existing methods while being stable and repeatable.

Abstract

An algorithm for objectively calculating the hyperparameter for linearized one-step electrical impedance tomography (EIT) image reconstruction algorithms is proposed and compared to existing strategies. EIT is an ill-conditioned problem in which regularization is used to calculate a stable and accurate solution by incorporating some form of prior knowledge into the solution. A hyperparameter is used to control the trade-off between conformance to data and conformance to the prior. A remaining challenge is to develop and validate methods of objectively selecting the hyperparameter. In this paper, we evaluate and compare five different strategies for hyperparameter selection. We propose a calibration-based method of objective hyperparameter selection, called *BestRes*, that leads to repeatable and stable image reconstructions that are indistinguishable from heuristic selections. Results indicate: (1) heuristic selections of hyperparameter are inconsistent among experts, (2) generalized cross-validation approaches produce under-regularized solutions, (3) L-curve approaches are unreliable for EIT and (4) *BestRes* produces good solutions comparable to expert selections. Additionally, we show that it is possible to reliably detect an *inverse crime* based on analysis of these parameters.

Keywords: regularization, EIT, hyperparameter, L-Curve, GCV

4.1 Introduction

Electrical impedance tomography (EIT) attempts to calculate a stable and accurate image of the conductivity or conductivity change within a medium from electrical measurements made on the medium boundary. The image reconstruction problem is essentially underdetermined and characterized by a system matrix with large condition number. Image reconstructions obtained through naïve methods such as least squares are unstable and dominated by noise. The problem has been overcome through the use of various regularization methods which produce useful solutions by imposing additional conditions (priors), such as image smoothness, on the problem [113]. The trade-off between solution conformance to the measured data and conformance to the prior is controlled by a scalar hyperparameter, often labelled λ.

A difficulty with experimental and clinical EIT reconstruction algorithms is the tendency of algorithms to rely on subjective methods to select a hyperparameter. The absence of objective hyperparameter selection methods results in several issues which hinder experimental and clinical use of the technique: (1) users of EIT for clinical applications are uncomfortable using 'fiddle' adjustments to modify images, (2) comparisons of EIT reconstruction algorithms can be subjective due to the necessity of manual tuning of hyperparameter values, (3) experimental work is not repeatable if disparate researchers cannot objectively recreate the hyperparameter values used in the work of others and (4) meta-algorithms, such as detection of electrode errors [7], require a method to fix these values.

In order to address this issue, we investigate some existing hyperparameter selection methods and propose a new calibration based method called *BestRes* (Best Resolution). By 'calibration' we mean that a procedure is defined to select a value for a given EIT system and measurement configuration rather than for each image or data set. We define a configuration as the combination of current injection pattern, finite element mesh (FEM), assumed prior conductivity (σ_0) and regularization prior. Consequently, the objective hyperparameter methods discussed in this paper are functions of this configuration. Hyperparameter selection methods are then compared for several one-step linearized EIT reconstruction algorithms.

4.2 Methods

This paper addresses the problem of objective hyperparameter as follows: in the methods section we describe the family of EIT reconstruction algorithms used throughout this paper. In hyperparameter selection methods we describe five hyperparameter selection strategies, including a new calibration-based method called *BestRes*. In the results, we describe the effectiveness of each strategy and compare the performance of the objective methods with heuristic selection. In the discussion we consider some additional observations of this work. We conclude with a recommendation of the *BestRes* hyperparameter selection method.

We consider EIT difference imaging, which is widely understood to improve reconstructed image stability in the presence of problems such as unknown contact impedance, inaccurate electrode positions, nonlinearity, and the use of 2D approximations for 3D electrical fields [18] [87]. Initially, we address the class of normalized one-step linearized reconstruction algorithms that calculate the proportional change in a finite element conductivity distribution, $\mathbf{x} = (\boldsymbol{\sigma_2} - \boldsymbol{\sigma_1})/\boldsymbol{\sigma_1}$, due to a proportional change in difference signal, $\mathbf{z} = (\mathbf{v_2} - \mathbf{v_1})/\mathbf{v_1}$, over a time interval (t_1, t_2). By convention we consider the signal at t_1 to be the *reference* frame and the signal at t_2 to be the *data* frame. Since we do not know $\boldsymbol{\sigma}_1$, $\mathbf{x}$ is interpreted as the proportional change in conductivity with respect to the unknown

initial conductivity $\mathbf{x} = \boldsymbol{\Delta\sigma}/\boldsymbol{\sigma_0}$. For small changes around a background conductivity the relationship between $\mathbf{x}$ and $\mathbf{z}$ may be linearized as

$$\mathbf{z} = \mathbf{H}\mathbf{x} + \mathbf{n} \tag{4.1}$$

where $\mathbf{H}$ is the Jacobian or sensitivity matrix and $\mathbf{n}$ is the measurement system noise, assumed to be uncorrelated additive white Gaussian (AWGN). Each element i, j, of $\mathbf{H}$ is calculated as $H_{ij} = \frac{\partial z_i}{\partial x_j}\Big|_{\sigma_0}$ and relates a small change in the i^{th} proportional difference measurement to a small change in the proportional conductivity of j^{th} element. $\mathbf{H}$ is a function of the finite element mesh (FEM), the current injection pattern, and the background conductivity, $\boldsymbol{\sigma}_0$. We use the adjacent current injection pattern and a homogeneous background conductivity with $\boldsymbol{\sigma}_0 = 1$ for each of the elements. Normalizing the signal requires that we also normalize the sensitivity matrix by dividing its columns by $\mathbf{v_{ref}}$ which is a vector of reference voltages obtained by solving the forward problem [4] over a homogeneous domain.

4.2.1 Regularization

In order to overcome the ill conditioning of $\mathbf{H}$ we solve 4.1 using the following regularized inverse

$$\hat{\mathbf{x}} = (\mathbf{H^T}\mathrm{W}\mathbf{H} + \lambda\mathbf{R})^{-1}\mathbf{H^T}\mathrm{W}\mathbf{z} = \mathbf{B}\mathbf{z} \tag{4.2}$$

where $\hat{\mathbf{x}}$ is an estimate of the true proportional change in conductivity distribution, $\mathbf{R}$ is a regularization matrix, λ is a scalar hyperparameter that controls the amount of regularization, and $\mathbf{W}$ models the system noise. Since noise is uncorrelated in the system $\mathbf{W}$ is a diagonal matrix, $\mathbf{W_{i,i}} = \mathbf{1}/\sigma_\mathbf{i}^\mathbf{2}$ where σ_i^2 is the noise variance for measurement i. $\mathbf{W}$ can also be modified to account for variable gain settings on each tomograph channel. However, for this work we assume that all measurements have equal noise variance, thus $\mathbf{W}$ becomes a multiple of the identity matrix. With $\mathbf{R} = \mathbf{I}$ (labelled $\mathbf{R}_{Tik}$) equation 4.2 is the 0^{th} order Tikhonov algorithm. With $\mathbf{R} = diag(\mathbf{H})$ (labelled $\mathbf{R}_{diag(\mathbf{H})}$) equation 4.2 is the regularization matrix used in the NOSER algorithm of [35]. [4] modelled $\mathbf{R}$ as a spatially invariant Gaussian high pass filter (labelled $\mathbf{R}_{HPF}$) with a cut-off frequency selected so the spatial period is a given fraction of the medium diameter. $\mathbf{R}_{HPF}$ reconstructions appear reasonable for cut-off frequencies corresponding to 5%, 10% and 20% diameter. A 16 electrode EIT system, using adjacent measurements not at current injection sites, yields 208 measurements of which 104 are independent. 104 measurements justifies the recovery of 104 conductivity parameters which permits, for example, the reconstruction of a 10×10 grid corresponding to a resolution of roughly 10%. Thus we consider λ_{HPF} for 10% because it appears better justified in terms of available independent measurements. All three of these priors are smoothing filters, however the Gaussian HPF has the advantage of being mesh size independent in that it is a function of the mesh inter-element correlations. Both Tikhonov and NOSER are ad hoc priors that do not consider correlations between solution mesh elements.

While several other one-step regularized inverse algorithms exist for EIT [18][86][36], in this paper we consider equation 4.2 with the Tikhonov, NOSER and Gaussian HPF regularization matrices as a representative sample with which to compare hyperparameter selection strategies. The hyperparameter selection functions discussed in this paper were developed primarily with EIDORS [8] and will be contributed to that EIT framework. In this paper, we do not address issues of execution speed or algorithm efficiency as we are primarily interested in effectiveness of hyperparameter selection.

4.2.2 Figure of merit

A quantitative figure of merit is required in order to compare the quality of the reconstructed images. In [120] Wheeler *et al* reviewed several figures of merit for EIT that have been proposed in the literature. The primary figure of merit used in this work is *resolution* which we calculate in terms of blur radius (BR). We define BR as $BR = r_z/r_0 = \sqrt{A_z/A_0}$ where r_0 and A_0 are the radius and area respectively of the entire 2D medium and r_z and A_z are the radius and area of the reconstructed contrast containing half the magnitude of the reconstructed image [4]. BR calculates the area fraction of the elements that contain the largest amplitude contributions to 50% of the total image amplitude. It is a measure of the concentration of image amplitude. We call the set of elements that contribute to the blur radius the half amplitude (HA) set. Figure 4.1(a) shows the evolution of the HA set in response to increasing λ for an impulse contrast. Figure 4.1(b) shows the corresponding impedance change images, here represented with 3D visualization. With insufficient λ the image is dominated by noise and the HA set is composed of spatially disjoint elements. As λ is increased, noise is filtered through the smoothing action of the prior, image energy starts to concentrate and the HA set starts to cluster. The point at which the HA set is comprised of adjacent elements is termed the 'onset of stability' (OS). Excessive regularization blurs the image and expands the now contiguous HA set. A resolution curve (plot of blur radius versus λ) such as figure 4.5(b) shows a rapid improvement in resolution (indicated by decreasing blur radius) reaching a maximum resolution indicated by the minimum blur radius value. This is followed by a slow degradation in resolution (indicated by an increasing blur radius) as filtering starts to blur the image. For an impulse contrast the minimum point of the resolution curve indicates the best resolution. This value can be considered optimal with respect to both resolution and stability (slope of curve is low indicating small change in signal for a small change in λ) for the given data set.

Blur Radius as the Point Spread Function The point spread function (PSF)[1] describes the response of an imaging system to a point source or point object. A point source has negligible extent, distinguishing it from other source geometries. When a signal is generated by an impulse or pseudo-impulse (i.e. from a phantom consisting of a single element of the generating mesh), the HA set of the resulting image is the EIT analog of the point spread function of the system.

4.3 Hyperparameter Selection Methods

The goal of hyperparameter selection is to produce a "good" reconstruction. Intuitively hyperparameter selection should produce solutions that preserve as much of the measured data as possible by applying the least amount of *a priori* information required to obtain a useful reconstruction.

4.3.1 Heuristic Selection

The most common method of hyperparameter selection is Heuristic Selection in which researchers examine sets of reconstructions generated over a range of hyperparameter values and select the image they like best. This method is highly subjective and not repeatable. To our knowledge no research has specifically evaluated the performance of objective hyperparameter selection for one step solutions.

[1] Another commonly used term for the PSF is a system's impulse response.

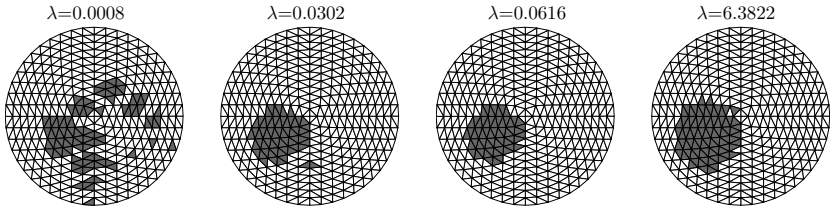

(a) *2D images of the evolution of half amplitude set (dark triangles) with increasing* λ

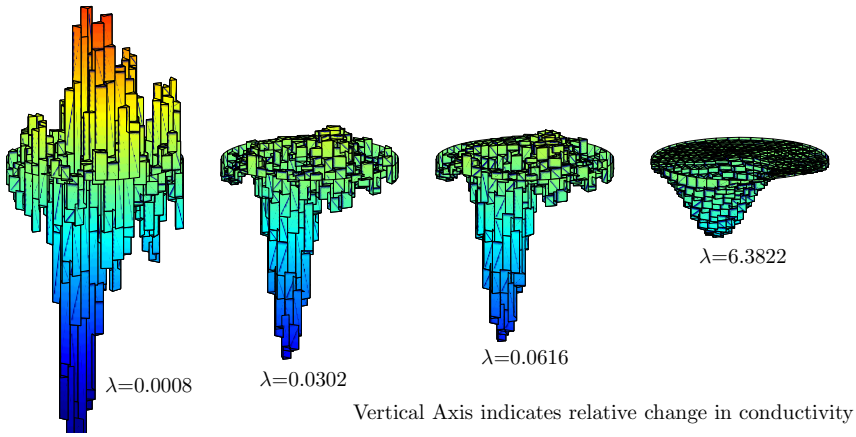

(b) *3D images of the evolution of proportional conductivity change image with increasing* λ.

Figure 4.1: *Images reconstructed on a 576 element mesh using tank data of an impulse phantom and the* R_{HPF} *prior. The third image with* $\lambda = 0.0616$ *represents the best image in terms of resolution.*

In this work, heuristic selection was performed by five graduate students[2] who were asked to participate in an experiment evaluating human performance in choosing regularization parameters. A web site was set up in which five independent data sets were used to generate sequences of reconstructions. Each sequence showed reconstructions as a function of 77 different values of the hyperparameter. Each web page, such as the example of figure 4.2(a), showed the same conductivity change solution using eight visual styles (sub-images). Each pair of images is shown as a 2D false colour representation of the conductivity change image and an associated 3D version where the z dimension represents conductivity change. The left half of the page shows the reconstruction as a decrease in conductivity while the right side shows the inverse of the image (we reverse the reference and data frames) so that the reconstruction appears to be a conductivity increase. The top row uses relative colour and z-axis scaling, thus each subimage in the 77 page sequence uses the full range of colours. For the 3D representation the conductivity is scaled to fill the entire z-axis. The bottom row uses an absolute colour and z-axis scaling thus each subimage of the 77 page sequence uses the same colour and vertical axis extent. Consequently highly smoothed images (large hyperparameter values), such as figure 4.2(b) have little color variation and reduced vertical extent compared to images reconstructed with lower hyperparameter values such as figure 4.2(a). Students were instructed to choose the best image based on the following definition: the image which shows the best resolution for the contrasting region(s) without excessive

[2]We use the term expert to denote a person who has been instructed to select an image based on some criteria.

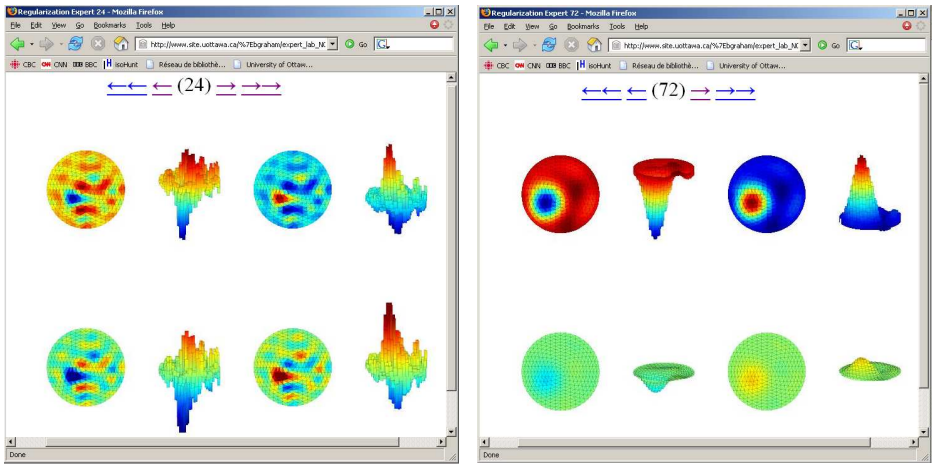

(a) $\lambda = 0.00071036, NF = 8.3048$ (b) $\lambda = 3.736, NF = 0.3026$

Figure 4.2: *Two web pages from the heuristic selection experiment. Images generated from tank data using $\boldsymbol{R}_{HPF}$ prior with different hyperparameter values.*

contamination by noise.

The same set of students was asked to repeat the experiment four months later. Students were instructed not to look at their earlier results as the aim of the second experiment was to evaluate repeatability.

4.3.2 L-Curve

Perhaps the most well known method of hyperparameter selection after heuristic selection is the L-Curve method [64]. This method plots the semi-norm of the regularized solution, $\log_{10}|\mathbf{R}\hat{\mathbf{x}}|$, versus the norm of the corresponding residual vector, $\log_{10}|\mathbf{H}\hat{\mathbf{x}} - \mathbf{z}|$, parametrically over λ. The resulting plot, such as figure 4.3(a), will often have an "L" shape where the optimal value for λ is located at the point of maximum curvature. Hansen describes a method for calculating this "corner" of the L-curve in [63]. We call this value λ_{LC}. There are cases where the L-Curve may fail, for example figure 4.3(b) is an L-Curve that does not have a "corner".

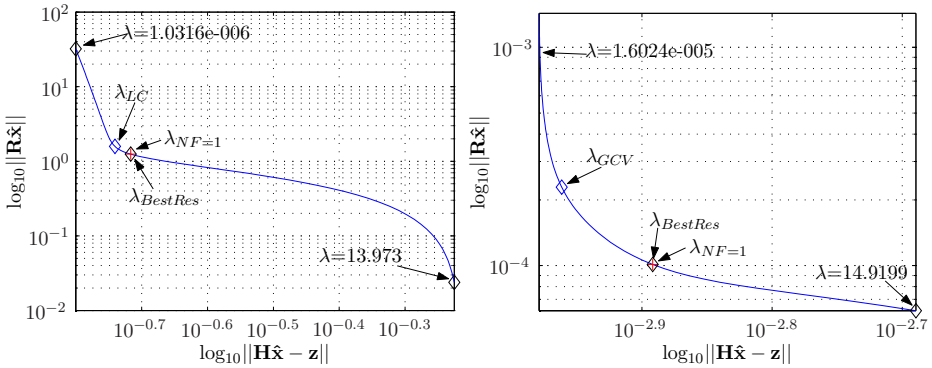

(a) *Tank data reconstructed using the $\boldsymbol{R}_{Tik}$ prior*

(b) *Simulated data reconstructed using the $\boldsymbol{R}_{diag}$ prior. The L-curve fails to indicate a corner value for (b).*

Figure 4.3: *Example L-curves reconstructed from tank phantom data using a 2D 576 element mesh.*

4.3.3 Generalized Cross-Validation

Generalized cross-validation (GCV) is based on the principle that if any arbitrary element of the data (right hand-side, $\mathbf{z}$, is left out, then the corresponding regularized solution should predict the missing element [63]. Its advantage is that no prior knowledge about the error norm is required. This leads to choosing a regularization parameter which minimizes the GCV function

$$GCV\,(\lambda) = \frac{\|\mathbf{H}\hat{\mathbf{x}} - \mathbf{z}\|^2}{trace\,(\mathbf{I} - \mathbf{HB})^2} \tag{4.3}$$

where $\mathbf{B}$, $\mathbf{z}$ and $\hat{\mathbf{x}}$ are as in equations 4.1 and 4.2. Hansen [63] discusses the use of GCV with the Tikhonov prior; however, in this work we evaluate the GCV method with all three priors.

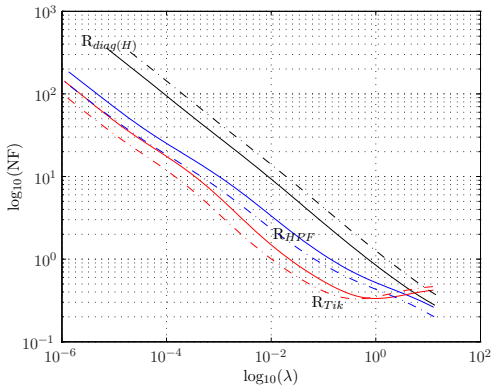

Figure 4.4: *NF versus λ (logarithmic axes) for algorithms $\boldsymbol{R}_{diag(\boldsymbol{H})}$ (black), $\boldsymbol{R}_{HPF}$ (blue), $\boldsymbol{R}_{Tik}$ (red). Solid lines: simulated data reconstructed on 256 element 2D mesh. Dashed lines: tank data reconstructed on 576 element 2D mesh. Throughout the range of useful solutions, NF and λ are linearly related.*

4.3.4 Fixed Noise Figure (NF)

The Fixed NF Method is based on a Noise Figure calculation introduced by Adler and Guardo in [4] where NF is defined as the ratio of signal-to-noise-ratio in the measurements to signal-to-noise-ratio in the image:

$$NF = \frac{SNR_{in}}{SNR_{out}} = \left(\frac{mean[\mathbf{z_c}]}{\sqrt{\text{var}[\mathbf{n}]}}\right) \Bigg/ \left(\frac{mean[\mathbf{Bz}_c]}{\sqrt{\text{var}[\mathbf{Bn}]}}\right) \tag{4.4}$$

The signal used in this definition is $\mathbf{z_c} = \mathbf{Hx_c}$, where $\mathbf{x_c}$ is a small contrast in the centre of the medium. The user selects a NF value and the corresponding λ is found using a bisection search technique. The Fixed NF Method substitutes the manual selection of λ with the manual selection of a NF, which the algorithm then maps to a hyperparameter value; the value for $NF = 1$ is labelled $\lambda_{NF=1}$. As shown in figure 4.4, for a given configuration $\log(NF)$ is nearly linearly inversely proportionally to $\log(\lambda)$ throughout the extent where λ yields good solutions.

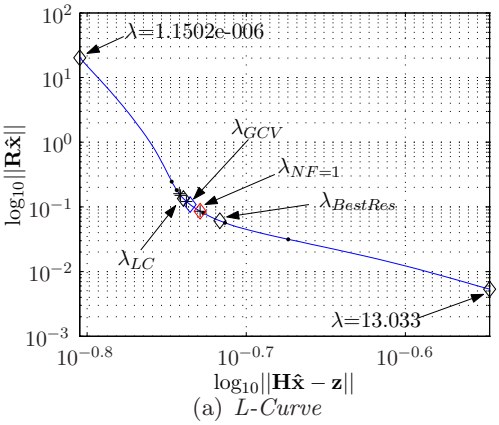

(a) *L-Curve*

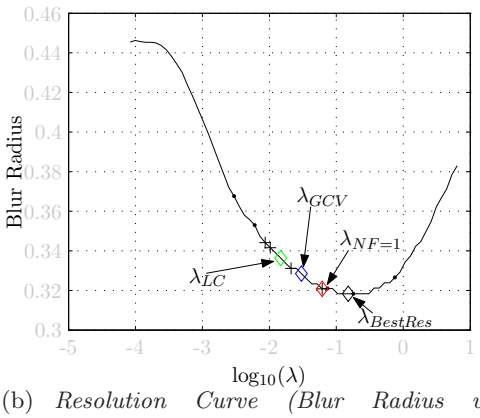

(b) *Resolution Curve (Blur Radius vs log10(λ))*

Figure 4.5: *Comparison of hyperparameter values selected from the various methods mapped to L-curve and resolution curve. Un-annotated points on the curves indicate the first set of heuristic selections. Un-annotated crosses indicate the second set of heuristic selections.*

4.3.5 BestRes Method

The resolution curve, of which figure 4.5(b) is an example, was introduced in section 4.2.2. This curve suggests the following hyperparameter selection strategy, which we refer to as the *"BestRes"* method, as follows:

1. Image an impulse contrast
   (a) The preferred method is to use imaging equipment to collect a frame of reference data from a homogenous medium. Then collect a data frame by imaging an impulse contrast using a physical phantom located halfway between the centre and boundary of medium ($r/2$).
   (b) If equipment is not available the method can use simulated data. Again simulate a reference frame using a homogenous medium. Simulate a data frame by changing the conductivity of a single mesh element located at $r/2$
2. Reconstruct a series of images as a function of the hyperparameter and plot the associated Resolution curve as in figure 4.5(b).
3. Determine $\lambda_{BestRes}$ as the point for maximum resolution - minimum BR. This value of λ is then used for all subsequent reconstructions using simulated or real data.

If using simulated data then representative noise should be included. We suggest producing several resolution curves (we used 50) each with a different instance of the representative noise level. Each curve will produce a value of $\lambda_{BestRes}$. The mean of this set of $\lambda_{BestRes}$ is the output of the *BestRes* method.

4.4 Results

4.4.1 Data Sources

Three sources of test data were used to compare the hyperparameter selection methods:

1. simulated data, generated using a 2D finite element mesh with 1968 elements using the point electrode model. Data for the reference frame was generated using a homogenous background conductivity with $\boldsymbol{\sigma}_0 = 1$. The data frame was generated by reducing the conductivity of a single FEM element (0.05% of medium area) located halfway along the radius of the tank ($r/2$) by 15%.

2. simulated data obtained by adding Gaussian noise to set #1. Noise variance was 0.05% of maximum signal value, and

3. tank data using a Goe-MF II type tomography system (Viasys Healthcare, Höchberg, FRG). The reference frame of the tank data was generated using a homogenous saline solution in a 30cm diameter tank. The data frame was generated using a 2cm diameter non-conductive impulse phantom located at $r/2$ in the plane of the electrodes.

Both simulated and tank data used 16 electrodes equispaced in a plane driven with the adjacent current drive protocol, excluding data on driven electrodes.

The three data sets were used to reconstruct images using 18 configurations (6 meshes, 3 regularization matrices). The 6 meshes have 64, 256, 492, 576, 1024, and 1968 elements. Reconstructions of simulated data using the 1968 element mesh constituted an inverse crime [122], which we discuss later. The hyperparameter selection methods are compared using the L-Curve and Resolution Curves of figures 4.5. Hyperparamater values selected from each of the methods are shown on both curves. Associated reconstructions are shown in figure 4.6.

4.4.2 Heuristic Results

The points on figures 4.5 indicate the first set of hyperparameters selected (indirectly) by heuristic selection. The associated reconstructions are found in figure 4.6. Heuristic selections varied and were not confined to the minimum region of the Resolution Curve or knee of the L-Curve: no clear preference was shown among images reconstructed using λ from the minimum region of the Resolution Curve. The crosses on figures 4.5 indicate the hyperparameter values selected by the same experts when the experiment was repeated 4 months later. Results indicate that Heuristic selections of hyperparameter are inconsistent among experts and unrepeatable. Heuristic selections are subject to many biases including the colour scheme used in images, whether impedance changes are shown from a 2D or 3D perspective, the *a priori* expectation of the expert concerning noise levels, desired image properties, and other unknown individual idiosyncrasies. The heuristic results suggests that there is no single preferred value of λ, rather there is a preferred region of λ over which reconstructions are not subjectively distinguishable.

4.4.3 L-Curve Results

Although most L-Curves from this data were able to indicate an optimal trade-off region, not all curves had a pronounced enough corner to allow unambiguous selection of λ. In the six Tikhonov configurations the L-Curve always indicated a clear point of maximum curvature. However there were some configurations, such as figure 4.3(b), where the L-Curve did not exhibit a corner from which a hyperparameter could be calculated. In general the L-Curve indicated a lower value for λ than the Fixed NF and *BestRes* methods. As a result L-Curve derived images were comparatively noisier. In several instances λ_{LC} occurred much earlier than the onset of stability. We make the observation that L-Curves for the NOSER and Gaussian HPF priors are shallower than classic L-Curves discussed in the inverse problems

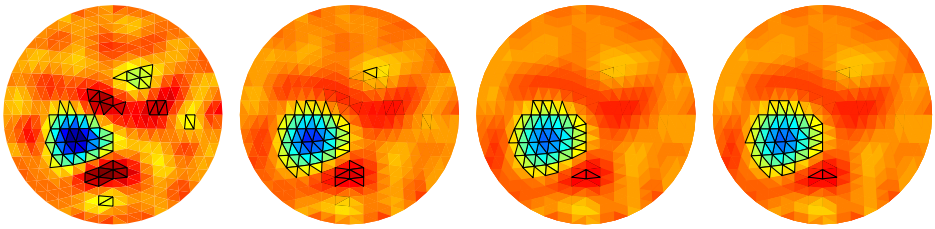

(a) *Lowest Heuristic Selection* (b) λ_{LC} (c) λ_{GCV} (d) $\lambda_{BestRes}$ *which was coincidentally the highest heuristic selection.*

Figure 4.6: *Reconstruction of phantom data on 576 element 2Dmesh, using different hyperparameter selection strategies. Black bordered triangles are elements of the half amplitude set.*

field such as [64]. This is illustrated in figure 4.7 which compares the relatively sharp corner of the Tikhonov L-Curve to the shallower curves for the Gaussian HPF and NOSER priors.

The L-Curve method also requires the generation of an L-curve for each set of data. It is preferable to be able to calculate a single hyperparameter value suitable for continuous use with a specific configuration which can be done with the *BestRes* and fixed NF methods.

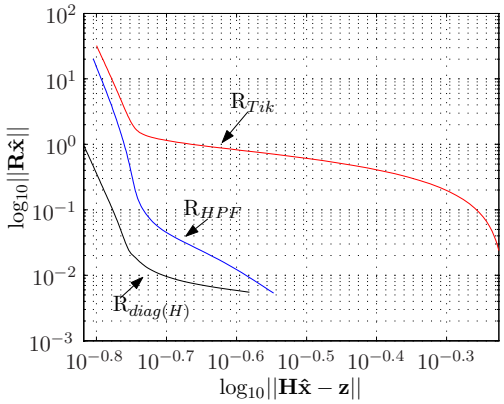

Figure 4.7: *L-curves reconstructed on 576 element 2D FEM using data from saline phantom for priors $\boldsymbol{R}_{Tik}$, $\boldsymbol{R}_{HPF}$, and $\boldsymbol{R}_{diag}$. The L-curve shapes vary significantly; only $\boldsymbol{R}_{Tik}$ shows a well-defined knee, while the others are much shallower.*

4.4.4 GCV

It has been noted [111] that that the GCV method can lead to very small values of λ leading to solutions that are severely under-regularized. As illustrated in figure 4.8 the GCV function can also be very shallow making it difficult to isolate a clear minimum. In some cases the GCV curve was monotonically increasing thus did not have a minimum. For example the GCV curve for a reconstruction using tank data on the 576 element mesh with the Tikhonov prior failed to exhibit a minimum. Overall the GCV criterion was unreliable in calculating hyperparameters for linearized one-step EIT reconstructions.

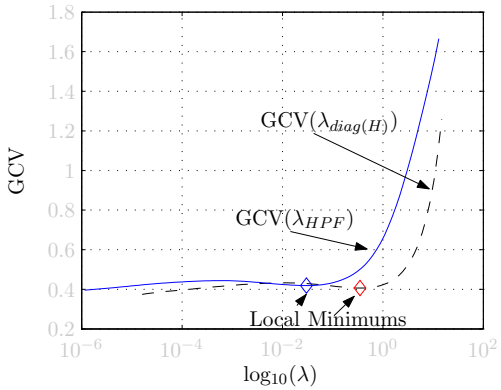

Figure 4.8: *GCV curves for different priors reconstructed on the same 576 element mesh using the same tank data. Plot indicates shallowness of some GCV curves and consequent potential difficulty of finding a clear minimum.*

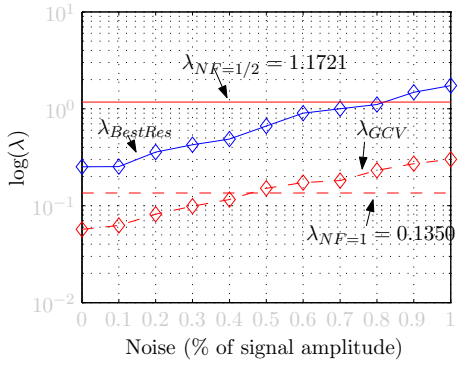

Figure 4.9: λ *versus noise for simulated data reconstructed on the 256 element mesh with the Gaussian HPF prior. Simulated AWGN was added to the signal.*

4.4.5 BestRes Results

As described in section 4.3.5, the *BestRes* method can use real or simulated data to calculate the hyperparameter with similar results. Using real data has the potential to produce a hyperparameter for the given configuration that is tailored to the equipment. In practice the reconstructions obtained using this seemingly more accurate method are not qualitatively improved over those that are generated using simulated data. For both tank and simulated data using all 18 configurations the resolution curve exhibited a distinct minimum point at which $\lambda_{BestRes}$ could be calculated and subsequently used to obtain a "good" reconstruction. It appears that resolution is a useful figure of merit for EIT reconstructions.

4.4.6 Fixed NF Results

With both the tank and simulated data $\lambda_{NF=1}$ was consistently located in the minimal region of the resolution curve. Moreover $\lambda_{NF=1}$ always fell within the boundaries of the hyperparameters selected by the experts (i.e. it was as consistent as the experts). Fixed NF with $NF = 1$ always calculated a hyperparameter that resulted in a good reconstruction. Our earlier experience using simulated, tank and clinical data has shown that noise figures in the range $0.5 - 2$ consistently lead to good reconstructions regardless of configuration while the associated λ value can range over several orders of magnitude dependent on con-

figuration. For the 18 configurations used in this work, λ ranged over 3 orders of magnitude for $NF = 1$. The advantage of the fixed NF method is that the suitable NF range is not configuration dependent while λ is.

4.5 Discussion

This paper has investigated the performance of various hyperparameter selection methods including the *BestRes* method herein introduced. In the course of these studies it became clear that several other aspects of EIT image reconstruction are related to hyperparameter selection. In this section we discuss the effects of noise level, radial position of contrasts and normalization on hyperparameter selection. We also touch on applicability to nonlinear reconstructions and inverse crimes.

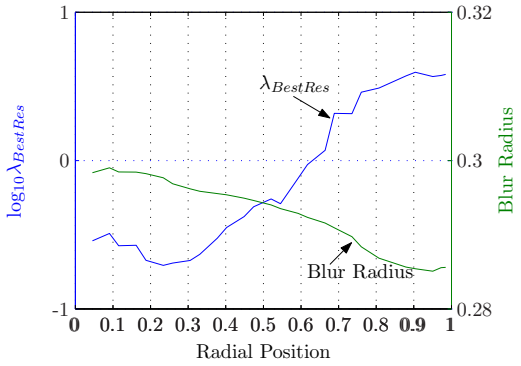

Figure 4.10: *λ and resolution versus radial position, simulated data reconstructed on the 256 element mesh using the Gaussian HPF prior. Left axis is* $\log_{10}\lambda_{\text{BestRes}}$*, right axis is resolution measured in terms of blur radius. Radial position of 0 is centre of the tank, radial position of 1 is edge of the tank. The simulated data included AWGN with noise = 0.50% of the signal amplitude.*

4.5.1 Effect of noise on λ

We performed additional experiments in order to explore further the behaviour of the fixed NF and *BestRes* methods. Simulated data from an impulse contrast were generated with increasing amounts of additive white Gaussian noise (AWGN). Figure 4.9 shows $\lambda_{BestRes}$ as a function of increasing noise. Hyperparameter values calculated by all methods except fixed NF increased as noise level increased resulting in greater noise suppression through increased smoothing. The maximum noise levels used in this work are much larger than found in practice but were used to understand trends.

Since fixed NF is not a function of the data, hyperparameters selected with fixed NF do not change with noise. Consideration of data noise will in general require more smoothing (therefore larger λ values). However at realistic noise levels $\lambda_{NF=1}$ falls within the minimum region of the resolution curve, is indistinguishable from heuristic selections, and consistently results in good reconstructions.

4.5.2 Clinical Considerations

The *BestRes* method is intended to preserve information in the data through compensation of the ill-conditioning of the sensitivity matrix, given a fixed noise level in the data. As

a hyperparameter selection method, *BestRes* does not consider problems associated with equipment such as uncertain electrode positioning, electrode and cable problems, and electromagnetic interference (EMI) from other sources in the clinical environment. The problem of uncertain electrode positioning is mitigated primarily by using difference measurements and should not be addressed through hyperparameter adjustments. Electrode and cable errors are best addressed by detecting the problem and alerting an operator to fix it, or by compensating for the problem *a posteriori* through use of an algorithm such as that of [7]. Excessive EMI in a clinical environment [89] will swamp the signal such that extraction of information is impossible regardless of hyperparameter. The *BestRes* method is a calibration technique to choose a hyperparameter based on a noise level that is fixed, regardless of whether the noise is representative of clinical data or added to simulated data.

4.5.3 Effect of radial position on $\lambda_{BestRes}$

Figure 4.10 is a plot of Resolution and λ_{BestRes} as a function of radial position of the generating contrast. These curves were generated by reconstructing a set of simulated data generated by an impulse contrast located at increasing radial positions. The best resolution is achieved for contrasts located at 75% of radial distance from the centre. Although λ_{BestRes} continues to increase as the radial position increases past 90%, the corresponding resolution starts to decrease due to blurring caused by proximity to the edge.

4.5.3.1 Normalization

Although primarily concerned with proportional (normalized) difference imaging we also investigated the performance of the Fixed NF method using simple (non-normalized) difference algorithms. The simple difference problem is solved using equation 4.2 with $\mathbf{x}$ defined as $\mathbf{x} = \boldsymbol{\sigma_2} - \boldsymbol{\sigma_1}$ and $\mathbf{z}$ defined as $\mathbf{z} = \mathbf{v_2} - \mathbf{v_1}$. ($\mathbf{H}$ is also modified in that its columns are not divided by $\mathbf{v_{ref}}$ as in section 4.2). Similar to the proportional difference algorithm the Fixed NF method was able to consistently calculate a hyperparameter located in the minimum region of the associated resolution curve.

Comment on Normalization

Normalization has some advantages. By normalizing the data, one does not need to know the amplitude current injected. Thus, the forward problem can be solved using a value of injected current which is convenient for the algorithm (usually ± 1). The authors of [90] justify normalization with the argument that a normalized sensitivity matrix is less sensitive to the boundary shape of the object and the position of the electrodes, which is a substantial problem in clinical applications. Also, some EIT systems change the gain settings for each electrode depending on the amplitude of signal expected. Normalization can compensate for these cases as well as instances where the calibrated gain settings are not exact.

Normalization of the sensitivity matrix does not change the spectrum of singular values of $\mathbf{H^T H}$. Although the condition number of $\mathbf{H^T H}$ may improve by an order of magnitude or more the relative change is not significant. For the meshes used in this work the condition number of $\mathbf{H^T H}$ improved by a factor of about 10. In other work involving non-circular meshes we have seen changes from as low as 1.5 to as high as 1000. In some cases (non-homogenous background conductivity) the condition number increased, so it is not possible to state that, as a rule, normalization always improves the condition number of $\mathbf{H^T H}$.

4.5.3.2 Nonlinear Reconstructions

We investigated the use of the fixed NF method with an iterative static reconstruction algorithm. In this experiment we used fixed NF to calculate a single hyperparameter that was used for each iteration. Running the algorithm to convergence indicated that the $\lambda_{NF=1}$ was located in the minimum region of the resolution curve. It may be possible to use the fixed NF method to calculate a new hyperparameter for each step of the iterative algorithm, however, this was not pursued.

4.5.3.3 Inverse Crime

The act of employing the same model to generate, as well as to invert, simulated data is known as an *inverse crime* [122]. In this work, data were simulated using a 1968 element mesh, so reconstructions using the same mesh constitute an inverse crime. Such reconstructions had noticeably better resolution than was achieved with other meshes and, as shown in figures 4.11(a) and 4.11(b), exhibited $\lambda_{BestRes}$ and λ_{LC} corresponding to an uncharacteristically high NF. This suggests a method to detect inverse crimes: using the suspect FEM, and associated data, construct a resolution curve or L-curve with the simulated data and calculate the NF corresponding to $\lambda_{BestRes}$ or λ_{LC}. If the $NF >> 3$ (for example, figure 4.11(a) had $NF > 7$) it is likely that the reconstruction algorithm is committing an inverse crime. The method was validated by the observation that reconstructions over the 1968 element mesh using tank data did not exhibit the large NF bias while the high NF phenomenon was observed every an "inverse crime" configuration was analyzed. One explanation for these results is that the optimal hyperparameter for the inverse crime case is significantly lower than that generally required, since the geometry matching between forward and inverse solutions is giving a regularizing effect.

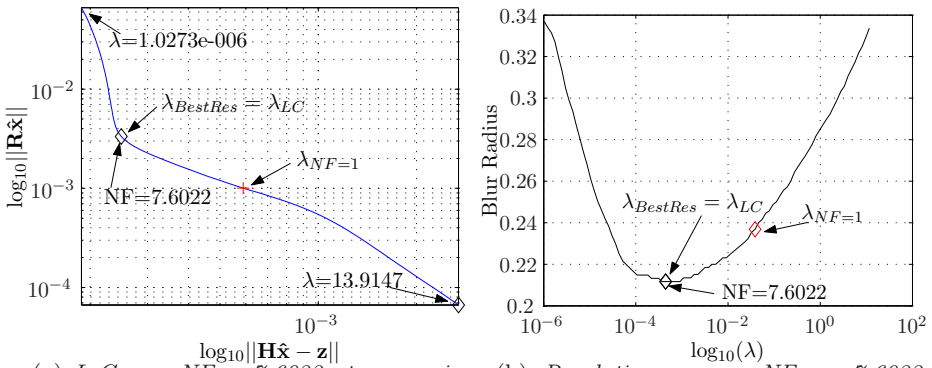

(a) *L-Curve, NF = 7.6022 at corner is excessive and indicates inverse crime*

(b) *Resolution curve, NF = 7.6022 is excessive and indicates an inverse crime.*

Figure 4.11: *Either the L-curve or resolution curve can be used to detect an inverse crime.*

4.6 Conclusion

This paper proposes a new method of objective hyperparameter selection for use in one-step image reconstructions and compares it to some existing methods including heuristic selection. We present the following observations:

1. Heuristic selections of hyperparameter are inconsistent among experts and unrepeatable. This suggests that there is no single preferred value of λ, rather there is a preferred region of λ over which reconstructions are not subjectively distinguishable. Moreover, it was not possible for observers to differentiate reconstructions based on heuristic hyperparameter selections from those produced from the objective methods.

2. The GCV method is unreliable for the class of algorithms used in this work.

3. The L-Curve is, in general, shallow for EIT applications and is not reliable for all configurations (doesn't indicate a hyperparameter). When the method does work it provides a lower hyperparameter value than the Fixed NF and *BestRes* methods.

4. With $NF = 1$ the Fixed NF Method calculates a hyperparameter that falls in the minimum region of the Resolution Curve. At low noise levels $\lambda_{NF=1}$ is very close to $\lambda_{BestRes}$. As AWGN is added to the simulated data $\lambda_{BestRes}$ increases while $\lambda_{NF=1}$ remains constant. However at the noise level found in our EIT equipment a NF of 1 produces good reconstructions that are close to the optimal reconstructions achieved with *BestRes* method.

5. The Fixed NF Method provides a configuration independent method to select λ that is repeatable and is more consistent than expert selection. One could use the Fixed NF method with $NF = 1$ to calculate a minimum hyperparameter value for any configuration. This method is repeatable and in applications with realistic noise levels will produce consistent stable reconstructions that are as good as heuristic selection.

6. Hyperparameters taken from the minimum region of the Resolution Curve (*BestRes* method) always produce good solutions that are comparable to, but more consistent than expert selections. Moreover $\lambda_{BestRes}$ is optimal in terms of our figure of merit.

For the class of regularized reconstruction algorithms used in this work both the Fixed NF and *BestRes* methods provide objective methods to select a good value for λ. The values were indistinguishable from those selected by human experts. Both methods were developed using simulated data but shown to be applicable (validated) using Tank data.

Although these methods do not completely solve the problem of obtaining an optimal hyperparameter value, they do provide a rationale and method for objectively and automatically selecting λ. Using the *BestRes* method with imaging equipment provides a sound engineering method for manufacturers or researchers to obtain a configuration-dependent hyperparameter that is optimal in terms of resolution. This allows end users to perform impedance imaging without the necessity of having to manually tweak parameters.

Chapter 5

A Nodal Jacobian Inverse Solver for Reduced Complexity EIT Reconstructions

This chapter is the text, with minor revisions, of a paper titled "A Nodal Jacobian Inverse Solver for Reduced Complexity EIT Reconstructions" by Bradley GRAHAM and Andy ADLER published in the International Journal of Information & Systems Sciences, Special Issue on Computational Aspect of Soft Field Tomography, Volume 2, Number 4 (2006).

This paper addresses the problem of solving increased resolution, high density, 3D EIT models (section 1.3 objective O2 and section 1.4.1 Contributions by Objective O2): develop an algorithm that reduces the execution time and memory required to calculate reconstructions using dense high resolution 3D finite element models.

In [77] Kaipo *et al* use a 2D finite element model based on a piecewise linear discretization of the conductivity as opposed to the more common piecewise constant conductivity model that is used in element based solvers. Such models lead to a Jacobian matrix that scales with the number of nodes in a model instead of the much larger number of elements, the consequence of which is a large reduction in the computational complexity of the resulting linear system. The main contribution of this objective is the development of *Nodal Jacobian Inverse Solver*, which is an algorithm for efficiently calculating a nodal Jacobian which is used to reduce the complexity of the EIT reconstruction problem. Additional contributions include the systematic evaluation of the algorithm's performance in both 2 and 3 dimensions.

Abstract

Electrical impedance tomography (EIT) uses surface electrodes to make measurements from which an image of the conductivity distribution within some medium is calculated. Calculation of conductivity solutions requires inverting large linear systems that have to date restricted reconstructions to 2D or coarse 3D domains. This paper presents a Nodal Jacobian Inverse Solver that scales with the number of nodes in a finite element mesh rather than with the number of elements. For the example used in this paper the size of the linear system is reduced by a factor of 26. We validate the algorithm by comparing its performance to traditional 2D Elemental Jacobian algorithms. We then analyze its performance with a 21504 element 3D mesh that is too large to be solved with linear algebra systems based on 32 bit pointers (such as is available in current versions of Matlab). Finally, we demonstrate the applicability of the algorithm for clinical use by reconstructing experimentally measured

human lung data.

Keywords: regularization, 3D, EIT, hyperparameter, Jacobian

5.1 Introduction

Electrical Impedance Tomography (EIT) uses body surface electrodes to make measurements from which an image of the conductivity distribution within some medium is calculated. Calculation of conductivity solutions using one of the Newton type methods requires inverting large linear systems derived from finite element models of the medium under analysis. The Hessian matrix in these linear systems scale with the square of number of elements in the model and the square of the number of measurements used in the reconstruction. Almost all EIT algorithms use a piecewise constant conductivity model, in which the conductivity is considered to be constant over an element. The large number of elements required and large number of measurements available for 3D reconstructions have to date restricted 3D reconstructions to coarse, low resolution models. Complex, accurate geometries, *a priori* structures, the increased number of measurements possible with newer machines and the desire for improved resolution in the third dimension leads to a requirement to solve large 3D models. Such reconstructions are beyond the capability of contemporary computers such as the AMD Athlon 64 3000+, 2GB RAM computers used in our lab. Thus the development of algorithms that can efficiently calculate full 3D solutions over dense finite element models with many measurements is required.

In this paper we present and evaluate a *Nodal Jacobian Inverse Solver* algorithm that reduces the execution time and memory required to calculate reconstructions. In addition to gains in reconstruction efficiency, the extraction and display of data stored in the nodal format is much quicker than for data stored in the elemental format. Moreover, nodal solutions are easily processed using pixel based filtering algorithms similar to those used in image processing work.

The finite element model used in this work includes a mesh that has a simple cylindrical geometry but is comprised of over 20,000 elements. This high mesh density is not warranted for a 16 electrode-208 measurement protocol, however it is used in this work to show the performance improvement possible using the proposed solver. It is expected that applications that use many electrodes or require huge numbers of elements to model complex geometries will be able exploit the performance benefits of the proposed algorithm.

5.2 Methods

This paper introduces the *Nodal Jacobian Inverse Solver* as follows. In the methods section we describe the traditional family of EIT reconstruction algorithms used in our research, describe the *Nodal Jacobian* variation of this family of algorithms, and describe the evaluation procedure. In the results we describe the effectiveness of the new family of algorithms compared to the traditional algorithms. In the discussion we consider some additional observations of this work and conclude with a recommendation of the proposed algorithm.

5.2.1 Data Acquisition

Lab data used in this paper was obtained using a 16 electrode adjacent drive EIT machine (the Goe-MF II type tomography system, Viasys Healthcare, Höchberg, Germany) designed

for use with 2D reconstruction algorithms based on data from electrodes placed in a planar section of the medium as shown in figure 5.1(a). Adjacent current stimulation is used with adjacent voltage measurement at all remaining electrodes except the driven electrode pair. The general formula for the number of measurements, M, obtained using this type of injection-measurement protocol is $M = (N_{el} - 3)/N_{el}$ where N_{el} is the number of electrodes. For 16 electrodes, 208 measurements are available per frame, while for a 32 electrode system the number of available measurements is 928. Although the 16 injection-measurement patterns are obtained over a finite time interval, 80ms for the Goe-MF II, the entire vector of 208 measurements is treated as representing the boundary voltages at a single instant in time and is considered a *frame* of data.

Data obtained from a 2D electrode placement such as in figure 5.1(a) is most often used to calculate a 2D estimate of the conductivity although a 3D reconstruction algorithm could use these data. By placing the electrodes in multiple planes 2D equipment can be used to acquire data that are better suited for 3D reconstructions. One such method is the hybrid electrode placement strategy (described in chapter 6) shown in figure 5.1(b) in which electrodes are placed in two axially aligned planes with the 16 electrodes connected sequentially as shown by the numbers in the figure. This arrangement will result in an inter-plane injection-measurements between electrodes 8 and 9 as well as 16 and 1. This strategy is used in this work in order to validate some of the simulated results with lab data collected using the Goe-MF II. The choice of 2 electrode planes was mainly one of simplicity and convenience. Many other electrode placement strategies are possible. The EIDORS v3 suite [8], using the Complete Electrode Model, was extended to perform the work in this paper.

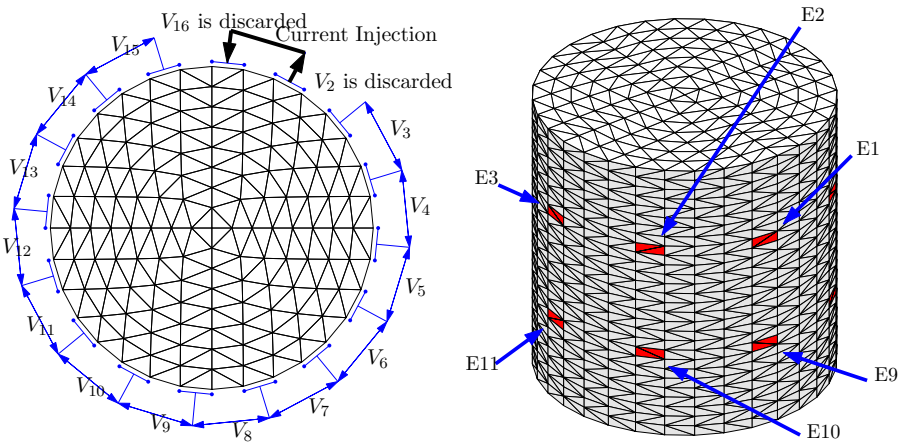

(a) *2D adjacent drive protocol showing current injection between electrodes 1 and 2 with and 13 individual measurements being made betwene the remaining electrodes.*

(b) *(b) Hybrid 3D adjacent drive protocol. Finite Element mesh has 28 layers with a total or 21504 elements and 4205 nodes. Electrodes are arranged in two layers of 8 electrodes.*

Figure 5.1: *2D and 3D Finite Element meshes.*

5.2.2 EIT Modeling

We consider EIT difference imaging, which is widely understood to improve reconstructed image stability in the presence of problems such as unknown contact impedance, inaccurate electrode positions, non linearity, and the use of 2D approximations for 3D electrical

fields when reconstructing in 2D [18][87]. We address the class of one-step linearized reconstruction algorithms that calculate the change in a finite element conductivity distribution $\mathbf{x} = \sigma_\mathbf{2} - \sigma_\mathbf{1}$ indicated by a measured change in difference signal, $\mathbf{z} = \mathbf{v_2} - \mathbf{v_1}$, over a time interval (t_1, t_2). By convention we consider the signal at t_1 to be the *reference* frame and the signal at t_2 to be the *data* frame. Since we do not know $\sigma_\mathbf{1}$, $\mathbf{x}$ is interpreted as the change in conductivity with respect to the unknown initial conductivity $\mathbf{x} = \mathbf{\Delta}\sigma$.

A forward model is required when one wants to solve the non-linear problem, generate simulated data or calculate the Jacobian using the efficient method described in [98] that requires calculation of the electric fields in the interior of the object. Using the finite element method (FEM), the voltage distribution at E electrodes is simulated by current injection into the medium with a conductivity distribution discretized on N finite elements. This model of the forward problem accepts a vector of conductivity values and calculates the voltage V_{ij} at each node i for each current injection pattern j through the linear equation

$$\mathbf{V} = \mathbf{Y}(\sigma)^{-\mathbf{1}}\mathbf{I} \tag{5.1}$$

where $\mathbf{Y}(\sigma)$ is the admittance matrix of the FEM and I_{ij} is the current at each node i during current injection pattern j. With the point electrode model each electrode is modeled as a single boundary node, thus the columns of I have only two non-zero entries corresponding to the current injected at the two electrodes. Calculation of the vector $\mathbf{v}$ of M voltage differences is represented by $\mathbf{v} = T[\mathbf{V}(\sigma)]$. For instance if v_9 is defined to correspond to the voltage difference between electrodes 4 and 5 during injection pattern 2, then the operator T will give $T[\boldsymbol{V}]_9 = \boldsymbol{V}_{42} - \boldsymbol{V}_{52}$.

The most accurate mathematical model for EIT is the Complete Electrode Model (CEM)

$$\begin{bmatrix} \mathrm{A}_M + \mathrm{A}_Z & \mathrm{A}_W \\ \mathrm{A}_W^T & \mathrm{A}_M \end{bmatrix} \begin{bmatrix} \Phi \\ \mathrm{V} \end{bmatrix} = \begin{bmatrix} 0 \\ \mathrm{I} \end{bmatrix} \tag{5.2}$$

where A_M, A_W, and A_Z represent the CEM boundary conditions. In this paper we use the point electrode model for the 2D experiments and the CEM for the 3D experiments. A complete derivation of the CEM can be found in [114] however the salient point is that in equation 5.1 and 5.2 $\mathrm{A}_M = \mathrm{Y}$ is the N by N symmetric admittance matrix given by

$$Y_{ij} = \int_\Omega \sigma \nabla w_i \cdot \nabla w_j d\Omega \tag{5.3}$$

where w_i is a linear basis function with value 1 on i^{th} node and 0 elsewhere. In the majority of cases σ is considered constant on each element (piecewise constant) which allows σ to be brought outside the integral in 5.3

$$Y_{ij} = \sum_{k=1}^{N} \sigma_k \int_{\Omega_k} \nabla w_i \cdot \nabla w_j d\Omega_k \tag{5.4}$$

The integral in 5.4 is calculated analytically for each element with each element contributing 9 (for a triangle) or 16 (for a tetrahedron) entries to the master admittance matrix Y.

For small changes around a background conductivity the relationship between $\mathbf{x}$ and $\mathbf{z}$ may be linearized as

$$\mathbf{z} = \mathbf{H}\mathbf{x} + \mathbf{n} \tag{5.5}$$

where $\mathbf{H}$ is the Jacobian or sensitivity matrix and $\mathbf{n}$ is the measurement system noise, assumed to be uncorrelated additive white Gaussian (AWGN).

For piecewise constant conductivity models, each element i, j, of $\mathbf{H}$ is defined as $H_{ij} = \frac{\partial z_i}{\partial x_j}\Big|_{\sigma_0}$ and relates a small change in the i^{th} difference measurement to a small change in the conductivity of j^{th} element with respect to a background conductivity vector, $\sigma_\mathbf{0}$. $\mathbf{H}$ is a function of the FEM, the current injection pattern, the measurement pattern, and the background conductivity. We use the adjacent current injection pattern and a homogenous background conductivity with $\boldsymbol{\sigma}_0 = 1$ for each of the elements. $\mathbf{H}$ is a matrix comprised of E columns of length M where E is the number of elements in the finite element model and M is the number of measurements per frame. Thus the i^{th} column represents the change in the M boundary measurements due to a change in the conductivity of the i^{th} element. There are several ways to calculate the Jacobian; the EIDORS2D toolset [116] uses the method of [114][127] (which is referred to as the *Standard Method*) whereas the EIDORS3D toolset [93] uses a more efficient method involving the dot products of the interior electric fields.

5.2.3 Image Reconstruction

In order to overcome the ill-conditioning of $\mathbf{H}$ we solve 5.5 using the following regularized inverse originally described in [4]

$$\hat{\mathbf{x}} = (\mathbf{H}^T\mathbf{W}\mathbf{H} + \lambda^2\mathbf{R})^{-\mathbf{1}}\mathbf{H}^T\mathbf{W}\mathbf{z} = \mathbf{B}\mathbf{z} \tag{5.6}$$

where $\hat{\mathbf{x}}$ is an estimate of the true change in conductivity, $\mathbf{R}$ is a regularization matrix, λ is a scalar hyper parameter that controls the amount of regularization, and $\mathbf{W}$ models the system noise covariance. We calculate λ using the *BestRes* algorithm described in chapter 4. Noise is modeled as uncorrelated with conductivity changes and among measurement channels; thus, $\mathbf{W}$ is a diagonal matrix with $W_{i,i} = 1/\sigma_i^2$ where σ_i^2 is the noise variance for measurement i. $\mathbf{W}$ can also be modified to account for variable gain settings on each tomograph channel. With $\mathbf{R} = \mathbf{I}$ (labelled $\mathbf{R}_{Tik}$) equation 5.6 is the 0^{th} order Tikhonov algorithm. With $\mathbf{R} = diag(\mathbf{H}^T\mathbf{H})$ (labelled $\mathbf{R}_{diag}$) equation 5.6 is the regularization matrix used in the NOSER algorithm [35]. In [4] $\mathbf{R}$ is a model of the inverse *a priori* image covariance. EIT has the potential for only a relatively few independent measurements. As a direct consequence there will be limited high spatial frequency content and therefore low spatial resolution, associated with any reconstructed image. This implies that the elements with a separation less than the minimum recoverable spatial period (EIT resolution) are highly correlated. Consequently Adler and Guardo [4] model $\mathbf{R}$ as a spatially invariant Gaussian high pass filter (labelled $\mathbf{R}_{HPF}$) with a cut-off frequency selected so the spatial period is a given fraction of the medium diameter. In two dimensions a Gaussian high pass filter of spatial frequency ω_0 has the form

$$\mathbf{F}(u, v) = 1 - e^{-\omega_0(u^2+v^2)} \tag{5.7}$$

In the spatial domain the convolution kernel is

$$f(x, y) = \delta(x, y) - \frac{\pi}{\omega_0^2}e^{-\left(\pi^2/\omega_0^2\right)\left(x^2+y^2\right)} \tag{5.8}$$

where $\delta(x, y)$ is the Dirac delta function. The filtering matrix $\mathbf{F}$ multiplies an image vector $\mathbf{x}$ to give a filtered image $\mathbf{F}\mathbf{x}$. F_{ij} is calculated by centering the high pass filter in element

i and integrating across element j

$$F_{ij} = \int_{E_j} \left[\delta\left(x - x_i, y - y_i\right) - \frac{\pi}{\omega_0^2} e^{-\left(\pi^2/\omega_0^2\right)\left((x-x_i)^2+(y-y_i)^2\right)} \right] dxdy \tag{5.9}$$

This integration is performed numerically on a mesh of 512×512 points superimposed over the 2D FEM. We define this as an integration density of 512 points per linear unit or 512^2 points per square unit. The filter cut-off frequency is expressed in terms of the percentage of the diameter. Using a mesh of N_p points

$$(\%\text{ diameter}) = \frac{N_p}{2\pi\omega_0} \tag{5.10}$$

The regularization matrix is calculated as $\mathbf{R}_{HPF} = \mathbf{F}^T\mathbf{F}$. This filter could be extended to 3D by including the z component in equation 5.9 and integrating numerically over a mesh of integration density 512^3 points per cubic unit; however we do not use a 3D version of the Gaussian filter in this paper.

Although all three of these priors are smoothing filters which attenuate the contribution of the high frequency components of the SVD of $\mathbf{H}^T\mathbf{H}$, the Gaussian high pass filter has the advantage of being mesh size and mesh shape independent in that it is a function of the area weighted mesh inter-element correlations.

5.2.4 Nodal Jacobian

As the number of elements in a FEM increases, the time and memory required to calculate the solution increases, such that solving problems of useful resolution in 3D becomes difficult or impossible to perform. For example the term $\mathbf{H}^T\mathbf{W}\mathbf{H}$, in equation 5.6 for the 21504 element FEM of figure 5.1(b) produces a matrix of size 21504×21504 which exceeds the memory capabilities of 32-bit matrix indexing arithmetic, such as is currently available in Matlab software.

The ratio of nodes to elements can be up to a factor of two for 2D FEM meshes; the sum of angles in a triangle is 180, a point has 360 degrees, thus a dense mesh will tend to have an element to node ratio of two. In 3D a point has a solid angle of 4π, six tetrahedra fit into a cube (solid angle of 4π); a tetrahedron therefore has solid angle of $4\pi/6$. Thus a dense mesh will tend to have an element to node ratio of six although practical meshes will have a lower ratio; the 3D mesh used in this paper has an element to node ratio of 5.1. The incentive to develop an algorithm that scales with the number of nodes rather than the number of elements is the fact that the size of the Hessian matrix will be reduced by the square of the element to node ratio. Thus the Hessian matrix for the 3D mesh used in this paper will be reduced by a factor of 26 which is sufficient to allow it to be formed within the 32-bit matrix indexing environment of Matlab.

The construction of a *Nodal Jacobian* is based on the development of a nodal finite element model. In [77] Kaipo *et al* use a 2D finite element model based on a piecewise linear discretization of the conductivity in which the conductivity of an element is linearly interpolated throughout its volume based on the conductivity values at its vertices. The adoption of piecewise linear conductivity on each element means that the conductivity cannot be brought outside the integral in equation 5.3 thus equation 5.4 cannot be used to calculate the admittance matrix rather we must solve

$$Y_{ij} = \sum_{k=1}^{N} \int_{\Omega_k} \sigma_k(\vec{r}) \nabla w_i \cdot \nabla w_j d\Omega_k \tag{5.11}$$

where $\vec{r}$ is a position vector within element k. For an inhomogenous isotropic material $\sigma_k(\tilde{\mathrm{r}})$ is a conductivity tensor of the form $\sigma_k(\tilde{\mathrm{r}}) = \sigma_k(\tilde{\mathrm{r}})\mathbf{I}$ where $\tilde{\mathrm{r}}$ is a scalar function of the conductivity and $\mathbf{I}$ is the identity matrix.

In [77] Kaipo *et al* use the same linear basis functions, w_i, for σ as are used for the potential. In [77] the authors do not discuss or exploit the complexity improvement associated with using the nodal basis. Their use of piecewise linear conductivity was motivated by a requirement to calculate the gradient of the conductivity within each element for the purposes of incorporating a structural prior into their reconstructions. By using a piecewise linear conductivity model the gradient over each element is a constant. An implementation of the piecewise linear element is available in the EIDORS2D toolset [116] in which $\mathbf{Y}$ is calculated from equation 5.11. Also provided is a function to calculate the corresponding Nodal Jacobian using the *Standard Method*.

EIDORS3D [93] calculates an Elemental Jacobian using the NSHI (nullspace scaled hybrid isotropic) algorithm described in [121]. The NSHI algorithm is over **60** times faster than the *Standard Method* for the example cited in [98] but requires components calculated from an element based master matrix. Thus in order to retain the speed advantage of the NSHI algorithm, we adapted the EIDORS2D nodal master matrix construction algorithm to construct a Nodal Jacobian, H^N, from the elemental Jacobian, H^E, as follows:

1 $d = 3$ for triangles or $d = 4$ for tetrahedrons

2 for each node, n, in the mesh

3 elems=list of elements using node n

4 $\mathrm{H}^N_{:,n} = \sum_{i \in \text{elems}} {}^1\!/_d \mathrm{H}^E_{:,i}$ where $\mathrm{H}_{:,i}$ means the i^{th} column of matrix $\mathbf{H}$.

5 end for each node

Intuitively this can thought of as having each element contribute an equal proportion of its sensitivity to each of its three or four contained vertices.

When using the *Nodal Jacobian* in the regularized inverse 5.6 the resulting solution will be in the nodal basis. It is possible to convert the nodal solution back to a piecewise constant element basis where it is determined by E parameters. Conversion back to an elemental basis can be done by setting the conductivity value for each element to an average of the conductivity values of its enclosing vertices. This has the advantage of being simple to implement and works well for meshes constructed of regularly spaced nodes. It is also possible to weigh the average as a function of subtended angle or Voronoi cell area. In either case the conversion to an elemental solution will introduce additional smoothing through local averaging which may or may not be desirable. In this paper we maintain solutions in the nodal basis.

Two advantages of the nodal basis are the ability to store the solution in a smaller number of parameters, and the ability to rapidly extract and render graphical displays of solutions using a function such as Matlab's built-in *trisurf* function. The *trisurf* function takes as input a list of vertices and associated values at each vertex. No explicit knowledge of the geometry is required, such as an element list providing connectedness between nodes, in order to display cut planes of coplanar nodes. For example the 3D model of figure 5.1(a) has coplanar nodes at each of its 29 nodal layers as well as coplanar nodes at vertical slices such as $x = 0$ and $y = 0$ and other angles. Figure 5.7(a) shows three multiplane conductivity representations of figure 5.1(b) that were rendered by *trisurf* in real time (60ms each).

5.2.5 Nodal Gaussian Filter

The Gaussian High Pass filter, $\mathbf{R}_{HPF}$, of [4] can be extended to work over the nodes of the mesh as opposed to the elements. The regularization matrix is $\mathbf{R}_{HPF} = \mathbf{F}^T\mathbf{F}$ where F_{ij} is calculated by centering the high pass filter at node i and integrating across the Voronoi cell of node j in accordance with equation 5.9. As with equation 5.9 the filter cut-off frequency is expressed in terms of the percentage of the diameter in accordance with equation 5.10. This filter is extended to 3D by including the z component in equation 5.9 and integrating over the Voronoi polyhedra of node j. A Voronoi cell is a polygon (polyhedra in 3D) whose interior consists of all points in the plane (hyper plane in 3D) which are closer to a particular node than to any other. Figure 5.2(b) shows part of a Voronoi diagram for a 64 element, 41 node FEM of figure 5.2(a). Note that there are no closed Voronoi cells for the nodes located on the boundary since they are by definition unbounded and extend to infinity. To overcome this problem for the 2D mesh, we add a set of auxiliary nodes by replicating the boundary nodes but located radially offset from the original location by a small distance (0.00001 was used for a mesh of diameter 1). Figure 5.2(c) is for illustrative purposes and shows the auxiliary nodes at an exaggerated stand off distance resulting in additional closed Voronoi cells. Figure 5.2(d) shows the auxiliary nodes located almost coincident with the boundary nodes which brings the outer Voronoi cell edge close to the boundary of the original mesh. The Voronoi cells, including the cells added through the auxiliary nodes, are used as the domain of integration for the Gaussian filter calculations. Note that it would also be possible to integrate each element in $\mathbf{F}$ over the basis function of each FEM node.

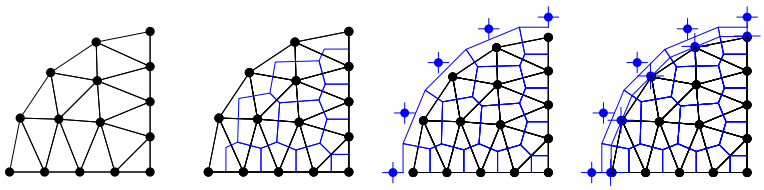

Figure 5.2: *One quarter of a 2D FEM showing development of Voronoi Cells for boundary nodes.*

The 3D models used in this work are constructed by using layers of nodes that are replicated and shifted versions of the nodes of an initial 2D mesh. The 3D Voronoi cell for such a mesh is an extruded version of the 2D Voronoi cell. This permits the numerical integration of the 3D Gaussian filter using equation 5.9. We use equation 5.9 and integrate with an integration density of 512^3 points per cubic unit.

5.2.6 Laplacian Mask Filter

A further advantage of a nodal basis is that it facilitates the use of filters derived from pixel oriented domains such as found in the image processing literature. Rather than develop a low pass filter and then invert it, we follow the method of [4] and develop a high pass filter directly (based on the Laplacian mask described in [60] labelled $\mathbf{R}_{Lap}$ that is subsequently inverted in equation 5.6. We define the region of support for the Laplacian as nodes located with in a radius of some percentage of medium diameter. In this work we use 10%, a number arrived at through experience. The filtered value for node i is calculated as follows

$$\hat{x}'(i) = (1 - \hat{x}(i)) \sum_{n \in \Omega_i} \hat{x}(n)(r/d_n) \tag{5.12}$$

where $\hat{x}(i)$ is the prior value of node i, r is the radius of the neighbourhood, d is distance between node i and node n. Ω_i represents the radial neighbourhood of node i; members of the set Ω are nodes that are located within a distance r of node i. $n \in \Omega_i$ means that n belongs to the radial neighbourhood of node i. r/d_n is a weighing of the nodal value. This formulation for a Laplacian filter is mesh size independent which is different from the discrete Laplacian filters used in [93] and [25].

5.2.7 Smoothing Mask Filter

In addition to the filters used directly in the regularized inverse it is also possible to apply a spatial smoothing filter, $\mathbf{R}_{LP}$, to the nodal solutions of equation 5.6 by multiplying the solution with the low pass filter. This can be treated as a post processing step that increases the signal-to-noise ratio (SNR) of the solution. This filter is implemented through matrix multiplication as $\hat{\mathbf{x}}' = \mathbf{R}_{LP}^k \hat{\mathbf{x}}$. The exponent k indicates that this filter can be applied multiple times. In this paper we use $k = 1$ but other values are possible. $\mathbf{R}_{LP}$ calculates a filtered value for node i as follows

$$\hat{x}'(i) = \sum_{n \in \Omega_i} \hat{x}(n) / \|\Omega_i\| \tag{5.13}$$

where $n \in \Omega_i$ means that n is a member of the radial neighbourhood of node i including node i and $\|\Omega_i\|$ means the number of members of Ω_i. We incorporate $\mathbf{R}_{LP}$ into equation 5.6 before hyperparameter selection. Thus equation 5.6 with $\mathbf{W} = \mathbf{I}$ is restated as

$$\hat{\mathbf{x}} = \mathbf{R}_{LP}^k (\mathbf{H}^T \mathbf{H} + \lambda^2 \mathbf{R})^{-\mathbf{1}} \mathbf{H}^T \mathbf{z} \tag{5.14}$$

with hyperparameter selected using the *BestRes* algorithm described in chapter 4. The complete algorithm can then be performed with any $\mathbf{z}$.

5.2.8 Evaluation Procedure

In order to evaluate the performance of this algorithm, the following test procedures were conducted.

1. Initially we validate the performance of the new algorithm by comparing its performance to the traditional algorithm for 2D reconstructions using tank data of a pseudo-impulse phantom. Comparisons are made between the nodal and elemental Jacobians using the $\mathbf{R}_{Tik}$, $\mathbf{R}_{diag}$, $\mathbf{R}_{HPF}$ and $\mathbf{R}_{Lap}$ priors.

2. We validate the 2D hyperparameter selection method, *BestRes*, (chapter 4) for 3D reconstructions.

3. We quantify the performance of the 3D nodal algorithm using the $\mathbf{R}_{Tik}$, $\mathbf{R}_{diag}$, $\mathbf{R}_{HPF}$ and $\mathbf{R}_{Lap}$ priors, with two sets of simulated impulse phantom data. Both sets of simulated data were created by moving an impulse contrast through 28 vertical positions of a 28 layer, 86016 element, 15805 node FEM that is similar to, but denser than the FEM of figure 5.1(b). Reconstructions are made using the 21504 element mesh of figure 5.1(b) One set of data had the impulse contrasts located at the axial center ($r = 0$), the second set of data had the contrasts located halfway between the axial center and the tank boundary ($r/2$).

4. Finally we validate the *Nodal Jacobian* algorithm with some lab data of human lungs.

Quantitative figures of merit are required in order to compare the accuracy of the reconstructed images. Several figures of merit for EIT proposed in the literature were reviewed in [120]. The primary figures of merit used in this work are resolution, image energy, and signal to noise ratio of the reconstruction. We define *resolution* in terms of blur radius (BR). BR calculates the area fraction of the elements that contain the largest amplitude contributions to 50% of the total image amplitude and is therefore a measure of the concentration of image amplitude. BR is defined as $BR = r_z/r_0 = \sqrt[3]{V_z/V_0}$ for 3D, where r_0 and V_0 are the radius and volume respectively of the entire medium and r_z and V_z are the radius and volume of the reconstructed contrast containing half the magnitude of the reconstructed image [4]. In 2D, V represents area and a square root is taken. Image Energy, an arbitrary but global measure, is defined as $P = \sum_i \hat{x}_i^2 V_i$. For elemental solutions $\hat{x}_i$ is the solution amplitude at element i, while for nodal solutions $\hat{x}_i$ is the solution amplitude at node i. Signal to Noise Ratio is defined as $SNR = \overline{\hat{\mathrm{x}}\mathrm{V}}/\sigma_{\hat{\mathrm{x}}\mathrm{V}}$ which is the volume weighted, solution mean over the volume weighted, solution standard deviation). Again area is used for 2D. For elemental solutions the area and volumes used are those of the element triangles (2D) and tetrahedrons (3D), for nodal solutions the Voronoi cell area is used in 2D while the extruded Voronoi cell is used for 3D.

5.3 Results

5.3.1 2D Results

We initially validated the performance of the nodal algorithm by calculating 2D reconstructions using data collected from a single plane of electrodes arranged around the middle of a tank. This is 3D tank data reconstructed with the assumption that the fields are confined in 2D. The phantom data used are from a 2cm non-conductive sphere located at r/2 in a tank of diameter 29cm and height 29cm. Data were collected using the Goe-MF II using the adjacent protocol described in section 5.2.1. Figure 5.3 shows reconstructions made using the $\mathbf{R}_{Tik}$, $\mathbf{R}_{diag}$, and $\mathbf{R}_{HPF}$ priors with the element based Jacobian. Figure 5.4 shows the same data reconstructed over the same mesh using the nodal based Jacobian and the $\mathbf{R}_{Tik}$, $\mathbf{R}_{diag}$, $\mathbf{R}_{HPF}$ and $\mathbf{R}_{Lap}$ priors. Resolution and signal to noise ratio are indicated in the figures.

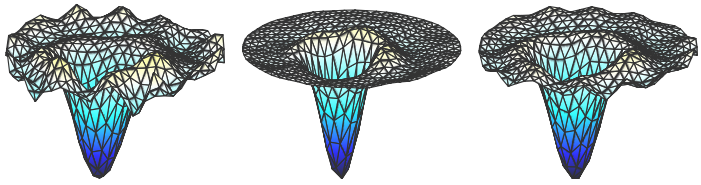

(a) $\mathbf{R}_{Tik}$ *BR=.309, SNR=.450*

(b) $\mathbf{R}_{diag}$ *BR=.233, SNR=.337*

(c) $\mathbf{R}_{HPF}$ *BR=.279, SNR=.444*

Figure 5.3: *Comparison of 2D Elemental reconstructions using tank data for different filters and Jacobians using 1024 element mesh. Reconstructions are normalized so that the vertical axis and color scales are maximized.*

Figures 5.3 and 5.4 show reconstructions normalized so that the vertical axis and color scales are maximized. The nodal algorithms produce much larger peak signals than the

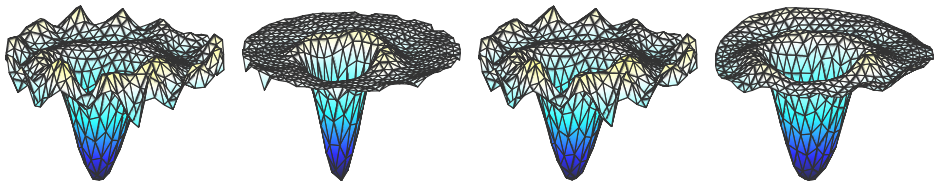

(a) $\mathbf{R}_{Tik}$ *BR=.328, SNR=.462*

(b) $\mathbf{R}_{diag}$ *BR=.236, SNR=.332*

(c) $\mathbf{R}_{HPF}$ *BR=.324, SNR=.440*

(d) $\mathbf{R}_{Lap}$ *BR=.296, SNR=.485*

Figure 5.4: *Comparison of 2D Nodal reconstructions using tank data for different filters and Jacobians using 1024 element mesh. Reconstructions are normalized so that the vertical axis and color scales are maximized.*

corresponding elemental solutions; however, this can be compensated for through normalization which is how the solutions of figures 5.3 and 5.4 are displayed. Resolution and SNR are better discriminators between algorithms. The elemental Jacobian algorithm with a $\mathbf{R}_{diag}$ prior is the best all around reconstruction in terms of resolution. The nodal algorithm with the $\mathbf{R}_{diag}$ prior is competitive with its elemental counterpart in terms of both resolution and SNR. Conversion from nodal to elemental basis, as described in section 5.2.4, imparts additional smoothing to the elemental solutions. This effect is not quantified here, however the elemental solutions do have the advantage of this additional smoothing. The solutions presented in figures 5.3 and 5.4 are in the elemental basis.

It is possible to improve the signal to noise ratio while maintaining the peak signal advantage of the nodal solutions by applying one or more stages of spatial filter discussed in 5.2.7. As shown in figure 5.5 the results are substantive. Repeated applications of the smoothing filter to the $\mathbf{R}_{diag}$ solution increase the SNR at the expense of peak amplitude and resolution. One or two passes of the filter can improve the SNR by 50% for a small cost in resolution.

The 2D results validate the applicability of the *Nodal Jacobian* algorithms by showing that for the configuration tested here, the nodal algorithm produces reconstructions as good as the elemental algorithms in terms of resolution and SNR. Moreover the nodal algorithms require less memory and run faster due to the smaller linear system that must be solved. Although not important for 2D reconstructions these speed and memory improvements allow the solution of larger systems inherent to 3D applications.

5.3.2 Hyperparameter Selection

The *BestRes* method of hyperparameter selection for 2D EIT is described in chapter 4. This method suggests selecting a hyperparameter that results in a reconstruction that has maximum resolution for an impulse contrast. The method was evaluated for 3D as follows. $\lambda_{BestRes}$ was evaluated as a function of radial position at the centre plane. For the $\mathbf{R}_{diag}$ prior the curve does not have a narrow minimum (is flat) for contrasts near the centre but becomes stable with a pronounced minimum for contrasts located between 20 and 75% of the radius from the centre. The curve becomes unstable for contrasts located at 85% radial position (close to the edge). The $\mathbf{R}_{Tik}$ curve remains flat for contrasts located near the centre and is unreliable until the contrasts are at radial positions between 30 and 65% to the edge. The resolution curve is very flat for the $\mathbf{R}_{Lap}$ prior but has detectable minimums that allow selection of the hyperparameter when the radial position of the target phantom

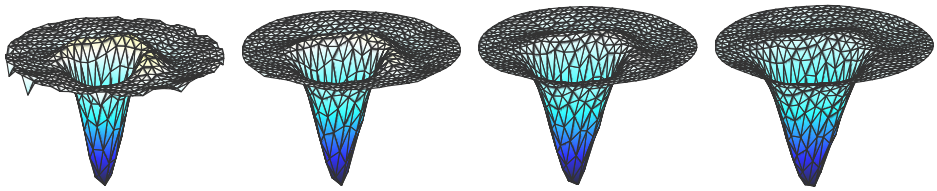

(a) $\mathbf{R}_{diag}$ *BR=.236, SNR=.332*

(b) *Filtered Once BR=.253, SNR=.444*

(c) *Filtered Twice BR=.282, SNR=.546*

(d) *Filtered 3 times BR=.318, SNR=.644*

Figure 5.5: *Spatial smoothing filter applied to nodal inverse solver algorithm with* $\mathbf{R}_{diag}$ *prior, 1024 element mesh. Reconstructions are normalized so that the vertical axis and color scales are maximized.*

is between 10% and 75%.

In chapter 4 Graham and Adler recommend using $\lambda_{BestRes}$ calculated for a contrast located at r/2 for the 2D case. This suggestion is valid for the 3D case with the added rule that the contrast be located halfway between the electrode planes. Figure 5.6 shows resolution as a function of radial position and shows the effective ranges of the *BestRes* algorithm for a given priors.

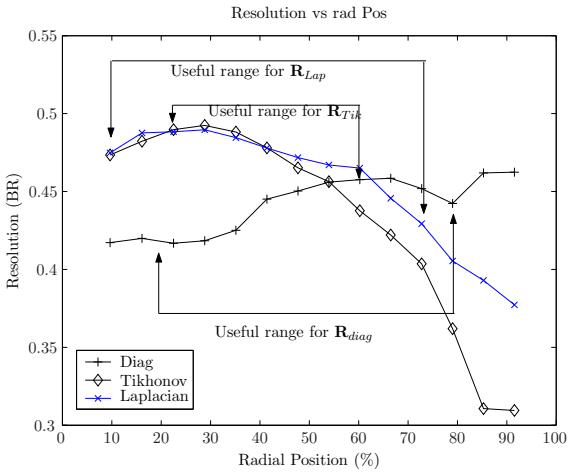

Figure 5.6: *Resolution vs Radial Position for* $\mathbf{R}_{Tik}$, $\mathbf{R}_{diag}$ *and* $\mathbf{R}_{Lap}$ *Priors*

5.3.3 3D Simulation Results

Due to the excessive memory requirements it is not possible to calculate elemental solutions of the 3D models using 32 bit Matlab. Consequently we do not evaluate the performance of the nodal 3D algorithm by comparison with its elemental counterpart. Rather we report on the performance of the nodal algorithms for 3D.

We calculated four sets of solutions, one for each prior, for each of the two data sets ($r = 0$ and $r/2$) described in section 5.2.8. These data sets were reconstructed using the FEM illustrated in figure 5.1(b) and the hybrid adjacent protocol described in section 5.2.1.

Some reconstructions from the $r/2$ data set are shown in figure 5.7. This figure shows vertical slices through a one quarter section of the reconstructed tank for 3 different vertical

positions of the impulse phantom. The leftmost column is the $\mathbf{R}_{Tik}$ prior, the centre column is the $\mathbf{R}_{diag}$, the right most is the $\mathbf{R}_{Lap}$ prior. We do not show the $\mathbf{R}_{HPF}$ solutions as they were similar to the $\mathbf{R}_{Tik}$ results.

From a qualitative point of view the three priors provide similar reconstructions in that none of them appears superior to the others in terms of a qualitative assessment of figure 5.7. Analysis of the various plots of figure 5.8 show that the $\mathbf{R}_{Tik}$ is inferior to the others in terms image energy while the $\mathbf{R}_{diag}$ prior is slightly superior in terms of resolution.

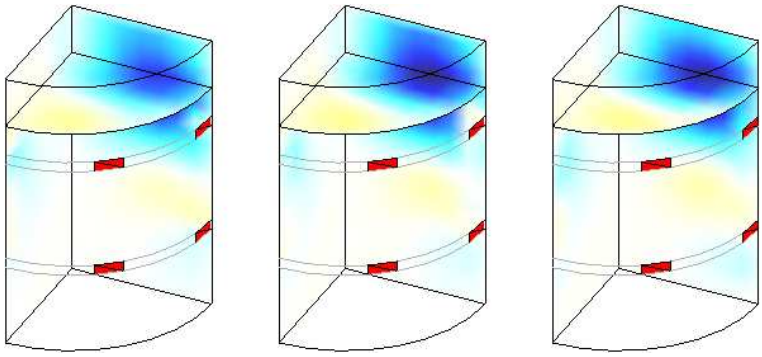

(a) *Target Height 23cm*

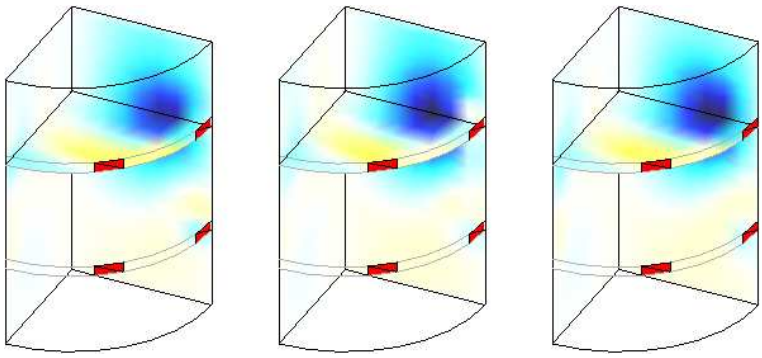

(b) *Target Height 19cm*

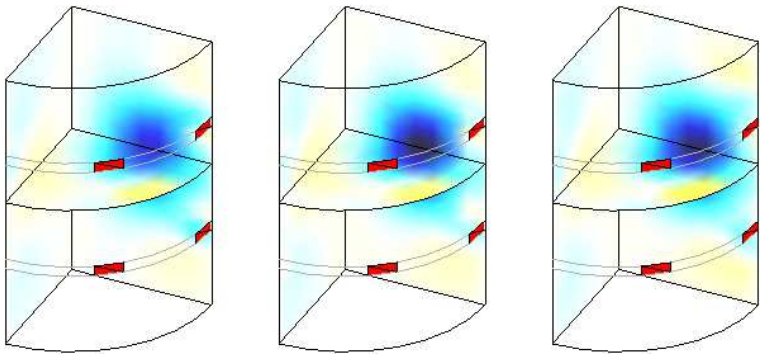

(c) *Target Height 15cm*

Figure 5.7: *Quarter section reconstructions of contrasts located at radial offset of r/2. Left column is* $\mathbf{R}_{Tik}$ *prior, centre column is* $\mathbf{R}_{diag}$ *prior, right column is* $\mathbf{R}_{Lap}$ *prior. Two electrodes per layer are shown*

Figure 5.8(a) shows the resolution for all three priors for the two sets of simulated data, r=0 and r/2. The resolution varies by 20% as a function of height. The best resolution for each prior occurs near the electrode planes with the worse resolution occurring in the

plane located halfway between the electrode planes. This is expected as resolution or its counterpart, sensitivity, decreases as position moves from current injecting or measuring electrodes. Thus resolution will be worse half way between the electrode planes. Radial position error as shown in figure 5.8(b) is lowest for contrasts at the centre of the tank and increases as contrasts move radially outward. In general however, the radial position error is small.

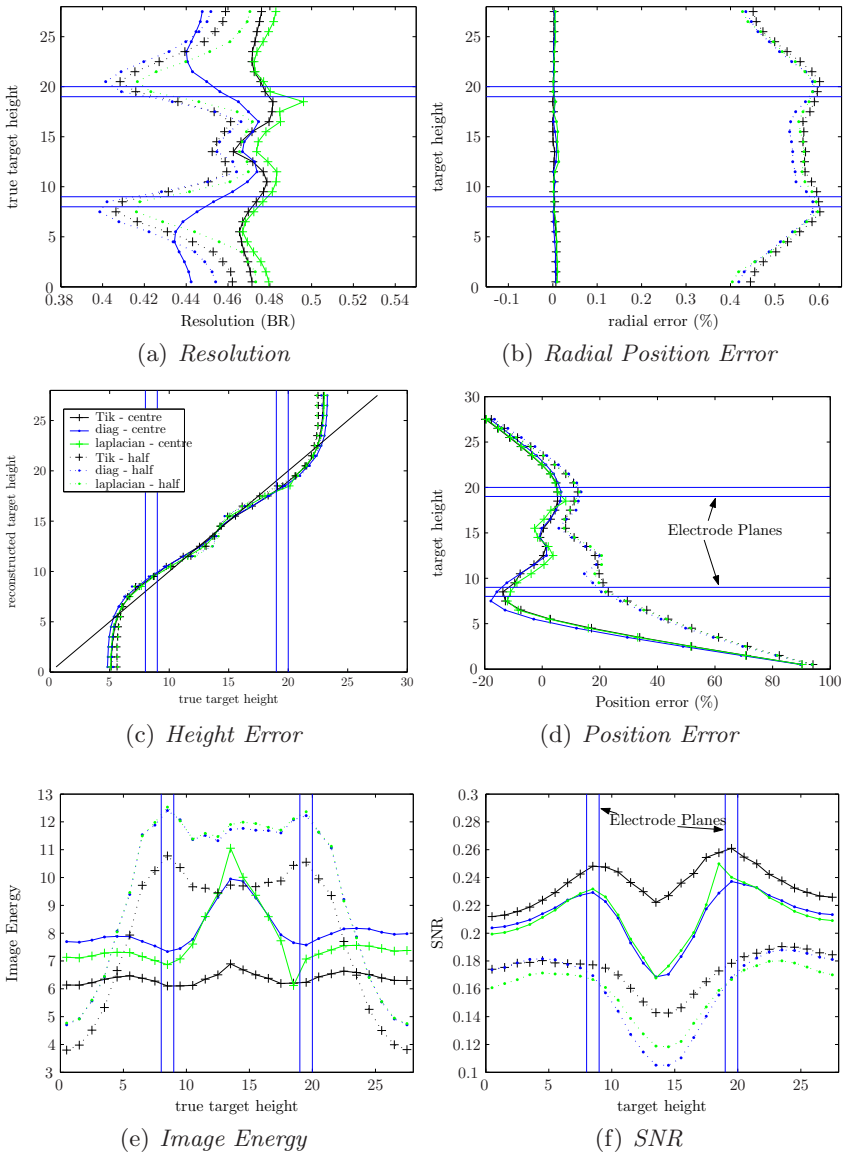

(a) *Resolution* (b) *Radial Position Error*

(c) *Height Error* (d) *Position Error*

(e) *Image Energy* (f) *SNR*

Figure 5.8: *Performance Measures for 3D Reconstructions of Two Simulated Data Sets. Legend in figure (c) applies to all figures. Electrode Planes are centered at heights of 8.5 and 19.5cm as indicated in 5.8(d) and 5.8(f)*

Height error as shown in figure 5.8(c) is common for all priors. There is a general tendency for contrasts to be reconstructed closer to the electrode planes than they actually are.

Position error is shown in figure 5.8(d) is a combination of the radial and vertical position errors and mainly indicates an asymmetry in the vertical axis. Figure 5.8(e) shows the

variability of image energy as a function of target height. The $\mathbf{R}_{diag}$ and $\mathbf{R}_{Lap}$ priors provide the largest image energy but are also the most variable with respect to target vertical position. For example targets located in one of the electrode planes result in reconstructions with four times as much energy as the same target located at the extreme ends of the tank. Figure 5.8(f) shows the signal to noise ratio of the reconstructed images.

Overall the $\mathbf{R}_{diag}$ prior gives the best results however the difference between it and the $\mathbf{R}_{Lap}$ prior is minor. No work was completed for this paper concerning the effect of electrode plane separation on reconstruction performance.

5.3.4 Human Lung Data Results

The basic analysis of sections 5.3.1 and 5.3.3 are based on impulse contrasts which are not necessarily representative of complex contrasts. In order to test the *Nodal Jacobian Inverse Solver* for complex contrasts we reconstructed some lab data of human lungs using the $\mathbf{R}_{diag}$ prior. Data were measured from a human subject using the equipment and 3D protocol of section 5.2.1. The reconstruction shown in figure 5.9 was calculated in 12s on an AMD Athlon 64 3000+ with 2GB RAM using 45 iterations of Matlab's built-in preconditioned conjugate gradient function. The image on the left of figure 5.9 shows vertical planes of the 3D volume. The images on the right of figure 5.9 are two horizontal slices of the 3D reconstruction model. The lungs are readily observed in the two horizontal slices. The vertical slice on the left shows that the vertical extent of the lungs does not extend to the vertical extremes of the 3D modeled volume. These results suggest that the *Nodal Jacobian* algorithm can be used for clinical applications.

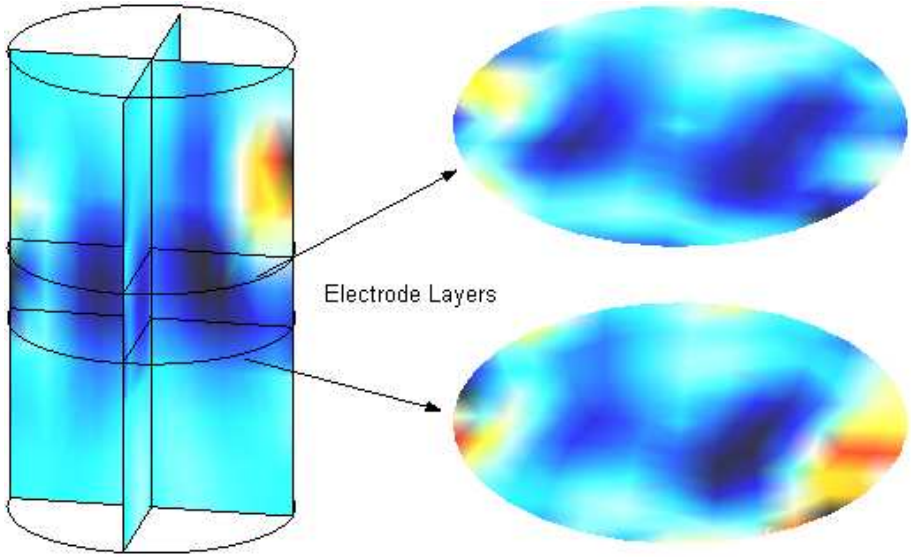

Figure 5.9: *Human Lung Data reconstructed using Nodal Jacobian Algorithm with the* $\mathbf{R}_{diag}$ *prior.*

5.4 Discussion

This paper has presented a new family of algorithms for solving the inverse problem in EIT. The main advantage of the *Nodal Jacobian* algorithm is that it reduces the size of the linear system that must be solved. This allows the reconstruction of images from 3D

models that are difficult or impossible to solve using element based algorithms. 16 electrode protocols were used in this work. Existing and future 3D EIT systems have 32, 64 or even 128 electrodes. The associated Jacobian will be large but it is possible to construct an elemental Jacobian for meshes with up to 130,000 elements with the 32 bit computers used in our lab. However the corresponding Hessian matrix will be too large to form, consequently such large models will be unsolvable using the elemental Jacobian via equation 5.6. The algorithm introduced in this paper reduces the computational requirements by a factor of up to 36 (26 for this paper's model) for dense 3D meshes and provides a promising way to solve high density 3D models with many electrodes. A secondary advantage of the nodal algorithm is the improvement in data extraction and rendering speeds which allow the display of multiple reconstructed image slices in real time.

The *Nodal Jacobian* algorithm is not an element or mesh free method, since the element based model is used to solve the forward problem and to calculate the elemental Jacobian from which the Nodal Jacobian is calculated. Future work could look at developing an algorithm to calculate a nodal Jacobian directly instead of calculating it from the elemental Jacobian.

Although the motivation for this work was to solve 3D problems, the *Nodal Jacobian Inverse Solver* algorithms produce solutions as good, in terms of resolution and SNR, as traditional algorithms for 2D configurations. 3D reconstructions from simulated data indicate that the *Nodal Jacobian Inverse Solver* with the $\mathbf{R}_{diag}$ or $\mathbf{R}_{Lap}$ prior is useful for imaging situations that have to date used an element based Jacobian with a smoothing prior. Finally, the successful reconstruction of a conductivity change image of human lungs from clinical data shows that the *Nodal Jacobian Inverse Solver* algorithm has good potential for clinical use.

Chapter 6

Electrode Placement Configurations for 3D EIT

This chapter is the text of a paper titled "Electrode Placement Configurations for 3D EIT" by Bradley GRAHAM and Andy ADLER accepted for publication in Physiological Measurement.

This paper addresses the problem of determining good electrode placement strategies for collecting 3D data from the chest given some equipment limitations and a specific set of constraints concerning electrode placement: (section 1.3 objective O3 and section 1.4.1 Contributions by Objective O3). Electrode placement for 2D reconstruction algorithms is typically confined to planar arrangements that match the 2D reconstruction geometry; yet the EIT problem is inherently 3D as currents cannot be confined to flow in the plane. Consequently 2D reconstructions are subject to artefacts generated by off plane contrasts. 3D reconstruction algorithms with multi-plane electrode arrangements have been used to more accurately reconstruct impedance distributions [90][99][115]. Compared to 2D there are many more ways to arrange and sequence electrodes when placing them in 3D. Given the variety of possible 3D electrode placement strategies, it is important to know which ones perform best in a specific application such as lung imaging.

The main contribution of this objective is the proposal of several EP configurations, followed by a rigorous evaluation of their performance, concluding with a recommendation for which of the proposed strategies is the best way to collect 3D lung data using existing adjacent drive tomography systems intended for 2D.

Abstract

This paper investigates several configurations for placing electrodes on a 3D cylindrical medium to reconstruct 3D images using 16 electrode EIT equipment intended for use with a 2D adjacent drive protocol. Seven different electrode placement configurations are compared in terms of the following figures of merit: resolution, radial and vertical position error, image energy, immunity to noise, immunity to electrode placement errors, and qualitative evaluation of image artefacts. Results show that for ideal conditions, none of the configurations considered performed significantly better than the others. However, when noise and electrode placement errors were considered the planar electrode placement configuration (two rings of vertically aligned electrodes with electrodes placed sequentially in each ring) had the overall best performance. Based on these results, we recommend planar electrode placement configuration for 3D EIT lung imaging of the thorax.

6.1 Introduction

EIT attempts to calculate a stable and accurate image of the conductivity or conductivity change within a medium from electrical measurements made on the medium boundary. Due to computational complexity, reconstructions have usually been over a 2D Finite Element Mesh (FEM). Continued improvements in computing power have permitted the recent exploration of 3D reconstructions [90][98]. Electrode placement for 2D reconstruction algorithms is confined to planar arrangements that match the 2D reconstruction geometry; yet the EIT problem is inherently 3D as currents cannot be confined to flow in the plane. Consequently 2D reconstructions are subject to artefacts generated by off plane contrasts.

3D reconstruction algorithms with multi-plane electrode arrangements have been used to more accurately reconstruct impedance distributions [90][98][113]. Dehghani *et al* in [41] investigated *excitation* patterns for applications of 3D breast imaging using 64 electrodes arranged in four layers. Performance was evaluated in terms of singular value decomposition and qualitative evaluation of reconstructed images. Polydorides and McCann [99] developed and evaluated an electrode segmentation scheme for 3D reconstructions. They examined the effects of the singular values of the Jacobian on the spatial resolution and concluded that the electrode segmentation scheme significantly improved the conditioning of the Jacobian and resulted in improved resolution.

Many EIT research groups use 16 electrode systems using adjacent stimulation and measurement, based on the original configuration of [17] and [127]. This is the case, for example, of the Goe-MF II adjacent stimulation tomography system (Viasys Healthcare, Höchberg, Germany) available in our lab. With the *adjacent* drive pattern the 16 electrodes are arranged equispaced in a single plane around the perimeter of the medium. Current is applied to an adjacent pair of electrodes and the resultant voltages between the remaining 13 adjacent pairs of electrodes is measured. The three possible measurements involving one or both of the current injecting electrode are not used. This is repeated 16 times with current injected between successive pairs of adjacent electrodes until all 16 possible pairs of adjacent electrodes have been used to apply the known current. This is shown schematically in figure 6.1. This procedure produces $16 \times 13 = 208$ voltage measurements called an EIT data *frame*. Since the electrodes are numbered 1 through 16 the adjacent pattern in 2D is obtained through a simple *sequencing* of the 16 machine leads to the 16 electrodes. This work is motivated by the desire to use such a 2D system to perform 3D EIT reconstructions.

Compared to 2D there are many more ways to arrange and sequence electrodes when placing them in 3D. Given the variety of possible 3D electrode placement strategies, it is important to know which ones perform best. However the large numbers of possibilities make this problem intractable. Consequently we choose to study a small set of possibilities guided by our intention to use the results for pulmonary imaging.

In this paper we propose and evaluate seven EP configurations in which the electrodes are arranged in two parallel planes of eight electrodes each, with electrodes equispaced around the medium. We define an EP configuration as the combination of physical placement of the electrodes and current injection pattern. Different current injection patterns are obtained through various sequencings or mappings of the 16 electrode leads to electrodes. Performance is evaluated in terms of several figures of merit as well as immunity to noise and performance in the presence of electrode placement errors. The results apply to any medium which is approximately cylindrical; however, we are specifically interested in lung imaging

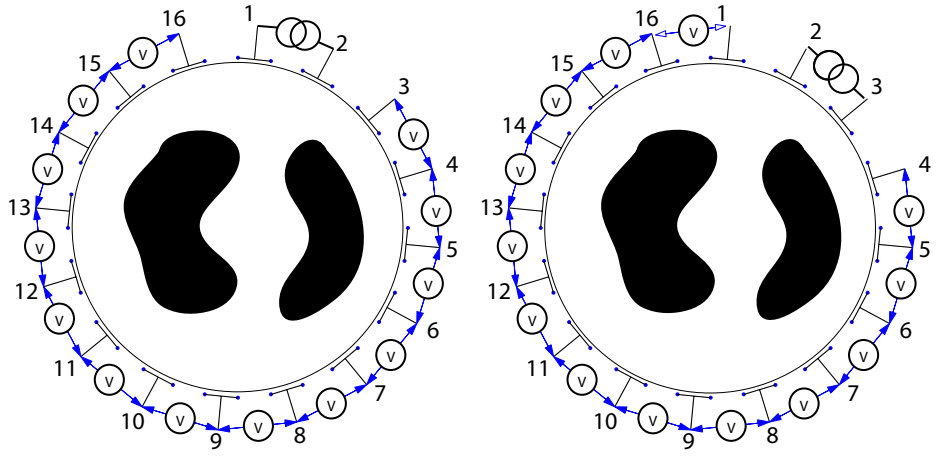

(a) *First of 16 drive pairs* (b) *Second of 16 drive pairs*

Figure 6.1: *2D Adjacent drive patterns. In figure 6.1(a) current is injected through electrode pair* $(1, 2)$ *and the resulting boundary voltage differences are measured from electrode pairs* $(3, 4), (4, 5), ..., (14, 15), (15, 16)$. *Voltages are not measured between pairs* $(16, 1), (1, 2)$, *or* $(2, 3)$. *In figure 6.1(b) the current is injected between pair* $(2, 3)$, *and the voltage differences measured between pairs* $(4, 5), (5, 6), ..., (15, 16), (16, 1)$. *Voltages are not measured between pairs* $(1, 2), (2, 3)$, *or* $(3, 4)$.

applications, in which one wants to obtain more accurate tomographic slices through the chest.

6.2 Methods

We consider EIT difference imaging, which is widely understood to improve reconstructed image stability in the presence of problems such as unknown contact impedance, inaccurate electrode positions, nonlinearity, and in the 2D case, the use of 2D approximations for 3D electrical fields [17][87]. We address the class of normalized one-step linearized reconstruction algorithms that calculate the change in a finite element conductivity distribution, $\boldsymbol{x} = \boldsymbol{\sigma}_2 - \boldsymbol{\sigma}_1$ due to a change in EIT difference signal, $\mathbf{z} = \mathbf{v}_2 - \mathbf{v}_1$ over a time interval (t_1, t_2). By convention we consider the signal at t_1 to be the *reference* frame and the signal at t_2 to be the *data* frame. Since we do not know $\boldsymbol{\sigma}_1$, $\mathbf{x}$ is interpreted as the change in conductivity with respect to the unknown initial conductivity $\mathbf{x} = \Delta\boldsymbol{\sigma} = \boldsymbol{\sigma}_2 - \boldsymbol{\sigma}_1$.

For small changes around a background conductivity the relationship between $\mathbf{x}$ and $\mathbf{z}$ may be linearized as

$$\mathbf{z} = \mathbf{H}\mathbf{x} + \mathbf{n} \tag{6.1}$$

where $\mathbf{H}$ is the Jacobian or sensitivity matrix and $\mathbf{n}$ is the measurement system noise, assumed to be uncorrelated additive white Gaussian (AWGN). Each element i, j, of $\mathbf{H}$ is calculated as $\mathrm{H}_{ij} = \frac{\partial \mathrm{z}_i}{\partial \mathrm{x}_j}\Big|_{\sigma_0}$ and relates a small change in the i^{th} difference measurement to a small change in the conductivity of j^{th} element. $\mathbf{H}$ is a function of the FEM, the current injection pattern, and the background conductivity. We use a homogenous background conductivity in which $\boldsymbol{\sigma}_0 = \mathbf{1}$ for each of the elements.

6.2.1 Image Reconstruction

In order to overcome the ill-conditioning of equation $\mathbf{H}$ we solve equation 6.1 using the following regularized inverse

$$\hat{\mathbf{x}} = (\mathbf{H^T W H} + \lambda^2 \mathbf{R})^{-1} \mathbf{H^T W z} = \mathbf{B z} \tag{6.2}$$

where $\hat{\mathbf{x}}$ is an estimate of the true change in conductivity distribution, $\mathbf{R}$ is a regularization matrix, λ is a scalar hyperparameter that controls the amount of regularization, and $\mathbf{W}$ models the system noise. Since noise is uncorrelated in the system, $\mathbf{W}$ is a diagonal matrix with $\mathbf{W}_{ii} = 1/\sigma_i^2$ where σ_i^2 is the noise variance for measurement i. $\mathbf{W}$ can also be modified to account for variable gain settings on each tomograph channel. However, for this work we assume that all measurements have equal noise variance with the result that $\mathbf{W}$ becomes a multiple of the identity matrix.

In this work we use $\mathbf{R} = diag(\mathbf{H^T H})$ which is the regularization matrix used in the NOSER algorithm of Cheney *et al* [35]. Hyperparameter selection was performed using the *BestRes* method [52] extended for 3D as described in Graham and Adler [53].

Solution of 6.2 for 3D requires solving linear systems that are too large to be solved with linear algebra systems based on 32 bit pointers (such as is available in current versions of Matlab). Graham and Adler [53] describe a *Nodal Jacobian* inverse solver algorithm that converts the element based Jacobian of equation 6.2 to a nodal based Jacobian. This algorithm reduces the size of $\mathbf{H^T W H}$ by up to a factor of 36 (the improvement factor for the model used in this work is 26.15) and allows the solution of Finite Element Models with 21000 elements and over 4000 nodes such as those used in this work[1].

6.2.2 Finite Element Models

Simulated data were generated from a dense 28 layer, 86016 element, 15805 node FEM mesh, while reconstructions were performed on a coarser 28 layer, 21504 element, 4205 node mesh. Both meshes matched the geometry of the 28cm diameter by 28cm high cylindrical tank in our lab which can be used with the Goe-MF II type tomography system. Thus each layer was 1cm thick. Electrodes were 2.8cm by 1cm in size and arranged in two parallel planes 11cm apart which can be seen in figure 6.2. The lower plane of electrodes are located in the 9^{th} layer (z=8 to z=9cm), while the upper plane of electrodes are located in the 20^{th} layer (z=19 to z=20cm). Figure 6.3 shows the dense mesh while figure 6.2 shows the coarse meshes.

6.2.2.1 Electrode Placement Configurations

Electrodes can be arranged in multiple planes or random locations, however the EP configurations proposed in this paper all consist of electrodes arranged at two layers of the mesh. The choice of 2 layers is based on the desire for a "regular" arrangement that will be easy to apply to the thorax. With 2 layers of electrodes the 16 electrode leads can be connected to the 16 tank electrodes in an arbitrary way that we call a sequence. We call the combination of electrode *arrangement* on the tank (either aligned or offset in this work) and *sequencing* an *Electrode Placement (EP) configuration*. The following 7 EP configurations are proposed and evaluated in this paper: Planar, Planar-Offset, Planar-Opposite, Zigzag, Zigzag-Offset, Zigzag-Opposite, and Square. Table 6.1 provides a mapping of the 16

[1]The work discussed in this paper was developed with the EIDORS Version 3 package using the complete electrode model [113]. Software for this work is currently being added to EIDORS Version 3 [8].

sequentially numbered electrodes, indicated in figure 6.1, to the 16 physical tank locations which are identified by letter on figures 6.2(a) and 6.2(b).

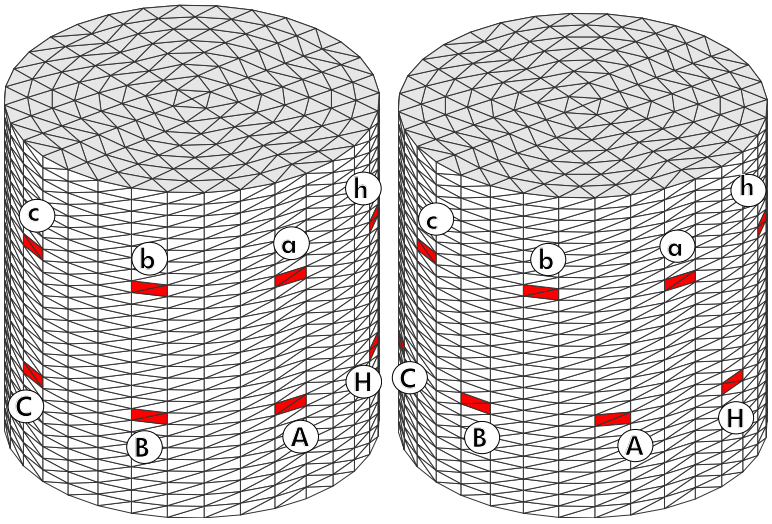

(a) *Aligned* (b) *Offset*

Figure 6.2: *Meshes used for reconstruction. Figure 6.2(a) is the* aligned *electrode arrangement. Figure 6.2(b) is the* offset *electrode arrangement. With the* offset *arrangement the lower electrode plane is rotated such that the electrodes are offset by half the inter-electrode spacing.*

For the three Planar EP configurations, measurements are mainly taken between electrodes in the same plane (intra-planar), with the exception of measurements taken between electrodes 8 & 9, and 16 & 1 which are inter-planar measurements. With the three Zigzag patterns measurements are always taken between electrodes in different planes (inter-planar). The Square EP configuration has an equal amount of data taken from inter- and intra-planar electrode pairs.

6.2.3 Evaluation Procedure

The seven EP configurations were evaluated using three simulation experiments for each configuration: vertical target movement, radial target movement, and contrast discrimination. For each of the seven EP configurations a single homogenous reference frame was simulated using the dense FEM shown in figure 6.3. The vertical target movement experiment consisted of data frames generated using a small target located halfway along the radius of the tank (r/2) that was moved through 28 vertical positions as illustrated by the vertical stack of (green) elements indicated in figure 6.3. The radial target movement experiment consisted of data frames generated using a small target located at the midplane of the figure 6.3 tank (a height of 14 cm) that was moved from the centre to the side of the mesh in 14 steps along the radius. The contrast discrimination experiment consisted of data frames generated using two small targets: a conductivity decrease located vertically at a height of 14cm, at a radial distance of r/2 at 0° (3 o'clock) and a conductivity increase located vertically at height 4cm, at a radial distance of r/2 at 180° (9 o'clock - opposite side of tank).

Subsequently, for each of the seven EP configurations, 28 reconstructions were calculated for the vertical target movement experiment and 14 reconstructions were calculated for

Aligned, fig 6.2(a)	Planar	Zigzag		Zigzag-Opposite	Square
Offset, fig 6.2(b)	Planar-Offset	Zigzag-Offset	Planar-Opposite		
1	a	a	a	a	a
2	b	B	E	e	b
3	c	b	b	b	B
4	d	C	F	f	C
5	e	c	c	c	c
6	f	D	G	g	d
7	g	d	d	d	D
8	h	E	H	h	E
9	A	e	e	D	e
10	B	F	A	H	f
11	C	f	f	C	F
12	D	G	B	G	G
13	E	g	g	B	g
14	F	H	C	F	h
15	G	h	h	A	H
16	H	A	D	E	A

Table 6.1: *Mapping of electrode number to tank location (letter) for the seven EP configurations. First column is electrode lead number, other columns are corresponding electrode position on tank as shown in 6.2.*

the radial target movement experiment under various conditions of noise and electrode placement errors. A single reconstruction was made for each of the EP configurations for the contrast discrimination experiment. Two planes of electrodes lead to a logical partitioning of the tank into three zones (top and bottom end zones, and the middle zone). It is assumed that in many cases the region of interest (ROI) will be confined to the middle zone. A good EP configuration will minimize reconstruction artefacts in the middle zone caused by contrasts in the end zones.

Reconstructions were evaluated and compared based on the following criteria:

1. *SNR and Conditioning*: The SNR of the difference signals for each configuration were compared. We define SNR $= 20\log_{10}\text{mean}(\mathbf{z})/\text{stdDev}(\mathbf{z})$. The condition numbers and singular values of each Jacobian matrix were compared: the SVD of a matrix $\mathbf{H}$ is a decomposition of the form

$$\mathbf{H} = \mathbf{U}\Sigma\mathbf{V}^T = \sum_{i=1}^{N} \mathbf{u}_i \sigma_i \mathbf{v}_i^T$$

   where $\mathbf{U} = (\mathbf{u}_1, ..., \mathbf{u}_n)$ and $\mathbf{V} = (\mathbf{v}_1, ..., \mathbf{v}_n)$ are matrices with orthonormal columns, $\mathbf{U}^T\mathbf{U} = \mathbf{V}^T\mathbf{V} = \mathbf{I}_n$, and where Σ is a diagonal matrix with non-negative diagonal elements, σ_i arranged in non-increasing order such that $\sigma_1 \geq ... \geq \sigma_n \geq 0$. The σ_i are the singular values of $\mathbf{H}$. The condition number of $\mathbf{H}$ is $cond(\mathbf{H}) = \sigma_1/\sigma_n$.

2. *Resolution* is a figure of merit (FOM) defined in terms of the 3D extension of the blur radius measure used in Adler and Guardo [4]. For 3D BR is defined as $BR = r_z/r_0 = \sqrt[3]{V_z/V_0}$ where r_0 and V_0 are the radius and volume respectively of the entire 3D medium and r_z and V_z are the radius and volume of the reconstructed contrast containing half the magnitude of the reconstructed image. BR calculates the volume fraction of the elements that contain the largest amplitude contributions to 50% of

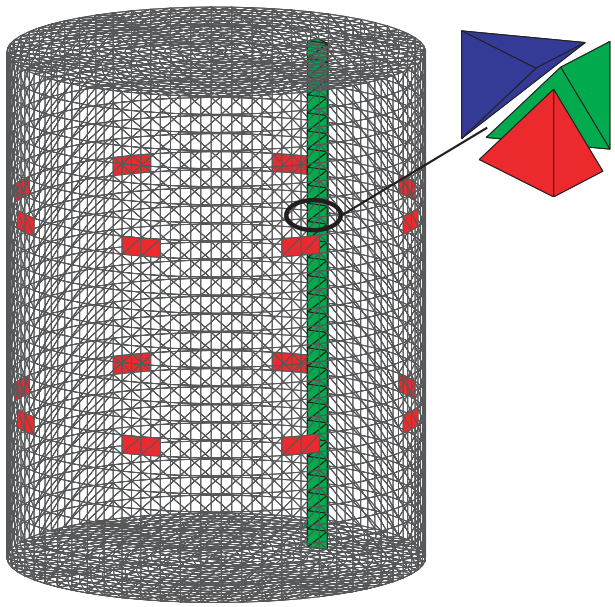

Figure 6.3: *The r/2 impulse was generated from a three tetrahedron wedge taken from each of the 28 layers of the large mesh. This produced 28 data frames per EP configuration. Lower electrode plane is at z=8 to z=9cm. Upper electrode plane is at z=19 to z=20cm.*

the total image amplitude. It is a measure of the concentration of image amplitude. The set of elements that contribute to the blur radius is called the half amplitude (HA) set [52].

3. *Radial Position Error (PE)* is a FOM defined as the proportional difference in radial position of the centre of mass of the reconstructed image HA set and the centre of mass of the generating small target. This is expressed as a percentage where a negative quantity indicates that the reconstructed image is closer to the centre of the tank than the corresponding generating impulse.

4. *Vertical PE* is a FOM defined as the proportional difference in the vertical position of the centre of mass of the reconstructed image HA set and the centre of mass of the generating small target. This is expressed as a percentage of tank height where a negative quantity indicates that the reconstructed image is closer to the central plane of the tank than the corresponding generating impulse.

5. *Image Magnitude (IM)* is a FOM that measures the magnitude of the HA set. It is defined as the sum of the volume-weighted element conductivity magnitudes where the only elements of the HA set are included: $IM = \sum_{i \in HA} ||\sigma_i|| V_i$ where V_i is the volume of the i^{th} element, σ_i is the estimated change in conductivity of the i^{th} element.

6. *Qualitative Evaluation* of reconstructed images which is primarily a subjective evaluation of image artefacts. We expect a qualitatively good image to appear as a small spherical blur corresponding to the generating target. A poor image could exhibit artefacts such as non-spherical extent, features that exist in the wrong locations or that do not correspond to the generating target, and protrusions from the main image.

7. *Immunity to Noise.* Using the vertical target movement data, an additional six sets

of reconstructions were calculated for each of the seven EP configurations in which AWG noise was added in six steps from 0.1% to 0.6% of the difference signal, **z**. The ability of each EP configuration to reconstruct images in the presence of this noise was then compared in terms of the FOMs described earlier.

8. *Immunity to systematic electrode placement errors.* Two techniques were used to evaluate electrode position errors.

   (a) In the first technique reconstructions were performed with a systematic electrode position error in which data collected with one of the EP configurations were reconstructed using the same electrode sequence but with the lower plane of electrodes rotated by half the inter-electrode distance (*Offset-Error*). Thus in this first case data generated with the Planar EP configuration were reconstructed using the Planar-Offset EP configuration. This is shown in figure 6.4 direction A. In the second case data generated with the Planar-Offset EP configuration were reconstructed using the Planar EP configuration. This is shown in figure 6.4 direction B. In the case of pulmonary imaging this error simulates a twisting of the thorax.

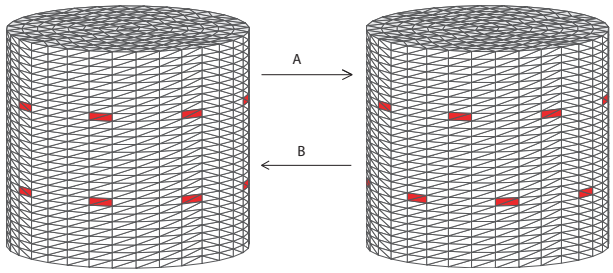

Figure 6.4: *Offset Error. Direction A: Data observed with aligned arrangement were reconstructed with offset arrangement. Direction B: Data observed with offset arrangement were reconstructed with aligned arrangement*

   (b) In the second technique an *Electrode Plane Separation Error* was evaluated as follows: For each EP configuration 9 sets of data were simulated with the distance between the electrode planes increasing from the correct separation of 11cm, to a layer separation of 20cm. Each set was comprised of homogenous reference frame and 28 data frames generated with a small target as in section 6.2.3. Each of 9 data sets per EP configuration was then reconstructed on the same mesh geometry but always with the electrodes at the interplanar distance of 11cm. This simulates a systematic electrode placement error in which the reconstruction model does not match the actual electrode placement for 8 of the 9 simulated data sets. In the case of pulmonary imaging this error simulates an inaccurate application of the electrodes.

6.3 Results

In this section, we compare each EP strategy against each figure of merit, in order to differentiate amongst the performance of the various EP configurations.

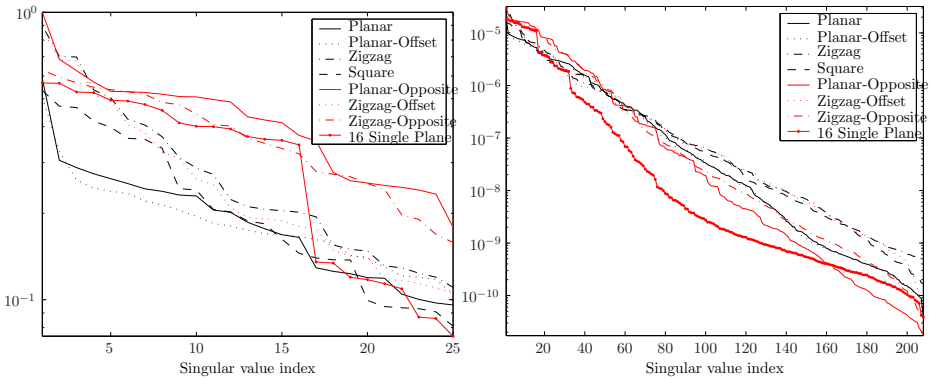

(a) *First 25 Singular Values, normalized* (b) *All Singular Values, non-normalized*

Figure 6.5: *Singular Values of* $\mathbf{H}$ *for the 7 EP Configurations*

6.3.1 Evaluation of Maximum Performance Experiments.

The initial evaluation looked at the best case performance of the EP configurations in that noise was not added to the vertical or radial movement data described in section 6.2.3 nor were electrode errors present. The following observations were made concerning this best case set of reconstructions:

6.3.1.1 SNR and Conditioning

The normalized SNR is listed in table 6.2. The Planar and Planar-Offset EP configurations have similar and significantly larger SNRs than the other configurations. This indicates that these two configurations should be more robust to noise than the others. This is observed in section 6.3.2 - Evaluation of Noise Effects. The condition numbers are also listed in table 6.2 but are less informative. Although there is a difference of a factor of 10 between the Square and Planar-Opposite configurations this is not significant in that all of the condition numbers are in excess of 10^{22}.

EP Configuration	SNR (normalized)	SNR (db)	cond($\mathbf{H}^T\mathbf{H}$) ($\times 10^{23}$)
Planar	1.0000	-3.9568	0.7826
Planar-Offset	0.9709	-4.0849	3.8234
Planar-Opposite	0.3852	-8.0997	0.4019
Zigzag	0.2965	-9.2365	2.0639
Zigzag-Offset	0.2702	-9.6406	2.6358
ZigZag-Opposite	0.2924	-9.2971	0.6721
Square	0.3907	-8.0380	5.8860

Table 6.2: *Comparison of EP Configurations in terms of SNR and Jacobian Condition Number.*

The singular values of each Jacobian were calculated for each EP configuration and are plotted in figure 6.5. Also included are the singular values for the 2D EP configuration in which the 16 electrodes are arranged in a single plane. The long term trend of the singular values is not significantly different between the various EP configurations with the exception of the 2D configuration. Figure 6.5(a) shows the first 25 singular values, in this

case normalized to the first and largest singular value. Although there are variations in the singular values the long term trends are similar and we conclude in this case that the singular values are not useful discriminators of the seven EP configurations. Picard plots of all EP configurations are similar; the Picard condition is satisfied for each EP configuration, however the singular values never cross the Picard coefficients. Thus it is not possible to use Picard plots to determine the number of singular values above the noise.

6.3.1.2 Resolution

Figure 6.6(a) shows Resolution as a function of reconstructed height. The resolution of all EP configurations varies as a function of the height of the contrast. The resolution curves of figure 6.6(a) show that the range of variation in resolution amongst the EP configurations, in the end regions is large compared to the range of variation in the middle section. The Planar EP configuration has the best resolution in the end zones, the opposite configurations have the worse performance in the middle zone; however, the differences are small and it appears that Resolution is not a strong discriminator of EP configurations. In general the

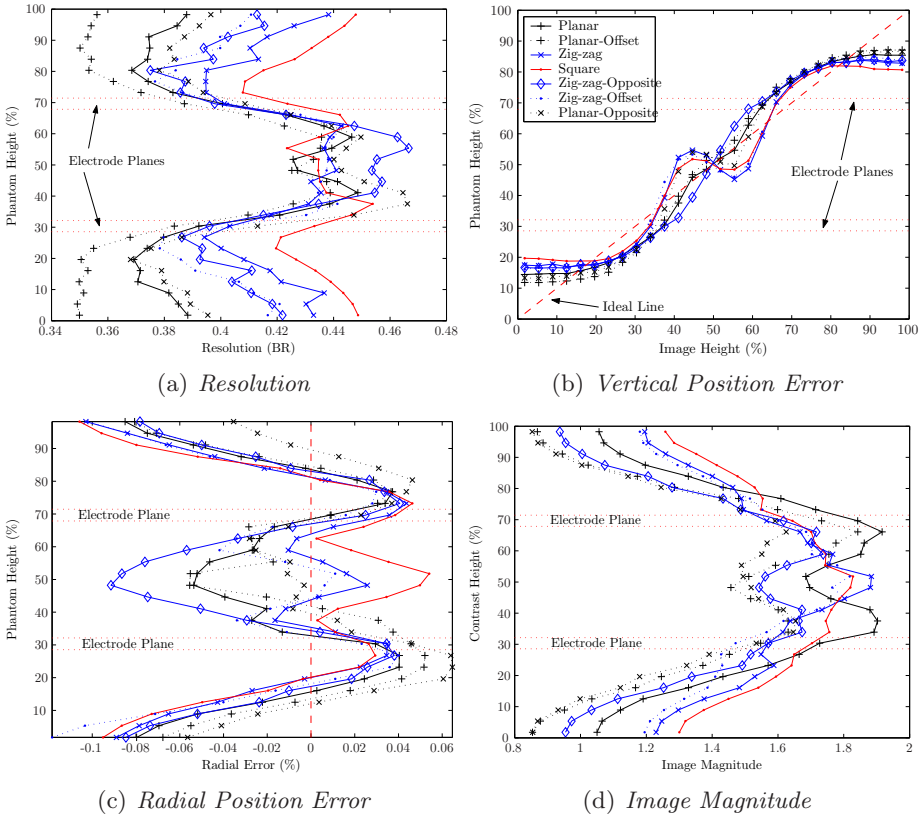

(a) *Resolution* (b) *Vertical Position Error*

(c) *Radial Position Error* (d) *Image Magnitude*

Figure 6.6: *Performance measures for 7 EP Stategies vs Contrast Height for noise free reconstructions of a contrast moving through 28 vertical positions at $r/2$. Legend in figure 6.6(b) is for all plots.*

resolution of all EP configurations varies as a function of distance from electrode plane so none of the EP configurations have a stable resolution vs contrast height function; however, the relative magnitude of the instability is small.

6.3.1.3 Vertical PE

Figure 6.6(b) shows Vertical PE vs reconstructed height. For perfect reconstructions the curves would be straight lines. All of the EP configurations suffer from a vertical range compression in the end sections. The Zigzag, Zigzag-Offset, Square, and Planar-Opposite EP configurations have a large non-linearity in the central region of the graph. This is undesirable as it causes the reconstruction to be unstable; a small change in the vertical position of the generating contrast can cause a large change in the vertical position of the reconstruction. A good EP configuration should have a near linear response in the middle zone. Vertical PE is an useful discriminator of EP configurations.

6.3.1.4 Radial PE

Figure 6.6(c) shows that for all of the EP configurations Radial PE is largest at the ends, improves as the generating contrast approaches the electrode planes, and decays as the contrast moves between the electrode planes. The various Radial PE curves behave differently in the inter-planar region; however, the difference is mainly one of sign with the magnitudes being small. Radial PE is not a strong discriminator of EP configurations.

6.3.1.5 Image Magnitude

Figure 6.6(d) is a plot of Image Magnitude vs phantom height showing that Image Magnitude increases as the phantom location moves from the ends of the tank toward the electrode planes. Although the behaviour of the various EP configurations in the middle section is different for each configuration it is difficult to say what behaviour is desired and therefore which EP configuration is preferable. Overall, Image Magnitude is not a strong discriminator of EP configurations.

6.3.1.6 Radial Performance

Figure 6.7 shows various performance measures for reconstructions from the radial movement data. As expected, the resolution plot of figure 6.7(a) shows a large variability in resolution as a function of radial position for all the EP configurations. The Zigzag and Zigzag-Opposite EP configurations have the most stable response albeit at a lower average resolution while the Planar-offset and Zigzag-offset configurations show the most variability in resolution yet have the best peak resolution (at the 80% radius). Figure 6.7(b) shows a large variability in vertical position error for all EP configurations with the exception of the Planar-Opposite, and Planar-Offset configurations which are relatively stable. Image radial position error, figure 6.7(c), is similar for all configurations thus is a poor discriminator for the set of configurations being evaluated. Finally, figure 6.7(d), indicates that image magnitude of the Planar and Planar-offset EP configurations are marginally more stable than the other configurations; however, image magnitude does not appear to be a strong discriminator between configurations.

6.3.1.7 Qualitative Evaluation

Figure 6.8 shows several reconstructions for contrasts located at the centre plane of the tank. The Planar, Planar-Opposite, Planar-Offset and Square EP configurations, figure 6.8(a), produce circular reconstructions that are all circular/spherical. The Zigzag figure 6.8(b) and Zigzag-Opposite figure 6.8(c) configurations produce images that are vertically elongated while the reconstruction of the Zigzag-Offset EP configuration figure 6.8(d) is

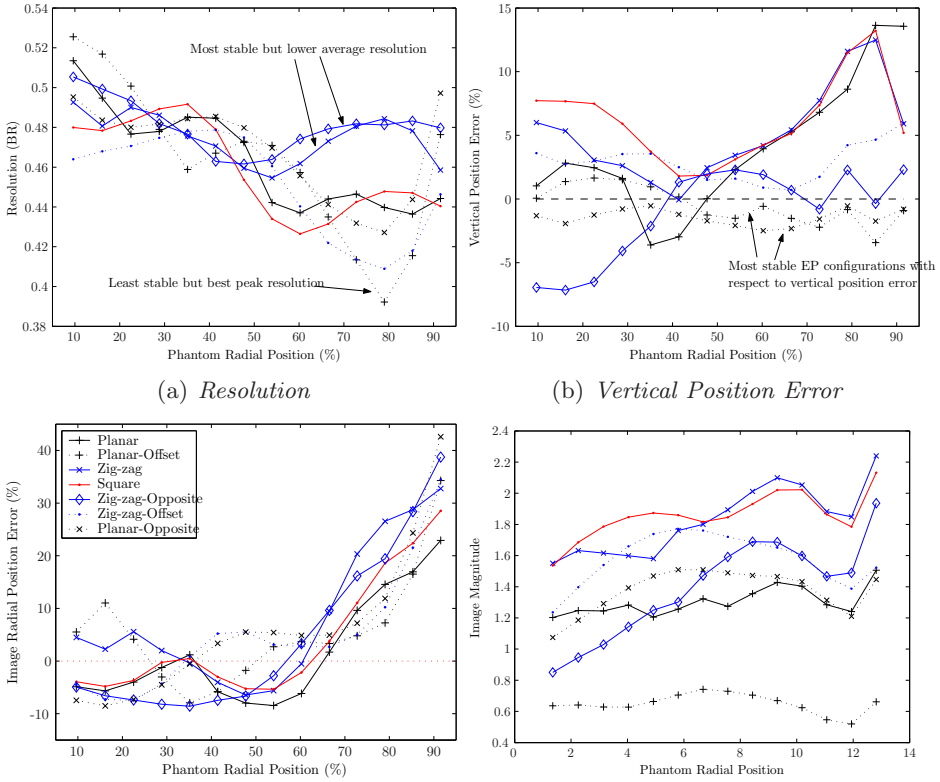

(a) *Resolution* (b) *Vertical Position Error*

(c) *Image Radial Position Error* (d) *Image Magnitude*

Figure 6.7: *Performance measures for 7 EP Stategies vs Contrast Radial Position for noise free reconstructions of a contrast moving through 14 radial positions at the vertical centre of the tank. Legend in figure 6.7(c) is for all plots.*

banana shaped. Additionally the Zigzag-Opposite configuration figure 6.8(c) has "finger" like artefacts extending from the image to the electrode planes. The best performance for targets located in the end sections are obtained with the Zigzag and Square EP configurations while reconstructions using the Planar, Planar-Offset (similar) and Planar-Opposite EP configurations produce images with large artefacts. As mentioned in section 6.2.3, in some applications the region of interest (ROI) may be confined to the middle zone in which case it may be preferable to use an EP configuration that works very well in the ROI despite producing artefacts for contrasts located in the end zones.

6.3.1.8 Contrast Discrimination

Figure 6.9 show vertical slices through the mesh for 3D reconstructions of the contrast discrimination experiment data. All of the 3D EP configurations are able to localize the two contrasts as shown in figures 6.9(a) to 6.9(c). The Square and Zigzag-Offset EP configurations, figure 6.9(a), provide the best qualitative performance in terms of section 6.2.3(6); however, the Planar, Planar-offset and Zigzag EP configurations, which are similar in appearance to each other, figure 6.9(b), are almost as good. Of the 3D EP configurations, the Planar-opposite is clearly the worst performer with the lower phantom being quite blurred, figure 6.9(c). Figure 6.9(d) shows that the 2D electrode arrangement cannot accurately locate the contrasts: the centrally located phantom appears as a conductivity decrease image with a large vertical extent and a crescent shape centred in the mesh while the phantom

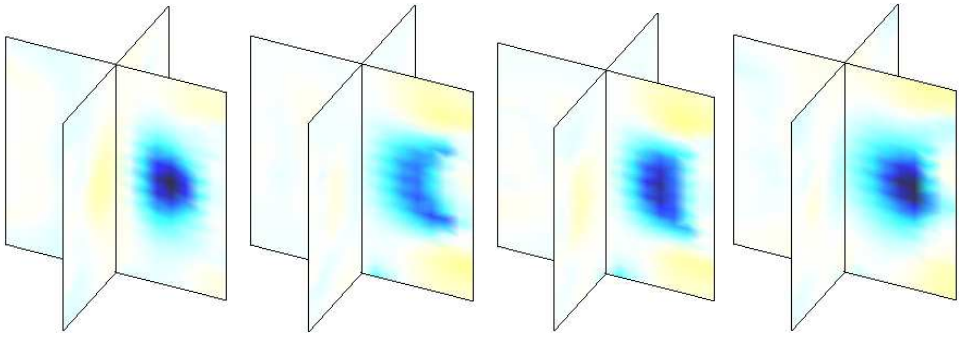

(a) *Planar-Offset, Planar, Planar-Opposite, and Square are similar.* (b) *Zigzag-Offset* (c) *Zigzag* (d) *Zigzag-Opposite*

Figure 6.8: *Baseline reconstructions for the $r/2$ small target at midplane ($z = 14cm$).*

located at 4cm height is also reconstructed as a large crescent shape centered through the middle of the mesh.

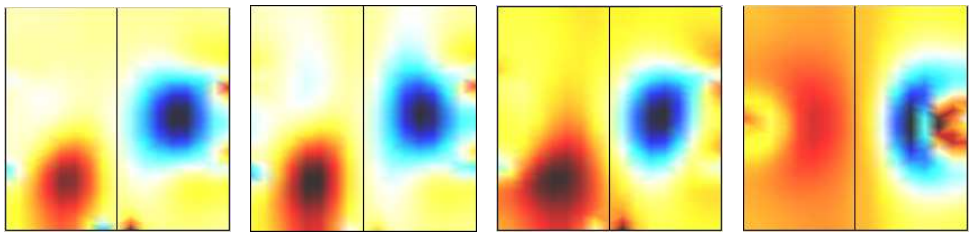

(a) *Zigzag-Offset, Square* (b) *Planar, Zigzag, Planar-Offset* (c) *Planar-Oposite* (d) *2D Adjacent*

Figure 6.9: *2D slices taken vertically through the centre of the reconstruction mesh showing 3D localization of contrasts.*

6.3.2 Evaluation of Noise Effects

In addition to the baseline reconstructions discussed above, an additional six sets of reconstructions were calculated for each of the seven EP configurations in which AWG noise was added in six steps from 0.1% to 0.6%. The noise was added to the data simulated as described in section 6.2.3. The Zigzag and Zigzag-Offset EP configurations could not produce useful reconstructions for noise levels above 0.2% while the Square EP configuration did not work with noise above 0.3%. Although useful reconstructions could be calculated using the two Opposite EP configurations with up to 0.6% noise, their Resolution and PE performance degraded rapidly. The Planar and Planar-Offset EP configurations were very robust to noise; resolution and PE degraded slowly and good images were reconstructed with noise in excess of 0.6%.

6.3.3 Electrode Position Errors - Offset Error

All of the EP configurations suffered degradation in resolution due to the offset error. The Zigzag-Offset pattern has the largest loss of resolution; however, the Planar-Opposite EP

configuration gave the worse overall performance: a conductivity decrease resulted in images of a conductivity increase. The Planar, Planar-Offset, and Zigzag EP configurations were able to reconstruct a circular/spherical image without introducing image shape artefacts. In all cases the centre of mass of the reconstructions were rotated in the axial plane by about 20°. Since EIT is expected to be used for functional imaging as opposed to anatomical imaging, the rotation position error may not be important as long as the magnitude of the conductivity change is accurate.

6.3.4 Electrode Position Errors - Electrode Plane Separation Error

Radial PE, Vertical PE and Resolution are not significantly affected by electrode plane separation errors for any of the EP configurations. All of the performance measures degraded smoothly. This can be seen with some representative plots in figures 6.10(a) to 6.10(c). Qualitatively, all configurations produced vertically elongated images with the Square and the two Opposite EP configurations being most affected, Zigzag and Zigzag-Offset configurations less so, and the Planar and Planar-Offset EP configurations the least. For contrasts located in the end zones, the Zigzag, Zigzag-Offset, and Square configurations

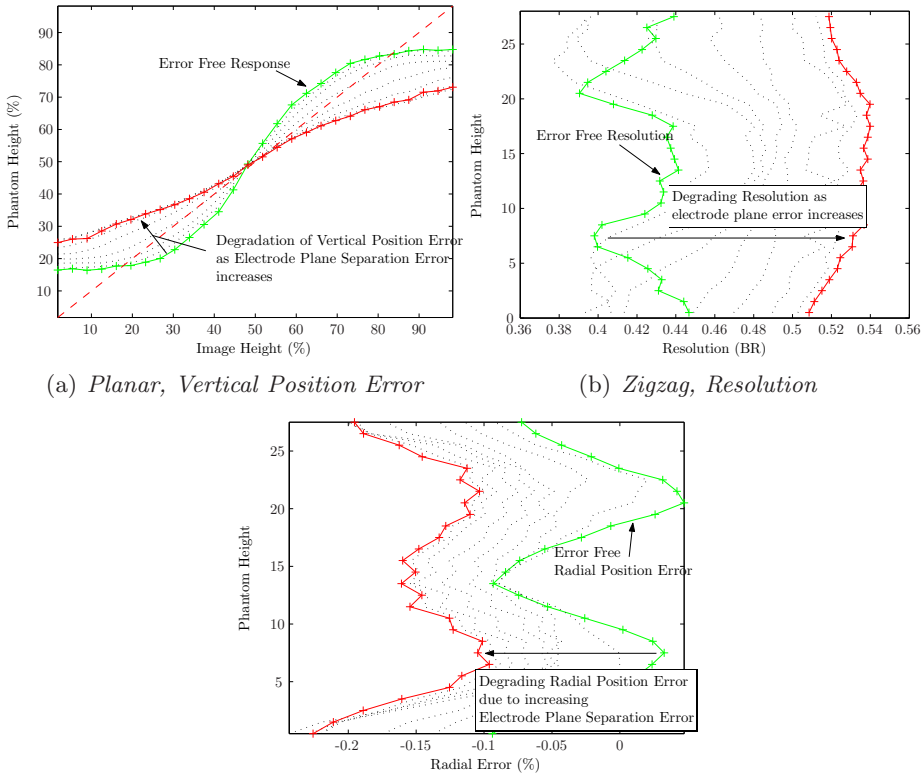

(a) *Planar, Vertical Position Error*

(b) *Zigzag, Resolution*

(c) *Planar-Opposite, Radial Position Error*

Figure 6.10: *Degradation of selected performance measures for selected configurations due to electrode plane separation error. The Error Free curves represent no electrode plane separation error. The dotted curves represent increasing electrode plane separation to a maximum of 10 cm error represented by the red solid line.*

show a swirling artefact while the Opposite EP configurations show an extensive vertical lengthening of the reconstructed contrast. The Planar and Planar-Offset EP configurations

also showed an increased Radial PE due to the contrast being *pushed* toward the tank centre for phantoms located in the end sections. This effect was less noticeable with the Planar EP configuration. Both the Planar and Planar-Offset EP configurations show little degradation due to electrode plane separation errors of up 20% (6cm on the 28cm tall tank). The Planar-Offset is slightly more robust than the Planar EP configuration in this regard.

6.3.5 2D Limitations

In addition to the seven 3D EP configurations additional reconstructions were performed using the same 3D meshes but with the 16 electrodes arranged in a single plane at a height of 14cm. The plots of figure 6.11 were generated similarly to those of section 6.2.3: 28 data frames from the $r/2$ phantom moving through 28 vertical locations. Figure 6.11(c) validates the obvious insight that vertical position cannot be resolved using a single plane of electrodes. Regardless of actual phantom height, the 2D arrangement always reconstructs an image that is located in the plane of the electrodes. As the small target moves farther away from the electrode plane the resolution, figure 6.11(a), and the image magnitude, figure 6.11(d), both decrease while the the radial error, figure 6.11(b), increases.

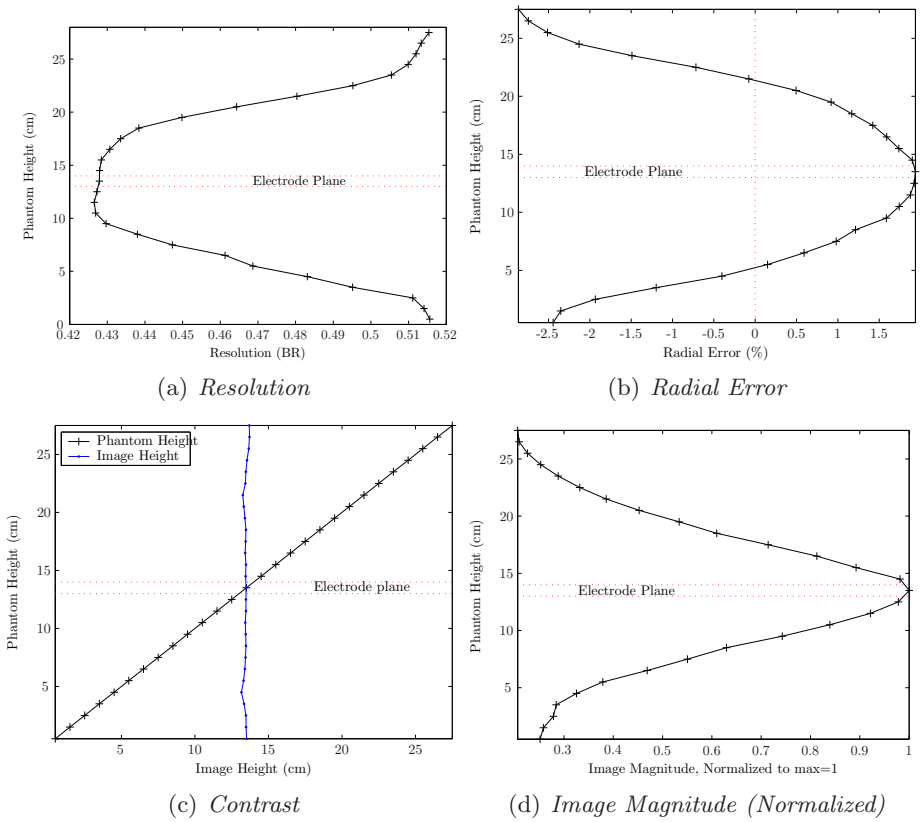

(a) *Resolution* (b) *Radial Error*

(c) *Contrast* (d) *Image Magnitude (Normalized)*

Figure 6.11: *Performance measures vs Phantom Height for noise free reconstructions with single layer of 16 electrodes for the small target moving through 28 vertical positions at* $r/2$.

6.3.6 Summary

A qualitative summary of the significant discriminators is presented in table 6.3. Five of the configurations show poor performance in one or more of the discriminators while the

Planar and Planar-offset configurations, which have similar performance, do not.

Figure of Merit Reference	Res Fig 6.6(a)	VPE Fig 6.6(b)	Qual Sect 6.3.1.7	Noise Sect 6.3.2	Offset Err Sect 6.3.3	Sep Err Sect 6.3.4	VPE (Radial) Fig 6.7(b)
Planar			+	+	+	+	
Planar-Offset			+	+	+	+	+
Planar-Opposite	-		+		- -	- -	+
Zigzag		- -	-	- -	+	-	
Zigzag-Offset		- -	- -	- -	-	-	
ZigZag-Opposite	-		-			- -	
Square		- -	+	-		- -	

Table 6.3: *Comparison Summary of EP Configurations - in the ROI.*

6.4 Conclusion

This paper has investigated the performance of a small set of 3D electrode placement configurations under the constraints of a 16 electrode adjacent drive system intended for 2D applications arranged in two planes. We make the following observations:

1. Opposite EP configurations are highly susceptible to corruption by noise and are not recommended.

2. The Zigzag EP configuration performs poorly in the presence of noise.

3. The Zigzag-Offset EP configuration is susceptible to Offset error.

4. The Square configuration suffers from the instability in VPE, has poor noise performance, and shows electrode to contrast "finger" artefacts.

5. The Planar and Planar-Offset EP configurations are most robust to noise and systematic electrode placement errors and have performance as good or better than the other configurations for targets in the ROI.

6. The Planar EP configuration provides the largest image energy for contrasts located in the centre section, and is the most robust to noise (slightly better than Planar-offset).

The current data suggest that no one EP configuration offers a worthwhile improvement over the others under ideal conditions. This observation that there is little difference in the noise free cases may be attributable to the fact that the various patterns are linearly dependent; thus given noise free data, it is possible to calculate any set from any other. Only when noise and electrode placement errors are considered does the choice of EP configuration become important. The difficulty of accurately placing a large number of electrodes on a person may be the largest discriminating factor amongst EP configurations intended for clinical use. Moreover electrode placement errors are exacerbated and change throughout the imaging session due to subject movement. This leads one to prefer an EP configuration that is robust to electrode placement errors and is easy to apply on a patient.

The addition of more electrodes to a 2D planar arrangement will allow higher resolution 2D reconstructions, however it is not known how the addition of more electrode layers will improve the vertical resolution on 3D reconstructions. Future work is required to analyze such configurations in order to understand how such electrode arrangements may be generalized.

In summary, the goal of this paper is to evaluate some electrode placement strategies for 16 electrode adjacent drive EIT systems in order perform 3D image reconstructions. Based on the results, and considering the value of easy of electrode placement, we recommend the

Planar electrode placement. Thus, 16 electrodes should be placed in two rings of vertically aligned electrodes with electrodes placed sequentially in each ring.

Chapter 7

Total Variation Regularization in EIT

This chapter is the text, with minor revisions, of a paper titled "Total Variation Regularization in EIT" by Andrea BORSIC, Bradley GRAHAM, Andy ADLER, and Bill LIONHEART to be submitted to IEEE Transactions on Biological Medical Imaging.

This paper addresses the problem of determining the viability of a non-blurring regularization method for 3D lung imaging (section 1.3 objective O4 and section 1.4.1 Contributions by Objective O4) by evaluating the PD-IPM algorithm for TV regularization of EIT reconstructions and comparing the algorithm's performance to the computationally simpler quadratic regularization. TV regularised reconstructions are considerably more expensive to calculate than quadratic reconstructions, however the TV PD-IMP algorithm is able to compute 2D non-smooth reconstructions in the presence of moderate noise, and is therefore of practical use in certain applications. The main contribution of this objective was the improvement in convergence of the PD-IPM algorithm and the evaluation of the algorithm's performance in 2D and 3D applications.

This is a collaborative work. The development of the PD-IPM algorithm, its explanation and implementation are the original work of Andrea Borsic and can be found in [23]. The analysis of the algorithm's performance, including the improvement in convergence, the simplification of the β decay schedule as well as the design and execution of the algorithm's performance evaluation and subsequent conclusions are the original contribution of this thesis.

Abstract

The paper presents a Primal-Dual Interior Point Method (PD-IPM) for efficiently solving the Total Variation (TV) regularized inverse conductivity problem for EIT. The TV functional leads to the formulation of the inverse problem as a minimization of a non-differentiable function which cannot be efficiently solved with traditional minimization techniques such as Steepest Descent and Newton Methods. The ability of the TV functional to preserve discontinuities in reconstructed profiles promotes the development of new algorithms, such as PD-IPM, that are able to efficiently solve the non-differentiable minimization.

This paper initially outlines of the discontinuity preserving properties of the TV functional followed by the development of the PD-IPM algorithm. The paper concludes with an evaluation of the PD-IPM algorithm and a comparison of its performance to that of

the traditional quadratic regularized inverse. Results show that TV regularized images for EIT have an improved ability to reconstruct images with sharp discontinuities for low noise data. Noise performance was similar for TV and quadratic inverse.

Keywords: regularization, EIT, TV Electrical Impedance Tomography, Total Variation, Primal Dual Interior Point Methods

7.1 Introduction

Electrical Impedance Tomography (EIT) uses surface electrodes to make measurements from which an image of the conductivity distribution within some medium is calculated. The inverse conductivity problem is ill-posed [26]; consequently regularization techniques have been adopted in order to stabilize the inversion. Most common regularization methods impose (explicitly or implicitly) a penalty on non-smooth regions in a reconstructed image. Such methods confer stability to the reconstruction process, but limit the capability of describing sharp variations in the sought parameter.

One technique to permit image regularization without imposing smoothing is the Total Variation (TV) formulation of regularization. The Total Variation functional is assuming an important role in the regularization of inverse problems belonging to many disciplines, thanks to its ability to preserve discontinuities in the reconstructed profiles. Application of non-smooth reconstruction techniques is important for medical and process imaging applications of EIT, as they involve discontinuous profiles. Qualitative and quantitative benefits can be expected in these fields.

We outline the properties of the TV functional in the next section, to motivate its use as a regularization penalty term and to understand the numerical difficulties associated with it. The use of the TV functional leads in fact to the formulation of the inverse problem as a minimization of a non–differentiable function. Application of traditional minimization techniques (Steepest Descent Method, Newton Method) has proven to be inefficient [44][23]. Recent developments in non-smooth optimization (Primal Dual–Interior Point Methods) have brought the means of dealing with the minimization problem efficiently. The performance of this algorithm with respect to traditional smooth algorithms is the subject of this paper.

7.2 Methods

This paper introduces the PD-IPM algorithm as follows. In the Methods section we describe the traditional family of EIT reconstruction algorithms used in our research, describe the TV functional and its PD-IPM implementation for EIT, and describe the evaluation procedure. In the Results section we describe the effectiveness of the TV functional compared to the quadratic regularized inverse. In the Discussion section we consider some additional observations of this work.

7.2.1 Static Image Reconstruction

We consider static EIT imaging where the goal of the algorithm is to recover the absolute conductivity of the medium under analysis. The technique requires a forward operator F

on the conductivity vector, $\boldsymbol{\sigma}$, which calculates V = $F(\boldsymbol{\sigma})$, the simulated voltages at the boundary. The reconstruction is commonly stabilized using regularization; the inversion is stated as:

$$\hat{\boldsymbol{\sigma}}_{rec} = \arg\min_{\sigma} \frac{1}{2} \|F(\boldsymbol{\sigma}) - \mathbf{V}_{\text{meas}}\|^2 + \alpha G(\boldsymbol{\sigma}) \tag{7.1}$$

where $\mathbf{V}_{\text{meas}}$ is the vector of the measured voltages $F(\boldsymbol{\sigma})$ the forward model prediction, $G(\boldsymbol{\sigma})$ the regularization functional, α is a hyperparameter controlling the level of applied regularization and the norm $||\cdot||$ is the 2-norm.

7.2.2 Quadratic Solution

The functional $G(\boldsymbol{\sigma})$ is often assumed to be of the form:

$$G(\boldsymbol{\sigma}) = \|\mathbf{L}(\boldsymbol{\sigma} - \boldsymbol{\sigma}^*)\|^2 \tag{7.2}$$

where $\mathbf{L}$ is an appropriate regularization matrix and $\boldsymbol{\sigma}^*$ a prior estimate of the conductivity distribution. In the literature there are several choices for the matrix $\mathbf{L}$, for example the identity matrix [126], a positive diagonal matrix [35], approximations of first and second order differential operators [71], and the inverse of a Gaussian matrix [4]. Algorithms of this class fall into general framework expressed by equations 7.1 and 7.2, that is:

$$\hat{\boldsymbol{\sigma}}_{rec} = \arg\min_{\boldsymbol{\sigma}} \frac{1}{2} \|F(\boldsymbol{\sigma}) - \mathbf{V}_{\text{meas}}\|^2 + \alpha \|\mathbf{L}(\boldsymbol{\sigma} - \boldsymbol{\sigma}^*)\|^2 \tag{7.3}$$

The framework expressed by equation 7.3 can be called quadratic regularization since the 2-norm is used. A norm guarantees that the functional is always positive, as a penalty term should be, and more important, the resulting functional is differentiable, leading to an easier solution of the minimization problem. Quadratic regularization, because of its simple differentiability, has been the common framework for solving several inverse problems, and particularly for EIT [126][35][71][26][78][24].

The optimization problem 7.3 can be solved by replacing $F(\sigma)$ with its linear approximation for a small change about an initial conductivity distribution $\boldsymbol{\sigma}_0$

$$F(\boldsymbol{\sigma}) \approx F(\boldsymbol{\sigma}_0) + \mathbf{J}(\boldsymbol{\sigma} - \boldsymbol{\sigma}_0) \tag{7.4}$$

where $\mathbf{J}$ is the Jacobian matrix of $F(\boldsymbol{\sigma})$ calculated at the initial conductivity estimate $\boldsymbol{\sigma}_0$. The function to be minimized, equation 7.1, with regularizing penalty term, equation 7.2, becomes a quadratic function when F is replaced by its linear approximation, equation 7.4. Defining $\delta\boldsymbol{\sigma} = \boldsymbol{\sigma} - \boldsymbol{\sigma}_0$ and $\delta\mathbf{V} = F(\boldsymbol{\sigma}_0) - \mathbf{V}_{\text{meas}}$, the solution to the linearized regularization problem is given by

$$\delta\boldsymbol{\sigma} = (\mathbf{J}^T\mathbf{J} + \alpha\mathbf{L}^T\mathbf{L})^{-1}\mathbf{J}^T\delta\mathbf{V} + \alpha\mathbf{L}^T\mathbf{L}(\boldsymbol{\sigma} - \boldsymbol{\sigma}_{ref}) \tag{7.5}$$

Equation 7.5 is solved iteratively with $\boldsymbol{\sigma}_{i+1} = \boldsymbol{\sigma}_i + \delta\boldsymbol{\sigma}$. The drawback is that, regardless of the choice of $\mathbf{L}$, the technique cannot reconstruct step changes, smooth solutions are favoured.

7.2.3 Total Variation Functional

There are situations in almost every field of application of EIT where the imaged conductivity has discontinuities. In the medical field an example is that of the inter organ boundaries

where each organ has its own electrical properties. In archaeology a buried wall will give rise to a sudden step in conductivity, and in process tomography a multiphasic fluid will give rise to discontinuities at each phase interface. It is therefore important to be able to reconstruct these situations correctly, even though such conductivities are difficult to deal with using traditional algorithms. Several approaches have been investigated in order to overcome these limitations. Often they can be considered a way to introduce prior information. An example is anisotropic regularization [78][24] where the structure of the expected sudden changes is assumed to be roughly known. The smoothness constraints are relaxed therefore in the direction normal to the discontinuities. In this way the algorithm better describes rapid variations in the object, however prior structural information needs to be known in order to adopt such methods.

Many regularization matrices are discrete representations of differential operators and are used in conjunction with the 2–norm. A different approach is represented by the choice of the total variation functional, which is still a differential operator but leads to a ℓ^1 regularization. The total variation (TV) of a conductivity image is defined as:

$$TV(\sigma) = \int_{\Omega} |\nabla \sigma| d\Omega \tag{7.6}$$

where Ω is the region to be imaged.

The TV functional was first employed by Rudin, Osher, and Fatemi [102] for regularizing the restoration of noisy images. The technique is particularly effective for recovering "blocky" images, and has become well known to the image restoration community [31]. The effectiveness of the method in recovering discontinuous images can be understood by examining the following one dimensional situation. Suppose that the two points A and B

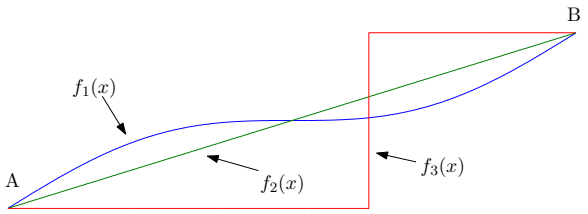

Figure 7.1: *Two points A and B can be connected by several paths. All of them have the same TV.*

of figure 7.1 are connected by a path. Three possible functions $f(x)$ connecting them are shown. As the functions are monotonically increasing, the TV of each function is:

$$TV(f) = \int_{A}^{B} f'(x)\, dx = f(B) - f(A) \tag{7.7}$$

which is the same value for each function. TV treats f_1, f_2 and f_3 in the same way and when used as a penalty term in a Tikhonov regularized inverse problem, will not bias the result towards a smooth solution. On the other hand, the ℓ^2 norm assumes different values for f_1,f_2 and f_3. When used as a penalty term the ℓ^2 norm will bias the solution towards smoother functions, for which the ℓ^2 norm assumes smaller values. In the cited example f_3 is inadmissible as a quadratic solution since its ℓ^2 norm is infinity. With the use of TV as

a regularization penalty term a much broader class of functions are therefore allowed to be the solution of the inverse problem, including functions with discontinuities. Another way to understand the differences with other techniques is to consider the discretized version of equation 7.6. Suppose that the conductivity is described by piecewise constant elements, the TV of the 2D image can be expressed as the sum of the TV of each of the k edges, with each edge weighted by its length:

$$TV(\sigma) = \sum_k l_k \left| \boldsymbol{\sigma}_{m(k)} - \boldsymbol{\sigma}_{n(k)} \right| \tag{7.8}$$

where l_k is the length of the k^{th} edge in the mesh, $m(k)$ and $n(k)$ are the indices of the two elements on opposite sides of the k^{th} edge, and the index k ranges over all the edges. Equation 7.8 can be expressed in terms of matrices as:

$$TV(\boldsymbol{\sigma}) = \sum_k |\mathbf{L}_k \boldsymbol{\sigma}| \tag{7.9}$$

where $\mathbf{L}$ is a sparse matrix, with one row per each edge in the mesh. Every row $\mathbf{L}_k$ has two non zero elements in the columns $m(k)$ and $n(k)$: $\mathbf{L}_k = [0, ..., 0, l_k, 0, ..., 0, -l_k, 0...0]$. TV regularization is therefore of the ℓ^1 kind: it is a sum of absolute values, in this case a sum of vector lengths. The absolute value guarantees the positivity of the penalty function but unfortunately results in non–differentiability in the points where $\boldsymbol{\sigma}_{m(k)} = \boldsymbol{\sigma}_{n(k)}$. The numerical problem thus needs to be addressed properly. However, the important gain is that the ℓ^1 regularization does not penalize discontinuities.

7.2.3.1 Solving TV - Early Approaches.

Two different approaches were proposed for application of TV to EIT, the first by Dobson and Santosa [44] and the second by Somersalo *et al* [109] and Kolehmainen [85]. Dobson and Santosa replace the absolute value function in the neighbourhood of zero by a polynomial to obtain continuously differentiable function upon which steepest descent is then used to perform the minimization. Their approach is suitable for the linearized problem but suffers from poor numerical efficiency. Somersalo and Kolehmainen successfully applied Markov Chain Monte Carlo (MCMC) methods to solve the TV regularized inverse problem. The advantage in applying MCMC methods over deterministic methods is that they do not suffer from the numerical problems involved with non-differentiability of the TV functional; they do not require *ad hoc* techniques. Probabilistic methods, such as MCMC, offer central estimates and error bars by sampling the posterior probability density of the sought parameters (therefore differentiability is not required). The sampling process involves a substantial computational effort, often the inverse problem is linearized in order to speed up the sampling. What is required is an efficient method for deterministic Tikhonov style regularization, to calculate a non-linear TV regularized inversion in a short time.

Examination of the literature shows that a variety of deterministic numerical methods have been used for the regularization of image de-noising and restoration problems with the TV functional (a good review is offered by Vogel in [117]). The numerical efficiency and stability are the main issues to be addressed. Use of *ad hoc* techniques is common, given the poor performance of traditional algorithms. Most of the deterministic methods draw from ongoing research in optimization, as TV minimization belongs to the important classes of problems known as "Minimization of sum of norms" [11][13][39] and "Linear ℓ^1 problems" [19][125].

Recent developments in operations research [13] have provided new classes of methods to deal efficiently with the problems of minimising the sum of absolute values. Chan, Golub and Mulet [30] have drawn from these advances and investigated the problem of restoring images with Primal Dual-Interior Point Methods (PD-IPM). The formulation of the image restoration problem is very similar to the EIT reconstruction problem, and results can be easily exploited. In the next section we summarize some results from Andersen, Christiansen, Conn and Overton [13] that are at the base of the method proposed by Chan [30] in image restoration applications, and of the method we propose for EIT.

7.2.4 Duality Theory for the Minimization of Sums of Norms Problem

The minimization of the term $TV(\boldsymbol{\sigma}) = \sum_k |\mathbf{L}_k\boldsymbol{\sigma}|$, can be thought to be a Minimization of Sum of Norms problem (MSN) as $\sum_k |\mathbf{L}_k\boldsymbol{\sigma}| = \sum_k \|\mathbf{L}_k\boldsymbol{\sigma}\|$, and in this case important results for MSN problems can be applied. The most general way of expressing the MSN problem is

$$\min_{\mathbf{y}} \sum_{i=1}^{n} \|A_i\mathbf{y} - \mathbf{c}_i\| \tag{7.10}$$

with $\mathbf{y} \in \mathbb{R}^m; \mathbf{c}_i \in \mathbb{R}^d$ and $A_i \in \mathbb{R}^{d\times m}$, which is equivalent to

$$(P) \quad \min_{\mathbf{y}} \left\{ \sum_{i=1}^{n} \|\mathbf{z}_i\| : A_i\mathbf{y} + \mathbf{z}_i = \mathbf{c}_i, \quad i = 1, \ldots, n \right\} \tag{7.11}$$

with $\mathbf{z}_i \in \mathbb{R}^d$. We call equation 7.11 the primal problem, and we label it (P). An equivalent problem to (P), which is called dual, and which is a maximization problem, can be obtained in the following way

$$\begin{aligned}
\min_{\mathbf{y}:A_i\mathbf{y}+\mathbf{z}_i=\mathbf{c}_i} \sum_{i=1}^{n} \|\mathbf{z}_i\| &= \min_{\mathbf{y}:A_i\mathbf{y}+\mathbf{z}_i=\mathbf{c}_i} \quad \max_{\mathbf{x}_i:\|\mathbf{x}_i\|\le 1} \sum_{i=1}^{n} \mathbf{x}_i^T\mathbf{z}_i \\
&= \max_{\mathbf{x}_i:\|\mathbf{x}_i\|\le 1} \quad \min_{\mathbf{y}:A_i\mathbf{y}+\mathbf{z}_i=\mathbf{c}_i} \sum_{i=1}^{n} \mathbf{x}_i^T\mathbf{z}_i \\
&= \max_{\mathbf{x}_i:\|\mathbf{x}_i\|\le 1} \quad \min_{\mathbf{y}\in\mathbb{R}^m} \left(\sum_{i=1}^{n} \mathbf{c}_i^T\mathbf{x}_i - \mathbf{y}^T \sum_{i=1}^{n} A_i^T\mathbf{x}_i \right) \\
&= \max_{\mathbf{x}_i} \left\{ \sum_{i=1}^{n} \mathbf{c}_i^T\mathbf{x}_i : \|\mathbf{x}_i\| \le 1; \sum_{i=1}^{n} A_i^T\mathbf{x}_i = 0 \right\}
\end{aligned} \tag{7.12}$$

where the first equality follows from Cauchy–Schwartz, the second from min–max theory [13] [101], the third trivially, and the fourth because if $\sum_{i=1}^{n} A_i^T\mathbf{x}_i$ is not zero, the minimised value would be $-\infty$. The dual problem of (P) is therefore

$$(D) \quad \max_{\mathbf{x}_i} \left\{ \sum_{i=1}^{n} \mathbf{c}_i^T\mathbf{x}_i : \|\mathbf{x}_i\| \le 1; \sum_{i=1}^{n} A_i^T\mathbf{x}_i = 0, \quad i = 1, \ldots, n \right\} \tag{7.13}$$

and the variables $\mathbf{y}$ are called primal variables and the variables $\mathbf{x}_i \in \mathbb{R}^d$ dual variables. The problems (P) and (D) are therefore equivalent. The concept of duality and the relation

between primal and dual optimal points can be formalised defining the primal feasible region as

$$\mathcal{Y} = \left\{ (\mathbf{y}, \mathbf{z}) \in \mathbb{R}^m \times \mathbb{R}^{dn} : A\mathbf{y} + \mathbf{z} = \mathbf{c} \right\} \tag{7.14}$$

and the dual feasible region as

$$\mathcal{X} = \left\{ \mathbf{x} \in \mathbb{R}^{dn} : A^T\mathbf{x} = 0; \|\mathbf{x}_i\| \leq 1, \quad i = 1, \ldots, n \right\} \tag{7.15}$$

where $\mathbf{x}$ is obtained by stacking the vectors $\mathbf{x}_i$. Andersen *et al* [13] have shown that for feasible points $(\mathbf{y}, \mathbf{z}) \in \mathcal{Y}$, $\mathbf{x} \in \mathcal{X}$

$$\sum_{i=1}^{n} \|\mathbf{z}_i\| - \sum_{i=1}^{n} \mathbf{c}_i^T \mathbf{x}_i > 0 \tag{7.16}$$

and that for optimal points $(\mathbf{y}^*, \mathbf{z}^*) \in \mathcal{Y}$, $\mathbf{x}^* \in \mathcal{X}$

$$\sum_{i=1}^{n} \|\mathbf{z}_i^*\| - \sum_{i=1}^{n} \mathbf{c}_i^T \mathbf{x}_i^* = 0 \tag{7.17}$$

In words: for feasible points the term $\sum_{i=1}^{n} \|\mathbf{z}_i\|$ is an upper bound to $\sum_{i=1}^{n} \mathbf{c}_i^T \mathbf{x}_i$ and vice-versa. The difference $\sum_{i=1}^{n} \|\mathbf{z}_i\| - \sum_{i=1}^{n} \mathbf{c}_i^T \mathbf{x}_i = \sum_{i=1}^{n} (\|\mathbf{z}_i\| - \mathbf{x}_i^T \mathbf{z}_i)$ is called the *primal–dual gap*; it is positive except at an optimal point where it vanishes. The primal–dual gap can be zero if and only if, for each $i = 1, \ldots, n$, either $\|\mathbf{z}_i\|$ is zero or $\mathbf{x}_i = \mathbf{z}_i / \|\mathbf{z}_i\|$. This can be expressed conveniently in a form called *complementary condition*

$$\mathbf{z}_i - \|\mathbf{z}_i\| \mathbf{x}_i = 0, \quad i = 1, \ldots, n \tag{7.18}$$

The complementary condition encapsulates therefore the optimality of both (P) and (D). An important class of algorithms called Primal Dual Interior Point Methods (PD–IPM) is based on the observation that equation 7.18 with the feasibility conditions equation 7.14 and equation 7.15 captures completely the optimality of both problems. The framework for a PD–IPM algorithm for MSN problem works by enforcing the three following conditions (primal feasibility, dual feasibility, complementary)

$$A\mathbf{y} + \mathbf{z} = \mathbf{c} \tag{7.19a}$$

$$A^T\mathbf{x} = 0 \tag{7.19b}$$

$$\mathbf{z}_i - \|\mathbf{z}_i\| \mathbf{x}_i = 0 \tag{7.19c}$$

The Newton Method cannot be applied in a straightforward manner to equation 7.19 as the complementary condition is not differentiable for $\|\mathbf{z}_i\| = 0$. Andersen *et al* [13] suggest replacing it with the so called *centering condition*

$$\mathbf{z}_i - (\|\mathbf{z}_i\|^2 + \beta^2)^{\frac{1}{2}} \mathbf{x}_i = 0, \quad i = 1, \ldots, n \tag{7.20}$$

where β is a small positive scalar parameter. Even if at first sight the centring condition is very similar to the smooth approximations that are generally used in the first attempts in

using total variation as a regularization functional [2][118][45][32], where $TV(\boldsymbol{\sigma})$ is approximated with $\sum_k \sqrt{\|\mathbf{L}_k\boldsymbol{\sigma}\|^2+\beta}$, it has different implications in this context. Particularly, it was shown in [12] that the centering condition is the complementary condition of the following pair of smooth optimization problems

$$\begin{aligned}(P_\beta)\quad & \min\left\{\sum_{i=1}^{n}(\|\mathbf{z}_i\|^2+\beta^2)^{\frac{1}{2}} : (\mathbf{y},\mathbf{z})\in\mathcal{Y}\right\}\\ (D_\beta)\quad & \min\left\{\mathbf{c}^T\mathbf{x}+\beta\sum_{i=1}^{n}(1-\|\mathbf{x}_i\|^2)^{\frac{1}{2}} : \mathbf{x}\in\mathcal{X}\right\}\end{aligned} \tag{7.21}$$

The problem P_β and D_β are a primal dual pair. Specifically, D_β has the solution $(y(\beta), z(\beta))$ and P_β has the solution $x(\beta)$, all satisfying equations 7.19a, 7.19b, and 7.20.

Introducing the perturbation β in the complementary condition for the original pair of problems is therefore equivalent to smoothing the norms in (P) and introducing a cost into (D). Particularly the cost function $\sum_{i=1}^{n}(1-\|\mathbf{x}_i\|^2)^{\frac{1}{2}}$ can be understood to keep the dual solution away from its boundary ($\|\mathbf{x}_i\| = 1$), from which the name of centring condition for equation 7.20, and of interior point method for the algorithm. The concept of keeping iterates away from the boundary of feasible regions originates from interior point methods for linear programming (LP) [124]. In LP optimal points are known to lie on vertices of the feasible set; traditional algorithms, such as the simplex method, exploited this by working on the frontier of the feasible region and examining vertices to find the solution. This approach changed in the mid 80s with Karmarkar's [80] introduction of interior point methods, which work by following a smoother path inside the feasible region called a *central path* (identified by a centering condition), and possibly making larger steps at each iteration. In MSN the central path is defined by the solutions $(y(\beta), z(\beta), x(\beta))$ of P_β, D_β for $\beta > 0,\ \beta \to 0$. Using these results Andersen *et al* realised an efficient PD–IPM algorithm that works maintaining feasibility conditions, equations 7.19a, 7.19b and applies the centering condition, equation 7.20, with a centering parameter β which is reduced during iterations, following the central path to the optimal point.

In the next Section we describe the application of the PD-IPM framework to TV regularized linear inverse problems.

7.2.5 Duality for Tikhonov Regularized Inverse Problems

In inverse problems, with *linear* forward operators, the discretized TV regularized inverse problem, can be formulated as

$$(P)\quad \min_{\mathbf{x}}\frac{1}{2}\|\mathbf{A}\mathbf{x}-\mathbf{b}\|^2+\alpha\sum_k|\mathbf{L}_k\mathbf{x}| \tag{7.22}$$

where $\mathbf{L}$, as in 7.9, is a discretization of the gradient operator. We will label it as the primal problem (P). The dual problem, can be derived noting, as for the MSN problem, that

$$|\mathbf{L}_k\mathbf{x}| = ||\mathbf{L}_k\mathbf{x}|| = \max_{\mathbf{y}:\|\mathbf{y}\|\le\mathbf{1}} y\,\mathbf{L}_k\mathbf{x} \tag{7.23}$$

By applying 7.23 to (P), the dual problem (D) is obtained as follows [23]

$$(D)\quad \max_{\mathbf{y}:\|\mathbf{y}_i\|\le 1}\min_{\mathbf{x}}\frac{1}{2}\|\mathbf{A}\mathbf{x}-\mathbf{b}\|^2+\alpha\mathbf{y}^T\mathbf{L}\mathbf{x} \tag{7.24}$$

The optimization problem

$$\min_{\mathbf{x}} \frac{1}{2} \|\mathbf{A}\mathbf{x} - \mathbf{b}\|^2 + \alpha \mathbf{y}^T \mathbf{L}\mathbf{x} \tag{7.25}$$

has an optimal point defined by the first order conditions

$$\mathbf{A}^T (\mathbf{A}\mathbf{x} - \mathbf{b}) + \alpha \mathbf{L}^T \mathbf{x} = \mathbf{0} \tag{7.26}$$

the dual problem can be written therefore as

$$(D) \qquad \max_{\substack{\mathbf{y} : \|\mathbf{y}_i\| \leq 1 \\ \mathbf{A}^T (\mathbf{A}\mathbf{x} - \mathbf{b}) + \alpha \mathbf{L}^T \mathbf{x} = \mathbf{0}}} \frac{1}{2} \|\mathbf{A}\mathbf{x} - \mathbf{b}\|^2 + \alpha \mathbf{y}^T \mathbf{L}\mathbf{x} \tag{7.27}$$

The primal–dual gap for (P) and (D) is therefore:

$$\begin{aligned} \frac{1}{2}\|\mathbf{A}\mathbf{x} - \mathbf{b}\|^2 + \alpha \sum_k |\mathbf{L}_k \mathbf{x}| - \frac{1}{2}\|\mathbf{A}\mathbf{x} - \mathbf{b}\|^2 - \alpha \mathbf{y}^T \mathbf{L}\mathbf{x} = \\ \alpha \left(\sum_k |\mathbf{L}_k \mathbf{x}| - \mathbf{y}^T \mathbf{L}\mathbf{x} \right) \end{aligned} \tag{7.28}$$

The complementary condition, which nulls the primal–dual gap, for 7.22 and 7.27 is therefore:

$$\sum_k |\mathbf{L}_k \mathbf{x}| - \mathbf{y}^T \mathbf{L}\mathbf{x} = \mathbf{0} \tag{7.29}$$

which with the dual feasibility $\|\mathbf{y}_i\| \leq 1$ is equivalent to requiring that

$$\mathbf{L}_i \mathbf{x} - \mathbf{y}_i \|\mathbf{L}_i \mathbf{x}\| = 0 \quad i = 1, \ldots, n \tag{7.30}$$

The PD-IPM framework for the TV regularized inverse problem can thus be written as

$$\|\mathbf{y}_i\| \leq 1 \quad i = 1, \ldots, n \tag{7.31}$$

$$\mathbf{A}^T (\mathbf{A}\mathbf{x} - \mathbf{b}) + \alpha \mathbf{L}^T \mathbf{x} = 0 \tag{7.32}$$

$$\mathbf{L}_i \mathbf{x} - \mathbf{y}_i \|\mathbf{L}_i \mathbf{x}\| = 0 \quad i = 1, \ldots, n \tag{7.33}$$

It is not possible to apply the Newton method directly to equations 7.31,7.32,7.33 as equation 7.33 is not differentiable for $\mathbf{L}_i \mathbf{x} = 0$. A centering condition has to be applied [13][23], obtaining a smooth pair of optimization problems (P_β) and (D_β) and a central path parameterised by β. This is done by replacing $\mathbf{L}_i \mathbf{x}$ by $(\|\mathbf{L}_i \mathbf{x}\|^2 + \beta)^{\frac{1}{2}}$ in 7.33.

7.2.6 PD-IPM for EIT

The PD-IPM algorithm described in section 7.2.5 was developed by Chan *et al* [30] for inverse problems with *linear* forward operators. We next describe a numerical implementation of the PD-IPM algorithm, based on [23], to calculate the non-linear solution to

$$\boldsymbol{\sigma}_{rec} = \arg\min_{\boldsymbol{\sigma}} \frac{1}{2} \|F(\boldsymbol{\sigma}) - \mathbf{V}_{\text{meas}}\|^2 + \alpha TV(\boldsymbol{\sigma}) \tag{7.34}$$

With a similar notation as used in Section 7.2.1. This is recognized as equation 7.1 with $G(\boldsymbol{\sigma}) = TV(\boldsymbol{\sigma})$. The system of *non-linear* equations that defines the PD-IPM method for 7.34 can be written as

$$\begin{array}{c} \|\mathbf{y}_i\| \leq 1 \\ \mathbf{J}^T\left(F(\boldsymbol{\sigma}) - \mathbf{V}_{\text{meas}}\right) + \alpha \mathbf{L}^T \boldsymbol{\sigma} = \mathbf{0} \\ \mathbf{L}\boldsymbol{\sigma} - \mathbf{E}\mathbf{y} = \mathbf{0} \end{array} \tag{7.35}$$

with $\mathbf{E}$ a diagonal matrix defined by $\mathbf{E} = \text{diag}\left(\sqrt{\|\mathbf{L}_i\boldsymbol{\sigma}\|^2 + \beta}\right)$ and $\mathbf{J}$ the Jacobian of the forward operator $F(\boldsymbol{\sigma})$. Newton's method can be applied to solve 7.35 obtaining the following system for the updates $\delta\boldsymbol{\sigma}$ and $\delta\mathbf{y}$ of the primal and dual variables

$$\begin{bmatrix} \mathbf{J}^T\mathbf{J} & \alpha\mathbf{L}^T \\ \mathbf{K}\mathbf{L} & -\mathbf{E} \end{bmatrix} \begin{bmatrix} \delta\boldsymbol{\sigma} \\ \delta\mathbf{y} \end{bmatrix} = - \begin{bmatrix} \mathbf{J}^T\left(F(\boldsymbol{\sigma}) - \mathbf{V}_{\text{meas}}\right) + \alpha\mathbf{L}^T\mathbf{y} \\ \mathbf{L}\boldsymbol{\sigma} - \mathbf{E}\mathbf{y} \end{bmatrix} \tag{7.36}$$

with

$$\mathbf{K} = \text{diag}\left(1 - \frac{\mathbf{y}_i\mathbf{L}_i\boldsymbol{\sigma}}{\mathbf{E}(i,i)}\right) \tag{7.37}$$

equation 7.36 can be solved as follows

$$\left[\mathbf{J}^T\mathbf{J} + \alpha\mathbf{L}^{\mathrm{T}}\mathbf{E}^{-1}h\mathbf{L}\right]\delta\boldsymbol{\sigma} = -\left[\mathbf{J}^{\mathbf{T}}\left(F(\boldsymbol{\sigma}) - \mathbf{V}_{\text{meas}}\right) + \alpha\mathbf{L}^{\mathrm{T}}\mathbf{E}^{-1}\mathbf{L}\boldsymbol{\sigma}\right] \tag{7.38}$$

$$\delta\mathbf{y} = -\mathbf{y} + \mathbf{E}^{-1}\mathbf{L}\sigma + \mathbf{E}\mathbf{K}\mathbf{L}\delta\boldsymbol{\sigma} \tag{7.39}$$

Equations 7.38 and 7.39 can therefore be applied iteratively to solve the non-linear inversion 7.34. The iterative procedure must be initialized which is done by setting $\mathbf{y_0} = \mathbf{0}$. Thus in the first iteration 7.38 is solved as

$$\delta\boldsymbol{\sigma} = (\mathbf{J}^T\mathbf{J} + \alpha\mathbf{L}^T\mathbf{L})^{-1}(\mathbf{J}^T(F(\boldsymbol{\sigma}) - \mathbf{V}_{\text{meas}}) \tag{7.40}$$

and $\delta\mathbf{y} = \mathbf{E}^{-1}\mathbf{L}\boldsymbol{\sigma} + \mathbf{E}\mathbf{K}\mathbf{L}\delta\boldsymbol{\sigma}$. This is recognizable as the first step of the 2–norm regularized inverse of equation 7.3. Some care must be taken on the dual variable update, to maintain dual feasibility. A traditional line search procedure with feasibility checks is not suitable as the dual update direction is not guaranteed to be an ascent direction for the modified dual objective function (D_β).

The simplest way to compute the update is called the *scaling rule* [13] which is defined to work as follows

$$\mathbf{y}^{(k+1)} = \varphi^*\left(\mathbf{y}^{(k)} + \delta\mathbf{y}^{(k)}\right) \tag{7.41}$$

where φ^* is a scalar value such that

$$\varphi^* = \sup\left\{\varphi : \varphi\left\|\mathbf{y}_i{}^{(k)} + \delta\mathbf{y}_i{}^{(k)}\right\| \leq 1, \quad i = 1, \ldots, n\right\} \tag{7.42}$$

An alternative way is to calculate the exact step length to the boundary, applying what is called the *step length rule* [13]

$$\mathbf{y}^{(k+1)} = \mathbf{y}^{(k)} + \min\left(1, \varphi^*\right)\delta\mathbf{y}^{(k)} \tag{7.43}$$

PD-IPM Algorithm

$$\psi(\boldsymbol{\sigma}) = \tfrac{1}{2}\|F(\boldsymbol{\sigma}_0) - \mathbf{V}_{\text{meas}}\| + \alpha TV(\boldsymbol{\sigma})$$

find a homogeneous $\boldsymbol{\sigma}_0$ to minimise $\|F(\boldsymbol{\sigma}_0) - \mathbf{V}_{\text{meas}}\|$;
initialise dual variable $\mathbf{y}$ to zero;
initialise primal variable $\boldsymbol{\sigma}$ with one step of traditional quadratic regularised inversion;
set initial β;
k=0;
while (termination condition not met)
  $\delta\mathbf{V}_k = (F(\boldsymbol{\sigma}_k) - \mathbf{V}_{\text{meas}})$;
  $J_k = J(\boldsymbol{\sigma}_k)$;
  $E_k =$ diag $(\sqrt{\|L_i\,\boldsymbol{\sigma}_k\|^2 + \beta})$;
  $K_k =$ diag $(1 - \frac{\mathbf{y}_i\, L_i \boldsymbol{\sigma}}{E_k(i,i)})$;
  $\delta\boldsymbol{\sigma}_k = -[J^T J + \alpha L^T E_k^{-1} K_k L]^{-1}\ J_k^T \delta\mathbf{V}_k + \alpha\, L^T E_k^{-1} L\,\boldsymbol{\sigma}_k$;
  $\delta\mathbf{y}_k = \mathbf{y}_k + E_k^{-1} L\,\boldsymbol{\sigma}_k + E_k^{-1} K_k L\,\delta\boldsymbol{\sigma}_k$;
  $\lambda_{\boldsymbol{\sigma}} =$ argmin $\psi(\boldsymbol{\sigma}_k + \lambda_{\boldsymbol{\sigma}}\,\delta\boldsymbol{\sigma}_k)$;
  $\lambda_{\mathbf{x}} = \max\{\lambda_{\mathbf{y}} : \|y_i + \lambda_{\mathbf{y}}\delta y_i\| \leq 1,\ \ i = 1, \ldots, n\}$;
  if a reduction of primal objective function has been achieved
    $\boldsymbol{\sigma}_{k+1} = \boldsymbol{\sigma}_k + \lambda_{\boldsymbol{\sigma}}\,\delta\boldsymbol{\sigma}_k$;
    $\mathbf{y}_{k+1} = \mathbf{y}_k + \min(1, \lambda_{\mathbf{y}})\,\delta\mathbf{y}_k$;
    decrease β by a factor $\beta_{reduction}$;
    decrease $\beta_{reduction}$;
  else
    increase β;
  end if
k=k+1; evaluate termination condition;
end while

Figure 7.2: *Pseudo code for the PD–IPM algorithm with continuation on β, line search on $\boldsymbol{\sigma}$ and dual steplength rule on $\mathbf{y}$.*

where φ^* is a scalar value such that

$$\varphi^* = \sup\left\{\varphi : \left\|\mathbf{y}_i{}^{(k)} + \varphi\delta\mathbf{y}_i{}^{(k)}\right\| \leq 1, \quad i = 1, \ldots, n\right\} \tag{7.44}$$

In the context of EIT, and in tomography in general, the computation involved in calculating the exact step length to the boundary of the dual feasibility region is negligible compared to the whole algorithm iteration. It is convenient therefore to adopt the exact update, which in our experiments resulted in a better convergence. The scaling rule has the further disadvantage of always placing $\mathbf{y}$ on the boundary of the feasible region, which prevents the algorithm from following the central path. Concerning the updates on the primal variable, the update direction $\delta\sigma$ is a descent direction for (P_β) therefore a line search procedure could be appropriate. In our numerical experiments, based on the pseudo code illustrated in Figure 7.2 we have found that for relatively small contrasts (e.g. 3:1) the primal line search procedure is not needed, as the steps are unitary. For larger contrasts a line search on the primal variable guarantees the stability of the algorithm.

7.3 Evaluation Procedure

A reconstruction algorithm that formulates the inverse problem as in equation 7.34 and solves it as in equations 7.38 and 7.39 was developed in the MATLAB environment. The method proposed by Chan *et al* [31] to solve equation 7.35 assumes the forward operator to be linear. The reconstructions that we present in this section of the paper are fully non-linear, the algorithm is shown to work on the cases we used as tests, but we do not provide a proof of convergence.

Evaluation was performed by comparing the performance of the TV PD-IPM algorithm with that of the quadratic algorithm equation 7.3. In equation 7.3 $\mathbf{L} = \mathbf{R}_{HPF}$ where $\mathbf{R}_{HPF}$ is the Gaussian spatial high pass filter originally described in [4]. 2D Simulated data were computed on a 1024 element circular mesh using the two phantoms shown in figures 7.3(a) and 7.3(b). Phantom A is a single "blocky" contrast with a conductivity

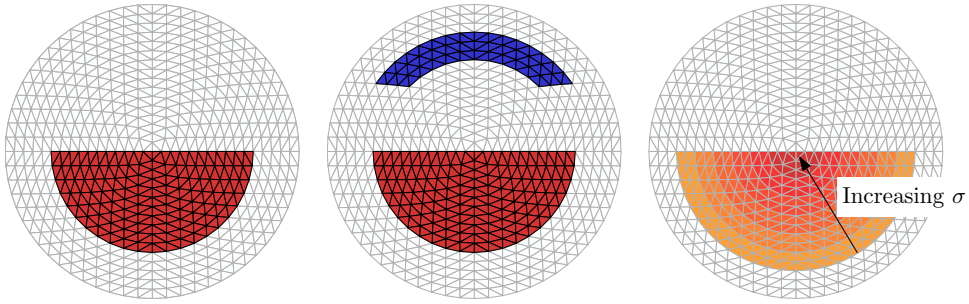

(a) *Phantom A* (b) *Phantom B* (c) *Phantom C*

Figure 7.3: *2D Phantom contrasts on a 1024 element mesh, used to generate simulated data using 16 electrode adjacent current injection protocol.*

of 0.90, phantom B consists of 2 "blocky" contrasts with conductivities of 0.90 and 1.10. Phantom C has a single contrast whose conductivity varies linearly from 1 at the edge to 1.6 at the centre. 15 sets of reconstructions were made for phantoms A and B for each algorithm (TV regularization and ℓ^2 Gaussian regularization) with increasing amounts of simulated noise added. 15 reconstructions were made of phantom C without adding noise. The 16 electrode adjacent protocol was used [4]. 2D reconstructions were performed on a 576 element circular mesh, not matching the mesh used for forward computations, in order to avoid what is referred as an *inverse crime* [122].

7.4 Results

7.4.1 Phantom A

Figure 7.4(a) and 7.4(b) shows that after the first iterative step the TV and the quadratic solutions are similar. The resolution, in terms of blur radius, is slightly better for the TV solution, however visual inspection of figures 7.4(a) and 7.4(b) shows that the TV solution has more noise. Blur Radius (BR) is defined as a measure of the resolution: $BR = \sqrt{A_z/A_0}$ where A_0 is the area of the entire 2D medium and A_z is the area of the reconstructed contrast containing half the magnitude of the reconstructed image [4]. BR calculates the area fraction of the elements that contain 50% of the total image amplitude. We call this the half amplitude (HA) set. The convergence behaviour of the two algorithms is illustrated in Figure 7.5 in which Residual Error, Total Variation, and Resolution are plotted against

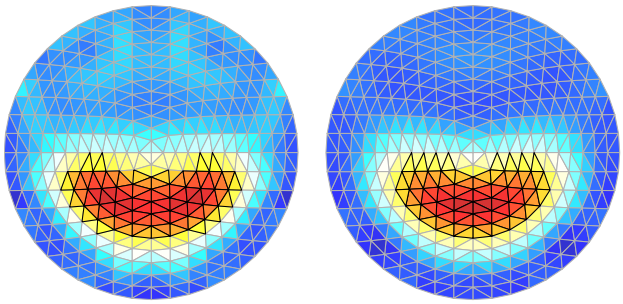

(a) *First step, TV solution.* $BR_{TV} = 0.3741$

(b) *First step,* ℓ^2 *solution.* $BR_{L2} = 0.3643$

Figure 7.4: *Black bordered triangles are elements of the HA set. No noise added.*

iteration number. Both the ℓ^2 and ℓ^1 solutions show steady decrease in Residual Error over the first 4 iterations. By the 5^{th} iteration both solutions have converged in this measure.

3D visualizations of selected TV solutions are shown in Figure 7.7. The characteristic blocky structures of a TV solution start to emerge by the 3^{rd} iteration as shown in Figure 7.7 and by the profile plots of figure 7.6. Visibly detectable improvements in the TV solution are impossible to detect after the 8^{th} iteration with no appreciable changes in the total variation or in the reconstructed images. The profile plots of figure 7.6 show that the TV algorithm is able to reconstruct the profile of phantom almost exactly in the noise free case. Although the residual error of the ℓ^2 solution decreases over the first 4 iterations the Resolution, shown in Figure 7.5(c), has peaked by the 5^{th} iteration . Although not shown, the resulting ℓ^2 images are visually similar. Figure 7.5(c) indicates that the resolution measure of Blur Radius is not a good indicator of TV image quality since the TV and visual images steadily improve while the Blur Radius decrease for the first 3 iterations then increase until it has stabilized by the 8^{th} iteration.

7.4.2 Noise Effects

Noise was added to the simulated data in 15 increments from 0 to a maximum standard deviation of 3% of the signal. Good images, such as those in figures 7.8(a) and 7.8(b) were produced by both algorithms for noise levels smaller than 0.6%. AWGN up to 1.0% produced TV images that by the 7^{th} iteration were recognizable but had large noise artefacts.

AWGN up to 1.0% produced TV images that by the 7^{th} iteration were recognizable but had large noise artefacts. TV reconstructions of data with more than 1.5% noise, as illustrated in figure 7.9(b), were dominated by noise artefacts. The quadratic algorithm was more robust to noise with the best reconstructions occurring with the first step of the algorithm. As more iterations were used the quadratic reconstructions became corrupted by noise. However, the first step of the quadratic algorithm produced a relatively good image quality with noise as high as 2.5%, see Figure 7.9(a).

7.4.3 Phantom B

With low noise, the TV algorithm is able to recover a single blocky object almost exactly. With two objects the TV algorithm provides a reasonable reconstruction however it is unable to recover the profile as accurately as it does in the phantom A case. Figure 7.10 shows the profiles for the TV and ℓ^2 algorithms while figures 7.11(a) and 7.11(b) show reconstructions

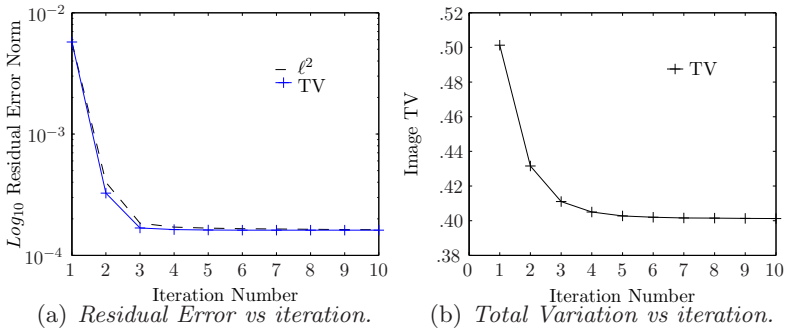

(a) *Residual Error vs iteration.*

(b) *Total Variation vs iteration.*

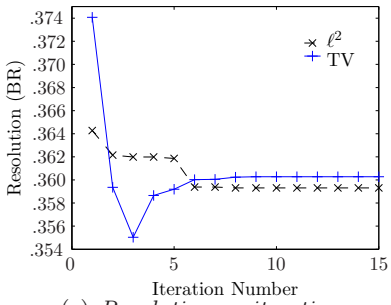

(c) *Resolution vs iteration.*

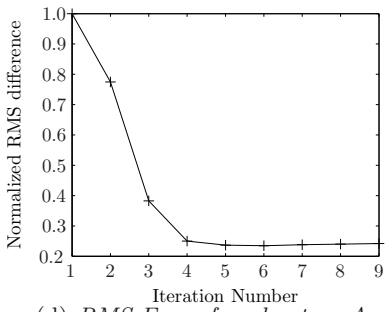

(d) *RMS Error for phantom A.*

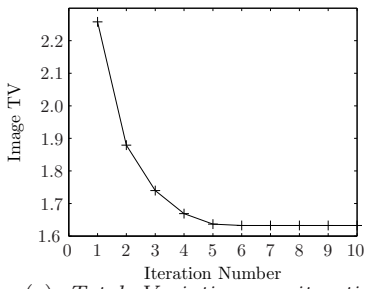

(e) *Total Variation vs iteration for phantom C.*

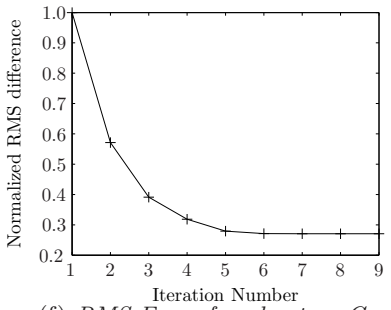

(f) *RMS Error for phantom C.*

Figure 7.5: *Convergence Behaviour of Algorithms. No Noise added.*

from both algorithms for the 8^{th} iteration. Figure 7.10 shows the profiles for the TV and ℓ^2 algorithms while figures 7.11(a) and 7.11(b) show reconstructions from both algorithms for the 8^{th} iteration.

7.4.4 Phantom C

With a single smoothly varying, non-blocky, contrast the TV algorithm provides a reasonable reconstruction of step changes however it is unable to recover the the profile as accurately as it does in the phantom A case. Figure 7.12 shows the profiles for the TV algorithm while figures 7.13 show associated reconstructions for several iterations. Figure 7.5(e) shows the TV convergence of the algorithm for Phantom C, while figure 7.5(f) shows the RMS error between the generating phantom and the reconstruction. The algorithm has converged by the 6^{th} iteration. Interestingly the best image in terms of qualitative matching of the phantom conductivity profile is the 3^{rd} iteration however figure 7.5(f) shows that the RMS error is still decreasing after the 3^{rd} iteration even though later iterations cannot reconstruct the edge between the two largest conductivity values.

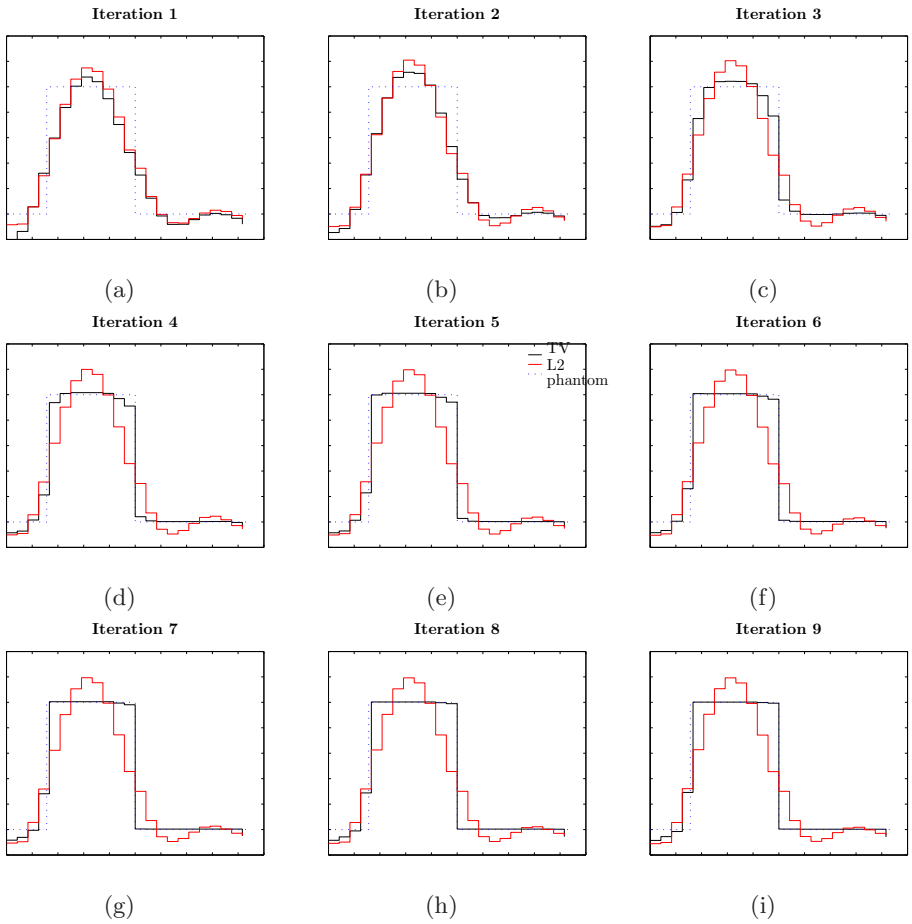

Figure 7.6: *Profile plots of the originating contrast, TV, and ℓ^2 reconstructions. No Noise added. Profiles are vertical slices through the middle of the reconstructed image.*

7.4.5 Parameters

The PD-IPM method has two tuneable parameters β and λ. The value of β has a large effect on convergence. Too large a value of β (greater than 10^{-6}) prevented convergence to the desired "blocky" solution; the solution stabilized but showed smoothed features that were not consistent with the edges obtained with smaller values of β. Ultimately it was determined that the quickest convergence occurred when β was initialized to a small value (we used 10^{-12}) and left unchanged. This was the method used in the results shown in this paper.

With an iterative algorithm multiple values of the regularization hyperparameter, λ, could be used for each iteration. In this work, for the TV algorithm, a different value was used for λ_0, in the initialization step (7.40) and for λ_i in the iterative steps (7.38). λ_0 was selected using the *BestRes* method described in [52]. *BestRes* is an algorithm for objectively calculating the hyperparameter for linearized one-step EIT image reconstruction algorithms. This method suggests selecting a hyperparameter that results in a reconstruction that has maximum resolution for an impulse contrast. Although TV is not intended for use in imaging impulse type contrasts the first step of the algorithm requires solution of the quadratic problem. In previous work the *BestRes* algorithm has provided λ values based on an impulse contrast that has generalized well to non-impulse contrasts. See, for

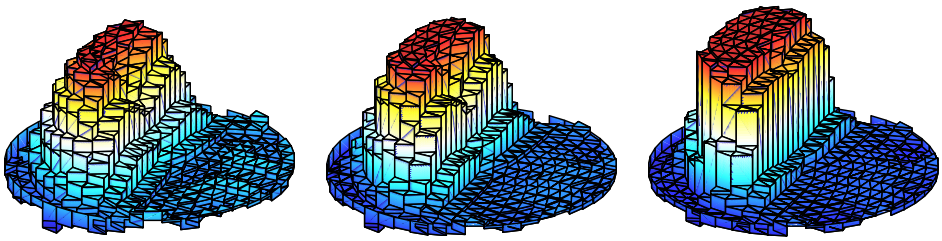

(a) i=1 (b) i=2 (c) i=3

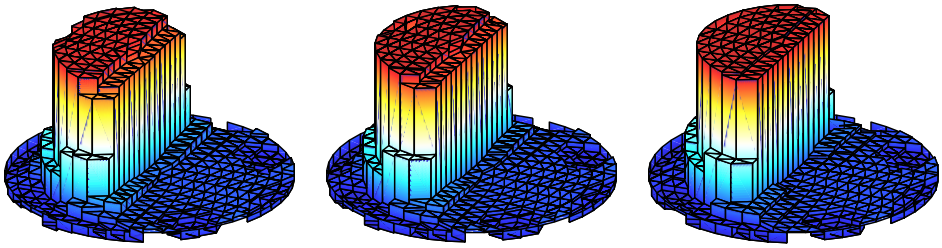

(d) i=4 (e) i=5 (f) i=7

Figure 7.7: *TV reconstructions of Phantom A at increasing iterations. Vertical axis is absolute conductivity. Normalized to 0. No Noise added.*

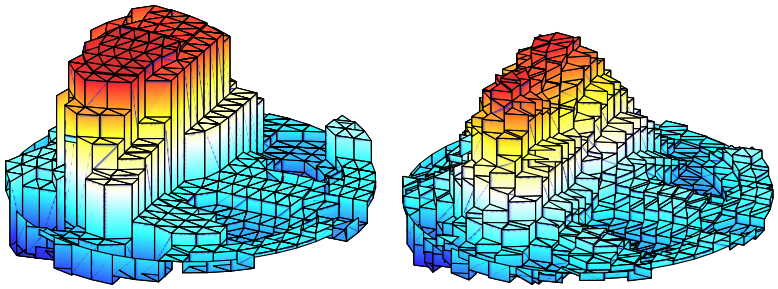

(a) *TV solution at* 7^{th} *iteration.* (b) L^2 *solution at* 7^{th} *iteration.*

Figure 7.8: *Reconstructions of Phantom A with 0.6% AWGN.*

example, the use of *BestRes* in chapter 5. The PD-IPM algorithm did not show to be strongly sensitive to the value of λ_0. We varied the value of λ_0 three orders of magnitude above and one order of magnitude below λ_{BR} without appreciably changing the TV solution at convergence or the rate of convergence.

The initial hyperparameter, λ_0, was always selected using *Best Res*, however, several numerical experiments were performed to determine the effect of the iterative hyperparameter, λ_i, on algorithm performance. Although λ_i could be changed at each iteration, in the reconstructions shown in this manuscript λ_i was maintained constant, thus $\lambda_i = \lambda_{i+1}$. Figure 7.14 shows the results of running the algorithm to convergence six times with a different value λ_i for each run. It is obvious from the figure that the algorithm is sensitive to the value of λ_i; too small a value of λ_i prevents a "blocky" solution, too large a value of λ_i will allow blocky reconstructions but suppress the amplitude. The *BestRes* method was originally used to calculate λ_i however the method was unable to find a good value for λ_i. Best results were obtained by the *ad hoc* visual inspection of figures such as figure 7.14 for various values of λ_i. Further work is required to develop an objective method to select λ_i.

The original PD-IPM methods includes updating the Jacobian matrix at each iteration.

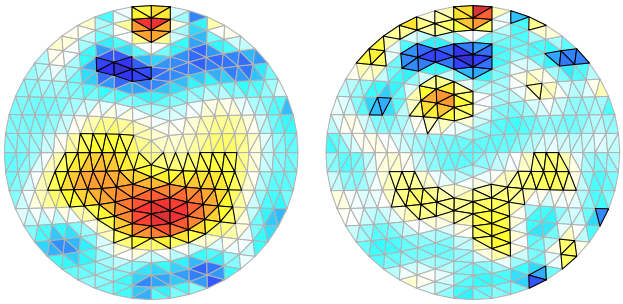

(a) L^2 *solution with 2.5% AWGN, first step. Noisy but useful reconstruction.*

(b) *TV solution with 1.5% AWGN, first step. Noise dominated solution.*

Figure 7.9: *Reconstructions of Phantom A.*

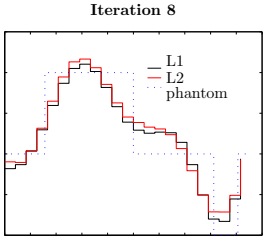

Figure 7.10: *Phantom B profiles.*

In our work numerical experiments this did not result always in a significant improvement in reconstructed images. We adopted therefore a the arrangement of not updating the Jacobian at each single iteration. This provides a reduction in the reconstruction computational time.

As an additional numerical experiment, we evaluated the use of the same regularization matrix L as for TV regularization, (equation 7.9), with the quadratic algorithm (7.3). Although reconstructions from the first step were identical to TV reconstructions, the quadratic solutions rapidly degraded, producing noisy reconstructions that were dominated by noise artefacts after the 10^{th} iteration. The TV prior is not recommended for use with the quadratic algorithm.

7.4.6 Preliminary testing in 3D

The generality of the PD-IPM scheme allows its use for the 3D EIT reconstructions. The method was expected to work equally well in three dimensions, and to be easily extended to this case. To validate this a single experiment with the simulated tank of figure 7.15 was performed. The tank has 315 nodes, 1104 elements, 32 electrodes and is constructed of 4 identical layers of tetrahedrons and was used for both simulating data and reconstruction. A single object in the shape of a crescent was used to generate simulated data. Reconstructions were made on the same mesh. The convergence of the PD-IPM algorithm is shown in figure 7.16. Convergence occurred rapidly with a reasonable image appearing in the first iteration and convergence being achieved by the 8^{th} iteration - there was no appreciable improvement in the image or change in the error norm after the 8^{th} iteration. Figure 7.17 shows slices taken at the five layer boundaries (including top and bottom tank surfaces) of the simulated tank. Figure 7.17 shows reconstructed conductivities after the first iteration, Figure 7.18 shows reconstructed conductivities after 8 iterations. The results were not as good as

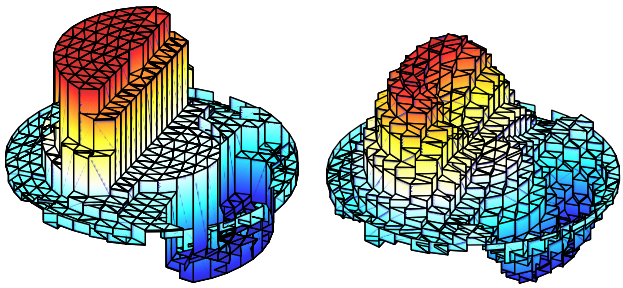

(a) *TV solution at* 8^{th} *iteration*

(b) ℓ^2 *solution at* 8^{th} *iteration*

Figure 7.11: *Reconstructions of Phantom B with 2.5% AWGN.*

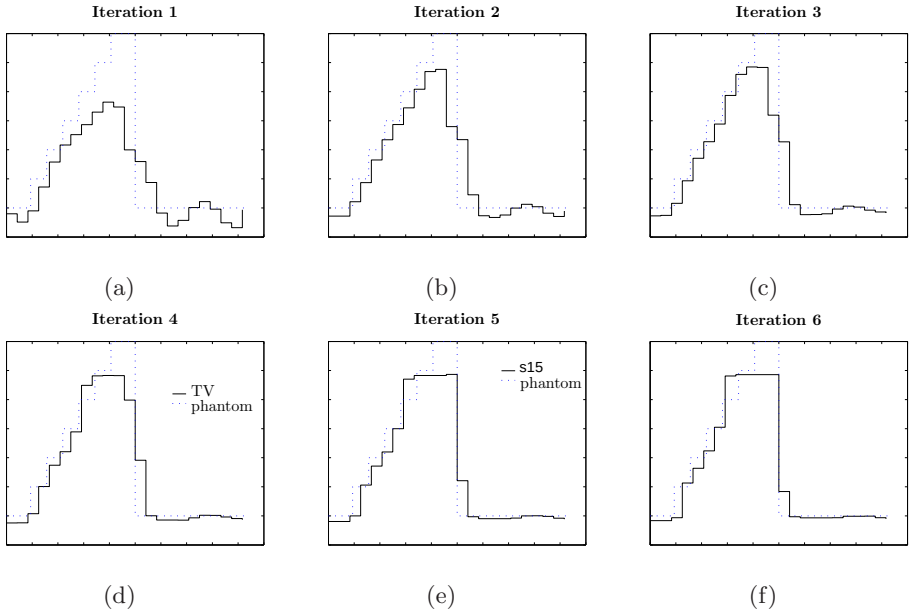

Figure 7.12: *Profile plots of the originating contrast and TV reconstructions for the phantom C, non-blocky, contrast. No Noise added. Profiles are vertical slices through the middle of the reconstructed image.*

the results obtained from the 2D numerical experiments. This may be attributable to poor quality of the 3D model in terms of number of mesh elements. More work is required in order to properly evaluate the performance of PD-IPM in 3D.

Aside on an Inverse Crime The act of employing the same model to generate, as well as to invert, simulated data is known as an *inverse crime* [122]. In earlier work [87] we have cautioned against unqualified publication of results obtained in this manner. The fact that an algorithm works with self simulated data does not imply that it will work well with real data because the use of self simulated data confers an advantage to the algorithm. The acid test for an algorithm occurs when it works successfully with empirical data. However, it is common methodology for researchers to start development of new algorithms using the same model for generation and subsequent inversion of simulated data. The justification is that an algorithm that does not work with such advantageous data will not work at all with real data. Once satisfactory results are obtained with the advantageous data, researchers

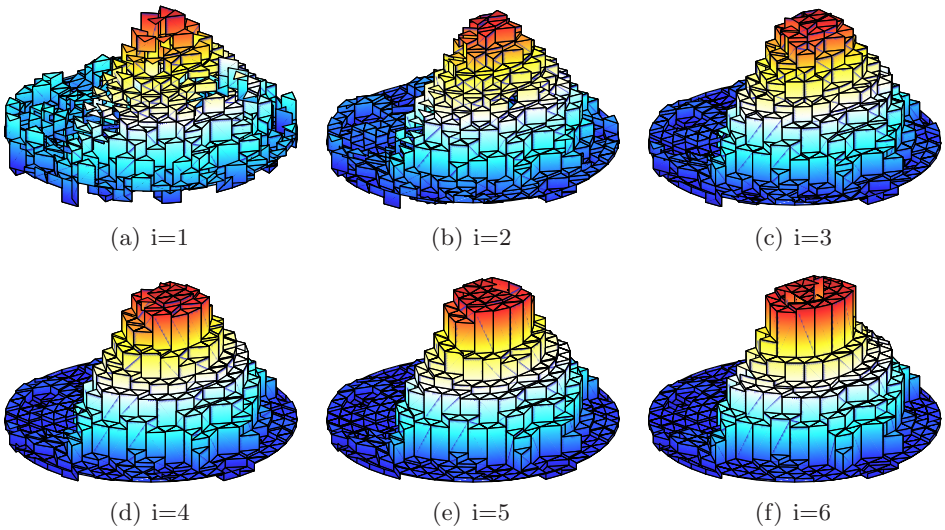

(a) i=1 (b) i=2 (c) i=3

(d) i=4 (e) i=5 (f) i=6

Figure 7.13: *TV reconstructions of Phantom C at increasing iterations. Vertical axis is absolute conductivity. Normalized to 0. No Noise added.*

use lab data or more often noise contaminated simulated data obtained using a different mesh. This paper is primarily concerned with 2D performance. The 3D results reported herein are preliminary and have not yet progressed past the first stage of development. Thus we reluctantly publish results in which an inverse crime is committed. However our aim in this case is simply to demonstrate that the PD-IPM framework can be used for 3D TV regularized reconstructions.

7.5 Discussion and Conclusion

Practical results of the TV regularisation and the efficiency of PD-IPM method are of interest in process and medical imaging. In this work we have demonstrated a practical implementation of a TV regularized reconstruction algorithm for EIT, and compared its performance to a traditional ℓ^2 regularized reconstruction algorithm. Currently, TV regularised reconstructions are considerably more expensive to calculate than quadratic reconstructions, however the TV PD-IMP algorithm is able to compute non-smooth reconstructions in the presence of moderate noise, and it is therefore of practical use.

The typical number of iterations required by the TV PD-IPM algorithm for convergence, and thus for being able to show sharp profiles in the reconstructed images, is on the order of 10 iterations. The quadratic algorithm produces good, albeit smooth, solutions in 1 to 3 steps. Thus there is a clear execution time advantage in using quadratic regularisation. On a 1.8GHz AMD Turion 64 with 1GB ram, one step of the quadratic algorithm took 0.78 seconds for the 576 element mesh, while one step of the PD-IPM algorithm took 0.86 seconds. Thus the TV solution at convergence takes about 9 seconds to calculate compared to the 1 to 2 seconds needed by the quadratic solution.

In our experiments we have found that the quadratic algorithm is slightly more robust to noise however both algorithms produce useful reconstructions at realistic noise levels. Further work will be required to better understanding the convergence behaviour of the PD-IPM algorithm in order to possibly reduce the number of iterations that this algorithm typically requires in order to converge, and thus to make it more competitive in terms of

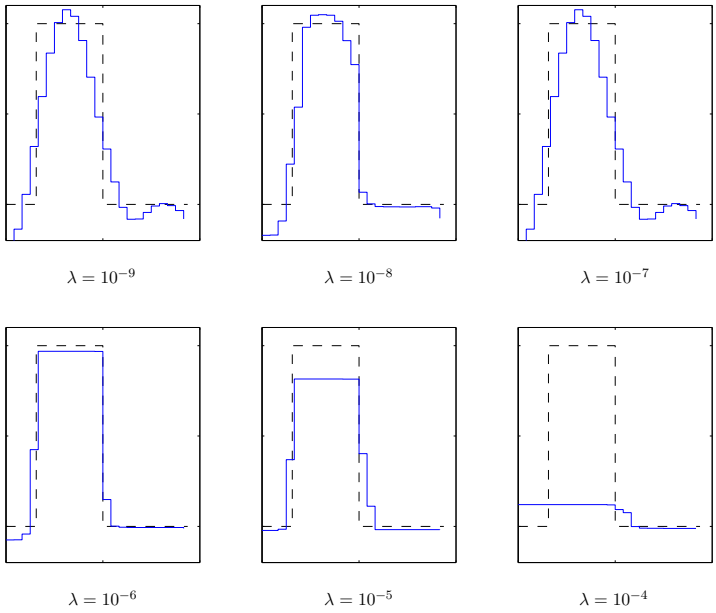

Figure 7.14: *Profiles of TV solutions at the* 7^{th} *iteration (convergence). Showing effect of using different* λ_i *values in equation 7.38. Dotted line is generating contrast, solid line is TV solution.* $\lambda_i \in [10^{-9}, 10^{-4}]$

computational requirements.

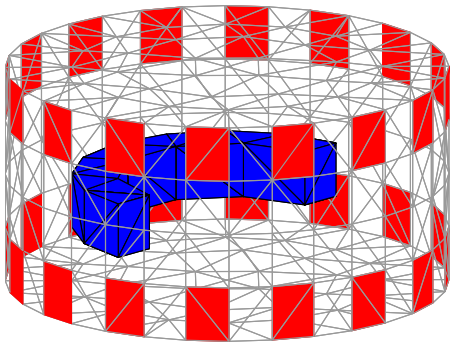

Figure 7.15: *Four layer tank used for 3D reconstructions. Red patches are the 32 electrodes in 2 layers. Phantom contrast are the blue elements which are only in the second layer (between z=1 and z=2). Simulated water depth is full vertical extent of tank.*

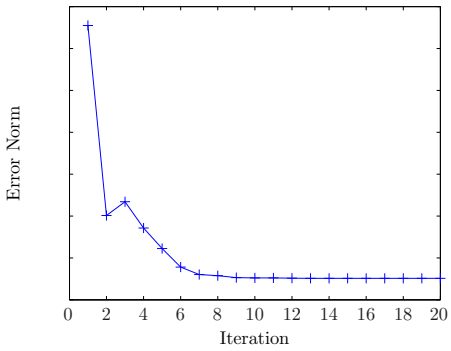

Figure 7.16: *Convergence of 3D PD-IPM algorithm.*

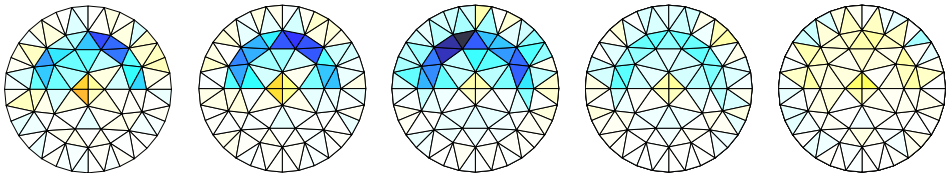

(a) *z=0 (bottom)* (b) *z=1* (c) *z=2* (d) *z=3* (e) *z=4 (top)*

Figure 7.17: *Slices of 3D reconstructions for Iteration 1. No noise added.*

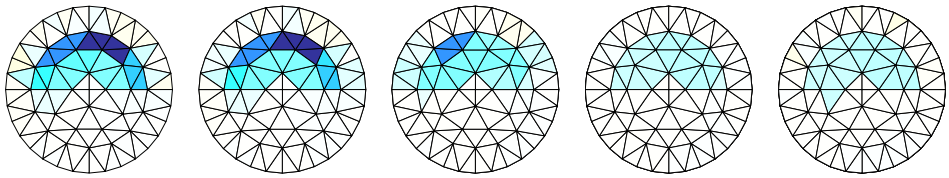

(a) *z=0 (bottom)* (b) *z=1* (c) *z=2* (d) *z=3* (e) *z=4 (top)*

Figure 7.18: *Slices of 3D reconstructions for Iteration 8. No noise added.*

Chapter 8

Conclusion and Future Work

At the start of this work the prevailing algorithms in use for lung/chest imaging were limited to 2D models that relied on *ad hoc* tweaking to produce reconstructions. The aim of this thesis was to develop enhancements in EIT image reconstruction for 3D lung imaging; in other words, to remove some of the limitations that continue to impede the routine use of 3D models for lung imaging. Due to our desire to validate theoretical and simulated models with lab data we constrained our field of investigation to models that could be realized with a 16 electrode scanner designed for tetrapolar (ostensibly adjacent drive protocol) measurements in a 2D configuration. This required the application of engineering principles to develop and analyze reconstruction algorithms and protocols suitable for use with the 16 electrode EIT systems such as the Goe-MF Type II scanner.

The aim was attained through the systematic achievement of the four main objectives:

1. The development of the *BestRes* objective hyperparameter selection method provides a calibration based method of calculating a hyperparameter once for a specific configuration of mesh and equipment. Using this algorithm eliminates the necessity of *ad hoc* tweaking by users during reconstruction. Disparate researchers can now more easily repeat the work of others. Moreover, by calculating the hyperparameter off-line, a good image can be obtained from a single matrix inversion. Contrarily, methods such as L-curve and expert selection require multiple inversions to be calculated for each useful solution. Moreover the L-Curve method is shown to be unreliable for EIT.

2. The development of the *Nodal Jacobian Inverse Solver* algorithm enables the solution of large dense 3D finite element models that, previous to this work, were not easily solvable using linear algebra systems based on 32 bit pointers. This solver allows one to model and solve complex, accurate geometries containing *a priori* structures with linear algebra software that could not solve the same model using the traditional elemental Jacobian.

3. The evaluation of an admittedly small set of potential 3D EP configurations, nevertheless provides a sound basis for recommending a specific method to collect 3D lung data. Moreover it provides a firm basis to discontinue further evaluation of configurations that perform poorly, such as the proposed opposite configurations.

4. The convergence improvements and subsequent evaluation of the PD-IPM algorithm for TV regularization provide a defensible argument for when and when not to use TV regularization. Moreover the promising 2D results provide justification and incentive for further research into this algorithm aimed at increasing the size of 3D models that

can be solved with the algorithm. The development of a nodal TV prior is a promising avenue for further research.

The work described in this thesis has removed some of the major limitations that have discouraged or prevented the routine use of 3D models for lung imaging. This thesis concludes with the following recommendation for how to effectively collect and reconstruct 3D EIT images of the lungs given the stated constraints on equipment and choice of electrodes arranged in 2 planes.

8.1 Recommendation

We recommend the following system to obtain 3D EIT difference images of the lungs for clinical applications. It is based on minimization of the non-linear optimization problem 3.7 which is reproduced below:

$$\hat{\mathbf{x}} = \arg\min_{\mathbf{x}} \left\{ \|\mathbf{Hx} - \mathbf{z}\|^2 + \lambda^2 \|\mathbf{Rx}\|^2 \right\} \tag{8.1}$$

This is solved using the MAP regularized framework of equation 3.22 again repeated below:

$$\hat{\mathbf{x}} = (\mathbf{H^T W H} + \lambda \mathbf{R}^T \mathbf{R})^{-1} \mathbf{H^T W z} = \mathbf{B}(\lambda)\mathbf{z} \tag{8.2}$$

where $\mathbf{z} = \mathbf{v}_2 - \mathbf{v}_1$. The parameters of equation 8.2 are as follows:

1. The regularization hyperparameter λ, is selected using the *BestRes* method of chapter 4.

2. The norm of the prior is the 2-norm. Use of the 1-norm via the TV PD-IPM algorithm for 3D requires further work to extend it to the nodal basis discussed in chapter 5.

3. The prior matrix, $\mathbf{R}$, is the diagonal matrix used in the NOSER algorithm, $\mathbf{R} = diag(\mathbf{H}^T\mathbf{H})$, due to its performance in 3D. The Gaussian prior performs slightly better in 2D but does not have a suitable analog for 3D.

4. The data weighting matrix $\mathbf{W}$ is left as the identity matrix, and is therefore removed from the algorithm. In the case that erroneous electrode data has been revealed through a method such as that of Asfaw and Adler [7] the problem measurements can be accounted for by zeroing each column of the Jacobian matrix $\mathbf{H}$ in equation 8.2.

5. The initial conductivity, σ_0, is left at a homogenous value of 1.

6. The conductivity used to calculate the Jacobian, σ^*, is left at a homogenous value of 1.

7. Using the Nodal inverse solver requires that the FEM parameters include tetrahedral meshes with linear conductivity on each element.

8. For pulmonary imaging we recommend the Planar Electrode Placement Strategy discussed in chapter 6. This is an adjacent current injection and measurement protocol.

8.2 Future Work

There is always more work to do. With respect to the work of this thesis the following subjects are promising areas of future development that could be undertaken to extend the capabilities of the system described in section 8.1:

1. The work of chapter 6 is an initial investigation into the analysis of electrode placements for the thorax. This work was constrained by the availability of 16 electrode equipment and should be extended to consider newer equipment with more than 16 electrodes. Thus future work should systematically investigate potential performance improvements available from electrode placement configurations using more than 16 electrodes arranged in two layers.

2. Clinical measurements to extend the conclusions of the chapter 6, Electrode Placement Configurations for EIT, should be conducted

3. Develop a TV algorithm that uses the nodal inverse solver. The main problem here will be to develop a nodal version of the TV prior matrix. Similar work has been started in [96].

4. Investigate the number of electrodes required to obtain higher resolution reconstructions in 3D. There is speculation that 16 electrodes are not enough for 3D.

Finally, the ability of researchers to extend the contributions in any field of endeavour, but especially fields reliant on software, is made much easier by the ready availability of the software and data used in previously published work. To that end all software used in this work that was developed using Matlab, the EIDORS2D [116] toolbox, and the EIDORS3D [93] toolbox was re-contributed to the EIDORS3D project.

Appendix: Variability in EIT Images Of Lungs: Effect of Image Reconstruction Reference

Authors:
Bradley GRAHAM and Andy ADLER

In the course of completing this thesis several side problems, such as mesh generation, mesh solution bias, and background conductivity effects were examined. These problems are important but are not directly applicable to the aim of this thesis. Morover the the results obtained from these side problems are not yet sufficient for publication. This appendix serves as a means to document the observations made to date on some of the issues caused by background conductivity effects in reconstruction algorithms.

Abstract

There is significant interest in Electrical Impedance Tomography for measurement of breathing. However, Kunst *et al* [83] have shown that variability in parenchyma density (in emphysema and haemodialysis patients compared to normals) had a large effect on the amplitude of EIT images for the same inspired volume. We hypothesize that this effect is due to the assumption made by EIT difference imaging that impedance changes occur relative to a homogeneous conductivity distribution. To test this hypothesis, we developed a 3D finite element model of the thorax, and simulated EIT measurements for a small tidal volume at different levels of lung conductivity. Images were reconstructed using: 1) a homogeneous model, 2) a model with physiologically realistic conductivity levels, and 3) a model with conductivities matching the simulation model.

Results show that the reconstructed image amplitude of the homogeneous model varies strongly with lung conductivity. The magnitude of the variations is compatible with the data of Kunst *et al.* The physiologically realistic model showed a slightly less, but insignificantly so, variation. The matched conductivity model showed much more uniform amplitude response but depended on the area of the inhomogenous region used in construction of the Jacobian.

These results suggest that the variability in EIT image amplitude of the lungs is due to the assumption of homogeneity made by difference EIT image reconstruction algorithms.

Keywords: Electrical Impedance Tomography, Lung Function, Image Reconstruction

A.1 Introduction

One of the most promising applications of Electrical Impedance Tomography (EIT) is for monitoring lung function [50] such as measuring the amount and distribution of inspired air. EIT images of the lung benefit from its large size and large conductivity contrast to other body tissues. Moreover there is a linear relationship between the measured tidal volume and the amplitude of EIT difference images (e.g. [94]). However, the constant of proportionality varies dramatically between subjects.

Kunst *et al* [83] studied the variation in EIT image amplitude between subjects. Images of a given tidal volume[1] were compared between normals and groups with high parenchyma density (haemodialysis patients) and low parenchyma density (emphysema patients). Results were measured in terms of the sum of image pixels per litre of tidal volume. The emphysema group had significantly lower impedance change (11.6 ± 6.4) than normals (18.6 ± 4.2), while the haemodialysis group showed a significantly larger impedance change (30.5 ± 13.1). Furthermore, during dialysis, the latter group showed impedance changes much closer to the normals (21.4 ± 8.6). These results show EIT in poor light: not only can measurements of the same tidal volume vary by a factor of three between patient groups, but even if calibration is performed, the calibration factor can undergo large changes rapidly.

We are interested in understanding the cause of and compensating for this variability in image amplitude. In this paper we deal with the cause. Future work will look at compensation. In this paper, we propose that this effect is mainly caused by the assumption of homogeneity made in the formulation of difference images in EIT via the Jacobian matrix. In order to explore this effect, a finite element model of the thorax was constructed, and simulation data at different baseline lung conductivities generated. Subsequently, images were reconstructed from these data under different difference imaging assumptions, and compared to the results of Kunst *et al* [83].

A.2 Methods

A.2.1 Image Reconstruction

We consider EIT difference imaging, which is widely understood to improve reconstructed image stability in the presence of problems such as unknown contact impedance, inaccurate electrode positions, non linearity, and in the 2D case, the use of 2D approximations for 3D electrical fields [17][87]. We address the class of normalized one-step linearized reconstruction algorithms that calculate the normalized change in finite element conductivity distribution, $\boldsymbol{x}$, due to a change in normalized difference signal, $\mathbf{z}$, over a time interval (t_1, t_2). Here $\mathbf{x}$ is defined as $x_i = \sum_{i}^{length(\mathbf{x})} (\sigma_{2,i} - \sigma_{1,i}) / \sigma_{1,i}$ with $\sigma_{1,i}$ and $\sigma_{2,i}$ being the i^{th} elements of the vectors $\boldsymbol{\sigma_1}$ and $\boldsymbol{\sigma_2}$ respectively, and $\mathbf{z}$ is defined as $z_i = \sum_{i}^{length(\mathbf{v})} (v_{2,i} - v_{1,i}) / v_{1,i}$ with $v_{1,i}$ and $v_{2,i}$ being the i^{th} elements of the vectors $\mathbf{v_1}$ and $\mathbf{v_2}$ respectively. By convention we consider the signal at t_1 to be the *reference* frame and the signal at t_2 to be the *data* frame.

For small changes around a background conductivity the relationship between $\mathbf{x}$ and $\mathbf{z}$ may be linearized as

$$\mathbf{z} = \mathbf{H}\mathbf{x} + \mathbf{n} \tag{A.3}$$

[1] Tidal Volume is the amount of air inhaled and exhaled during normal breathing, normally about between 500 and 1000ml.

where $\mathbf{H}$ is the Jacobian or sensitivity matrix calculated from a FEM ($F(\boldsymbol{\sigma})$), and $\mathbf{n}$ is the measurement system noise, assumed to be uncorrelated additive white Gaussian (AWGN). Each element i, j, of $\mathbf{H}$ is calculated as $H_{ij} = \frac{\partial z_i}{\partial x_j}\Big|_{\boldsymbol{\sigma_0}}$ and relates a small change in the i^{th} difference measurement to a small change in the conductivity of j^{th} element. $\mathbf{H}$ is a function of the FEM, the current injection pattern, and the background conductivity, $\boldsymbol{\sigma_0}$. Here $\boldsymbol{\sigma_0}$ is a vector containing the conductivity of each element of the mesh.

In order to overcome the ill-conditioning of $\mathbf{H}$ we solve A.3 using the following regularized inverse

$$\hat{\mathbf{x}} = (\mathbf{H^T W H} + \lambda^2 \mathbf{R}^T \mathbf{R})^{-1} \mathbf{H^T W z} = \mathbf{B z} \tag{A.4}$$

where $\hat{\mathbf{x}}$ is an estimate of the true change in conductivity distribution, $\mathbf{R}$ is a regularization matrix, λ is a scalar hyperparameter that controls the amount of regularization, and $\mathbf{W}$ models the system noise. The regularization matrix, $\mathbf{R}$, is the spatially invariant Gaussian high pass filter of [4] with a cut-off frequency of 10% of the medium diameter. Hyperparameter selection was performed using the *BestRes* method [52].

Reconstruction algorithms for EIT difference images often assume that the background conductivity, $\boldsymbol{\sigma_0}$, of the region being imaged is homogeneous, and conductivity changes occur with respect to this baseline value. This assumption is clearly unwarranted for imaging of the thorax, where the lungs are significantly less conductive than other tissue. In order to modify the assumption of a homogeneous background conductivity, $\boldsymbol{\sigma_0}$ can be altered to account for the conductivity of the various tissues in the thorax. The sensitivity matrix, $\mathbf{H}$, is then constructed from the modified $\boldsymbol{\sigma_0}$ and used to calculate the reconstructed image.

A.2.2 Simulated Data

Simulated data was generated using the 3D finite element mesh of figure 8.1(b) with the conductive properties of the thorax. This finite element mesh is an extrusion of the 2D mesh of figure 8.1(a). The FEM uses 10368 tetrahedral elements and covers a region 15cm vertically centered on the heart. The sixteen electrodes were spaced equally around the thorax at the level of the centre of the heart. Background conductivity was held constant

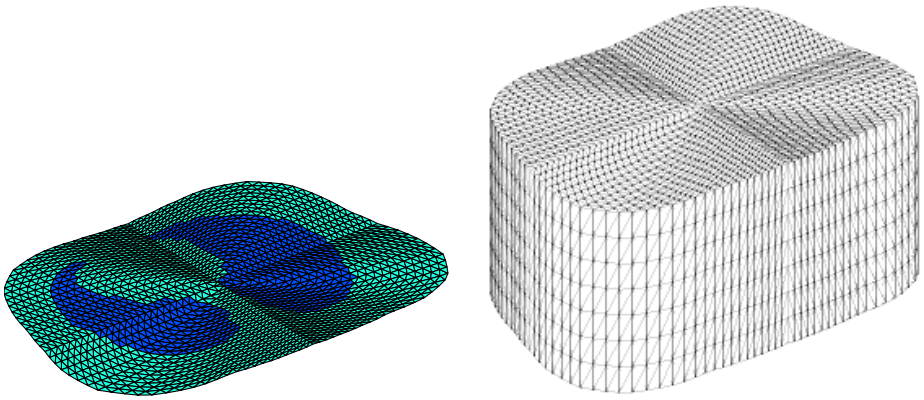

(a) *2D horizontal slice through 3D thorax mesh of figure 8.1(b).* (b) *3D Finite Element mesh of thorax used for simulated data.*

Figure A.1: *Finite Element Mesh for generating simulated data.* $\boldsymbol{\sigma_0}$ *is the vector containing the conductivity of each element,* σ_L *is a scalar value of the conductivity of elements of the lung tissue.*

while the lung conductivity (σ_L) was varied. Simulation data were calculated to model the EIT difference measurements due to introduction of a small tidal volume (ΔV) at different levels of baseline σ_L. Since the relationship between σ_L and lung volume (V_L) is not precisely known in vivo [94], we model lung conductivity as inversely proportional to V_L. For a small ΔV we make the following approximation:

$$\sigma = \frac{\sigma_L}{1 + {}^{\Delta V}/_{V_L}} \approx \sigma_L e^{-{}^{\Delta V}/_{V_L}}$$

Using this approximation, tidal volume, ΔV, constitutes a constant decrease in log conductivity. Difference measurements are simulated for inspiration and expiration as:

$$\begin{aligned} \boldsymbol{v}_{insp} &= F(\sigma_L e^{-{}^{\Delta V}/_{V_L}}) \\ \boldsymbol{v}_{\exp i} &= F(\sigma_L) \end{aligned}$$

Simulations were conducted for $\Delta V/V_L = 10\%$ over a range of 20 values from 5 mS/m to 2000 mS/m. This large non-physiological range was simulated in order to clarify the trend of the results. The reference frame was taken at the background lung conductivity.

A.2.3 Evaluation Procedure

Six sets of reconstructions were calculated using a 1968 element 2D finite element model. Images were reconstructed from the simulated data and using three different reconstruction algorithms: 1) using a homogeneous $\boldsymbol{\sigma_0}$, 2) using $\boldsymbol{\sigma_0}$ with physiological values and $\boldsymbol{\sigma_0}$ at its inspiration value (60 mS/m) ($\Delta V_{EIT,Inspi}$), and 3) using $\boldsymbol{\sigma_0}$ with physiological values and σ_L matching σ_L that was used to simulate the data $\Delta V_{EIT,Simul}$. In the third algorithm the area of the non-homogenous region, A_{σ_L} of the FEM was varied; thus four sets of reconstructions were calculated with areas of $A_{\sigma_L} = 33\%$, $A_{\sigma_L} = 51\%$, $A_{\sigma_L} = 73\%$, and $A_{\sigma_L} = 86\%$ as shown in figure A.2. Thus the single set of 20 simulated measurements was used to reconstruct six sets of 20 images.

An EIT estimate of tidal volume, ΔV_{EIT}, was then calculated by summing all pixels of the 2D FEM weighted by the pixel's area. $\Delta V_{EIT} = \sum_{i=1}^{E} A_i \sigma_i$ where A_i is the area/volume of element i and σ_i is the conductivity of element i.

A.3 Results

Figure A.3 shows four plots of image amplitude vs baseline lung conductivity, σ_L, for each algorithm. The different subplots correspond to non-homogenous Jacobians of differing area. The two curves for the homogenous Jacobian algorithms (blue and black lines) are the same in each of the subplots.

The results for $\Delta V_{EIT-Homo}$ (black curve) are consistent with those of Kunst *et al* [83]. Image amplitude for the same proportional volume change increases dramatically with increasing baseline (starting/initial) lung conductivity; there is a large increase in image amplitude as σ_L increases from 60 mS/m to 120 mS/m. Use of constant but physiologically realistic values reduces the dependence only slightly (blue curve). The use of parameters that match the simulation (red curve) results in significant decrease in the dependence on σ_L. However the effect is strongly dependent on the area of the inhomogeneity of the reconstruction mesh used to calculate the Jacobian. Figure 8.3(a), in which the inhomogeneous area, $A_{\sigma_{\hat{L}}}$ is 33%, shows a strong dependence on σ_L for $\sigma_L < 120$ mS/m but becomes

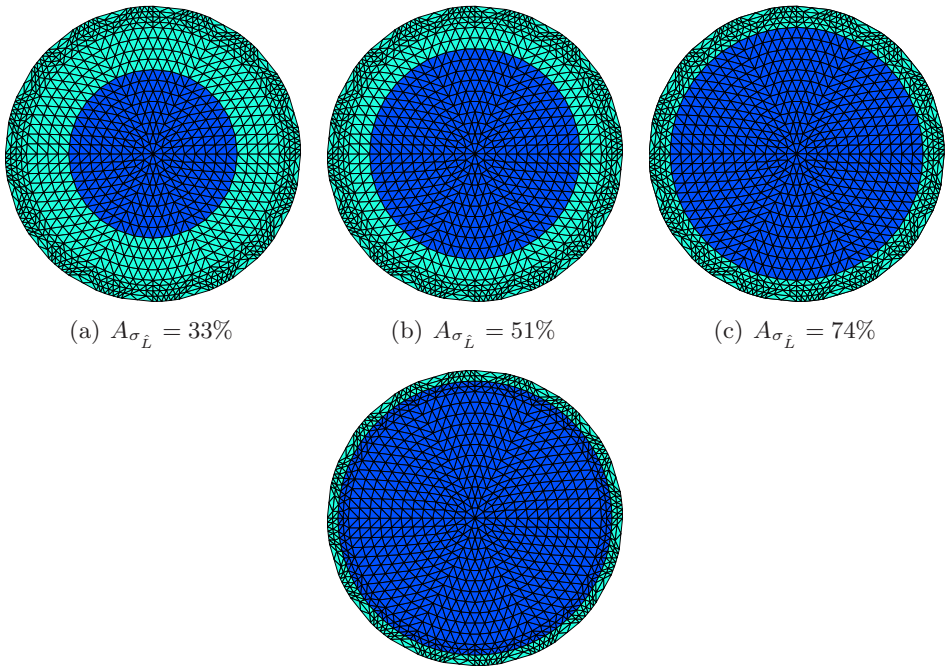

(a) $A_{\sigma_{\hat{L}}} = 33\%$ (b) $A_{\sigma_{\hat{L}}} = 51\%$ (c) $A_{\sigma_{\hat{L}}} = 74\%$

(d) $A_{\sigma_{\hat{L}}} = 86\%$

Figure A.2: *Meshes used for non-homogenous Jacobian construction. Dark elements are the inhomogenous regions of the matched algorithm.*

independent after. The most stable response occurs with $A_{\sigma_{\hat{L}}} = 73\%$ which is almost flat throughout the range of σ_L. All three of the curves from $A_{\sigma_{\hat{L}}} \geq 51\%$ to $A_{\sigma_{\hat{L}}} \leq 86\%$ have improved independence of σ_L. Figures A.4 and A.5 are 2D reconstructions for the two homogenous algorithms. These images clearly show the increasing image amplitude as σ_L increase from 5mS/m to 2000mS/m. Figures A.6 and A.7 are images from two of the inhomogeneous algorithms. They show that the variability in image amplitude over the range of σ_L is considerably reduced compared to the two homogenous models.

A.4 Conclusion

It is desired that a given proportional lung volume/conductivity change always produce the same proportional signal. We show that this is not possible using a homogenous reconstruction model. However analysis of the experimental data suggest a method to reduce the magnitude of this variability. By incorporating an inhomogenous region in the centre of the reconstruction mesh used to construct the Jacobian and setting the inhomogenous to the matched conductivity of σ_L, the variability of the amplitude of the reconstructed image can be reduced. Of course this is impossible in practice since we cannot know σ_L of the patient. However, these results suggest method to reduce the variability if an estimate of the background conductivity could be obtained perhaps through a crude two parameter estimate of the static conductivity of the patient.

Our motivation for this study is to understand the causes of the results of Kunst *et al*[83] in which different baseline lung conductivity levels introduced a dramatic difference in the magnitude of EIT images of the same tidal volumes. We have developed a rough simulation model of the effect of the assumption of homogeneous baseline lung conductivity

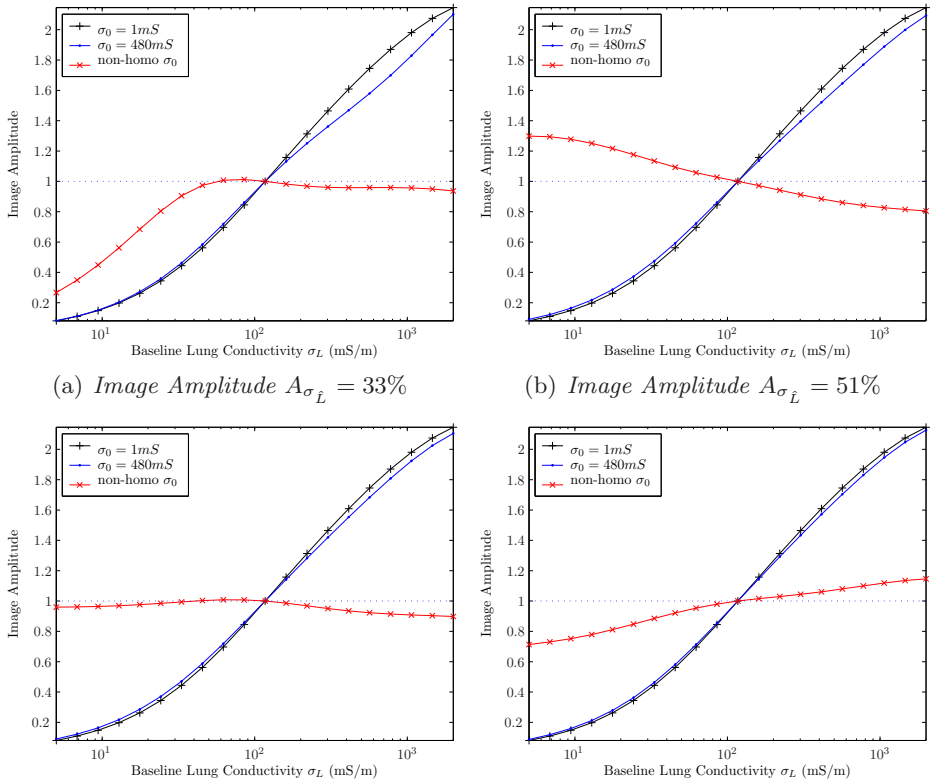

(a) *Image Amplitude* $A_{\sigma_{\hat{L}}} = 33\%$ (b) *Image Amplitude* $A_{\sigma_{\hat{L}}} = 51\%$

(c) *Image Amplitude* $A_{\sigma_{\hat{L}}} = 73\%$ (d) *Image Amplitude* $A_{\sigma_{\hat{L}}} = 86\%$

Figure A.3: *EIT difference image amplitude due to a small tidal volume as a function of baseline lung conductivity (σ_L) (mS/m). Image amplitude is normalized to a value of 1.0 when lung conductivity matches expiration (120 mS/m). Black curve: images reconstructed with homogeneous background, Blue curve: images reconstructed with lung region conductivity of 60 mS/m, Red curve: images reconstructed with lung region conductivity equal to the simulation model value (on horizontal axis).*

on EIT images, which is able to account for the magnitude of the observed effect. This result suggests that the variability observed could possibly be eliminated by enhancements to EIT image reconstruction algorithms. On the other hand, many other factors could contribute to the observed effect, such as:

1. breathing pattern differences (abdominal versus thoracic breathing),
2. size of thorax,
3. nonlinear relationship of conductivity change to inspired volume,
4. movement of the chest with breathing,
5. changes in Cole-Cole parameters of lung tissue in patients with haemodialysis and emphysema.

We postulate that the baseline conductivity effect is dominant, as most of the other factors would appear to be significantly smaller than the observed variability. For example, a simulation study of the movement of the chest with breathing showed changes due to

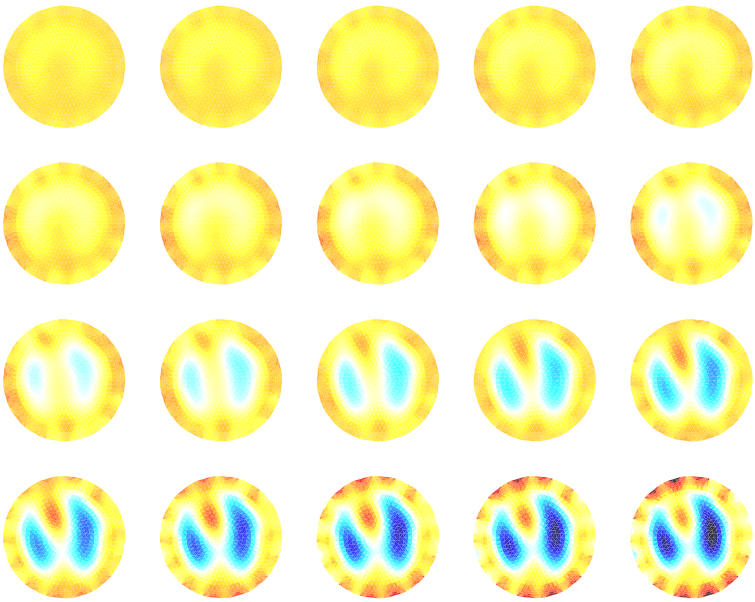

Figure A.4: *Reconstructions with homogenous Jacobian:* $\sigma_0 = 1mS$.

movement of approximately 20% [5]. Modifications in baseline conductivity may also explain the variability in EIT images with changes in posture [66].

In conclusion, these results suggest that an important contribution to variability in the amplitude of EIT difference images of the lungs is the assumption of homogeneity of the background conductivity in difference image reconstruction; furthermore, modifications to image reconstruction algorithms may be able to reduce the magnitude of the variability.

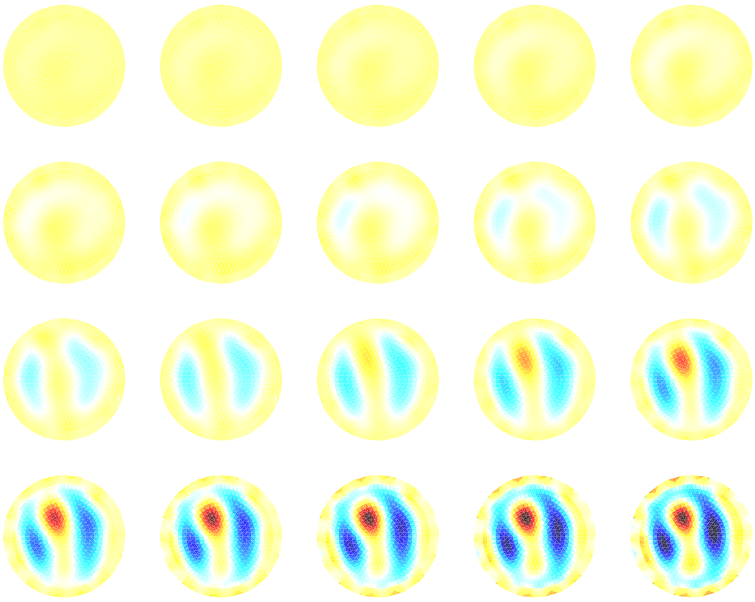

Figure A.5: *Reconstructions with physiologically realistic homogenous Jacobian:* $\sigma_0 = 480mS$.

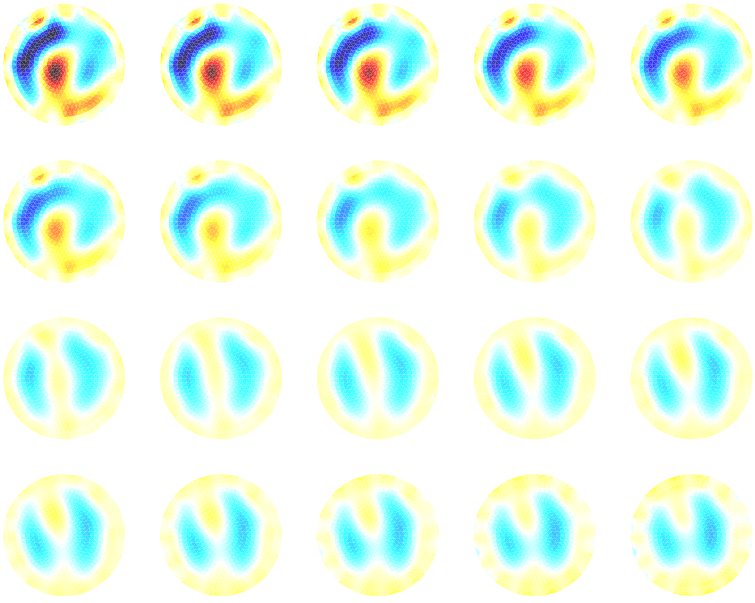

Figure A.6: *Reconstructions with non-homogenous Jacobian with* $A_{\sigma_{\hat{L}}} = 73\%$.

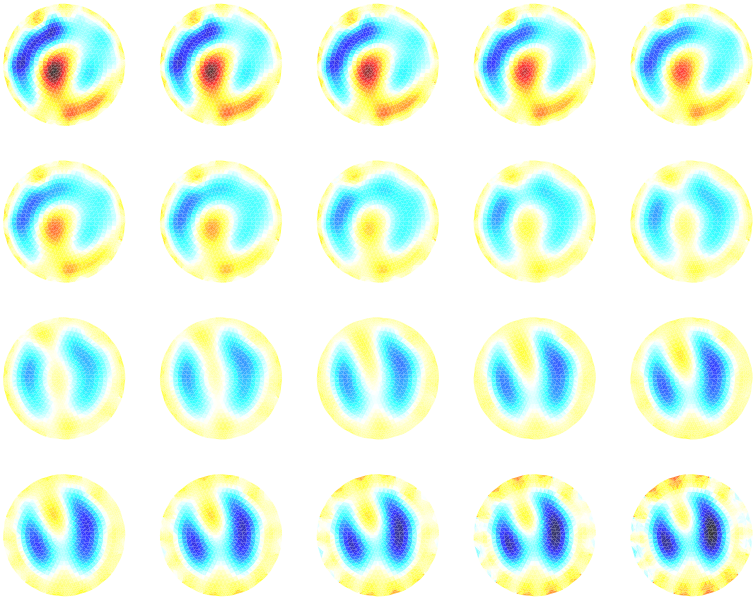

Figure A.7: *Reconstructions with non-homogenous Jacobian with* $A_{\sigma_{\hat{L}}} = 86\%$.

Bibliography

[1] Abdullah MZ, Electrical impedance tomography for imaging conducting mixtures in hydrocyclone separators, PhD Thesis, UMIST, 1993.

[2] Acar R, Vogel C R, Analysis of bounded variation penalty methods for ill-posed problems. Inverse Problems, 10, 1217-1229, 1994.

[3] Adler A, Measurement of Pulmonary Function with Electrical Impedance Tomography, Ph.D. Thesis, Institut de Génie Biomedical Université de Montréal, 1995.

[4] Adler A, Guardo R, Electrical impedance tomography: regularised imaging and contrast detection, IEEE Trans Med Imaging, 1996, 15 170-9

[5] Adler A, Guardo R, and Berthiaume Y, Impedance imaging of lung ventilation: Do we need to account for chest expansion? IEEE Trans Biomed Eng, 1996 43, 414-420.

[6] Adler A, Accounting for erroneous electrode data in electrical impedance tomograhy, Physiol Meas, 2004, 25, 227-238

[7] Asfaw Y, Adler A, Automatic Detection of detached and erroneous electrodes in electrical impedance tomography, 2005, Physiol Meas, 26 S175-S183.

[8] Adler A, Lionheart WRB, Uses and abuses of EIDORS: An extensible software base for EIT, 2006, Physiol Meas, 27, S25-S42.

[9] Alessandrini G, Rondi L, Stable determination of a crack in a planar inhomogeneous conductor, SIAM J Math Anal, 1998, 30, 326-340.

[10] Aster R, Borchers B, Thurber C, Parameter Estimation and Inverse Problems, Elsevier Academic Press, 2004.

[11] Andersen KD, Christiansen E, A Newton Barrier method for Minimizing a Sum of Euclidean Norms subject to linear equality constraints, Technical Report, Dept of Mathematics and Computer Science, Odense University, Denmark, 1995.

[12] Andersen KD, An efficient Newton barrier method for minimizing a sum of Euclidean norms, SIAM J on Optimization, 1996, 6, 74-95.

[13] Andersen KD, Christiansen E, Conn AR, Overton ML. An efficient primal-dual interior-point method for minimizing a sum of Euclidean norms, SIAM J on scientific computing, 2000, 22, 243-262.

[14] Avis NJ, Barber DC, Image reconstruction using non-adjacent drive configuration, Physiol Meas, 1994, 16, A153-A160.

[15] Barber DC, Brown BH, Applied potential tomography, J Phys E: Sci Instrum, 1984, 17, 723-733.

[16] Barber DC, A review of reconstruction techniques for electrical impedance tomography, Med Phys, 1989, 16, 162-169.

[17] Barber DC, Brown BH, Single step Algorithms for Image reconstruction,IEEE Trans. Biomedical Engineering, 1988, 32, 100-105.

[18] Barber DC, Brown BH, Errors in reconstruction of resistivity images using a linear reconstruction technique, Clin Phys Physiol Meas, 1988, 9, 101-4.

[19] Barrodale I, Roberts FDK, An efficient algorithm for discrete l_1 linear approximation with linear constraints, SIAM J Numer Anal, 1978, 15 , 603-611.

[20] Bayford RH, Gibson A, Tizzard A, Tidswell T, Holder DS, Solving the forward problem in electrical impedance tomography for the human head using IDEAS (integrated design engineering analysis software), a finite element modelling tool, Physiol, Meas, 2001, 22, 55-64.

[21] Blott BH, Cox SJ, Daniell GJ, Caton MJ, Nicole DA, High fidelity imaging and high performance computing in nonlinear EIT, Physiol Meas, 2000, 21, 7-13,

[22] Blue RS, Isaacson D, Newell JC, Real-time three-dimensional electrical impedance imaging, Physiol Meas, 2000, 21, 1-12.

[23] Borsic A, Regularisation Methods for Imaging from Electrical Measurements, PhD Thesis, Oxford Brooks University, 2002.

[24] Borsic A, Lionheart WRB, McLeod CN, Generation of anisotropic regularisation filters for Electrical Impedance Tomography, IEEE Trans Med Imaging, 2002, 21, 579- 587.

[25] Borsic A, McLeod CN, Lionheart WRB, Total Variation Regularisation in EIT Reconstruction, Proceedings of the 2nd World Congress on Industrial Process Tomography, 2001, 433.

[26] Breckon WR, Image reconstruction in electrical impedance tomography. PhD Thesis, Oxford Polytechnic, 1990.

[27] Brown BH, Seagar AD, The Sheffield data collection system, Clin Phys Physiol Meas, 1987, 8 (suppl A) 91-7.

[28] Brown BH, Leathard AD, Lu L, Wang W, Hampshire A, Measured and expected Cole parameters from electrical impedance tomographic spectroscopy images of the human thorax, 1995, Physiol Meas, 16, A57-A67.

[29] Calderon AP, On an inverse boundary value problem Seminar on Numerical Analysis and its Applications to Continuum Physics, Rio de Janeiro: Soc Brasil Mat, 1980, 65-73.

[30] Chan TF, Golub GH, Mulet P, A Nonlinear Primal-Dual Method for Total Variation-Based Image Restoration, UCLA Math Department CAM Report, 1995, 95-43.

[31] Chan T, Marquina A, Mulet P, High-order total variation-based image restoration, SIAM Journal on Scientific Computing, 1998, 19, 1046-1062.

[32] Chan T F, Zhou H M, and Chan R H. A continuation method for total variation denoising problems. UCLA CAM Report 95-18, 1995.

[33] Chen ZQ, Paoloni PJ, An integral Equation Approach to Electrical Conductance Tomography, IEEE Trans on Med Imaging, 1992, 11(4), 570-576.

[34] Cheng KS, Isaacson D, Newell JC, Gisser DG, Electrode model for electric current computer tomography, IEEE Transations on Biomedical Engineering, 1989, 36, 918-924.

[35] Cheney M, Isaacson D, Newell JC, Simske S, Goble JC, NOSER: An algorithm for solving the inverse conductivity problem Internat, J Imaging Systems & Technol 1990, 2, 66-75.

[36] Cohen-Bacrie C, Goussard Y, Guardo R, Regularized reconstruction in electrical impedance tomography using a variance uniformization constraint, IEEE Trans. Medical Imaging, 1997, 16, 562-571.

[37] Cheney M, Isaacson D, Issues in Electrical Impedance Imaging, IEEE Computational Science and Engineering, 1995, 2, 53-62.

[38] Clay MT, Feree TC, Weighted regularization in electrical impedance tomography with applications to acute cerebral stroke, IEEE Trans Med Imaging, 2002, 21 629-637.

[39] Coleman TF, and Li Y, A globally and quadratically convergent affine scaling method for linear $\ell 1$ problems, Mathematical Programming, 1992, 56, 189-222.

[40] Cook RD, Salunier GJ, Gisser DG, Goble JC, Newell JC, Isaacson D, ACT3: High-speed, high-precision electrical impedance tomograph, IEEE Trans Biomed Imag, 1993, 41, 713-722.

[41] Dehgani H, Soni N, Halter R, Hartov A, Paulsen KD, Excitation patterns in three-dimensional electrical impedance tomography Physiol Meas, 2005 26 S185-S197.

[42] Demidenko E, Hartov A, Soni N, Paulsen K, On Optimal Current Patterns for Electrical Impedance Tomography, IEEE Trans Biomed Eng, 2005, 52, 238-48.

[43] Dickin F, Wang M, Electrical resistance tomography for process tomography, Meas Sci Tech, 1996, 7, 247-260.

[44] Dobson DC, Santosa F, An image enhancement technique for electrical impedance tomography. Inverse Problems, 1994, 10, 317-334.

[45] Dobson D C, Vogel C R. Convergence of an iterative method for total variation denoising. SIAM J. on Numerical Analysis, 43, 1779-1791, 1997.

[46] Eyüboglu BM, Brown BH, Barber DC, In vivo imaging of cardiac related impedance changes, IEEE Eng Med Biol Mag, 1989, 8, 3945.

[47] Eyüboglu BM, Pilkington TC, Comments on distinguishability in electrical impedance tomography, IEEE Trans Biomed Eng, 1993, 40, 1328-1330.

[48] Faes TJC, van Genderingen HR, Noordegraaf AV, Some reflections on the EIT Conference (London, UK, 22-24 June 2005), Proc. 6th Conf. on Biomedical Applications of EIT. Physiological Measurement, 27, 2005.

[49] Frerichs I, Hahn G, Hellige G, Thoracic Electrical Impedance Tomographic Measurements During Volume Controlled Ventilation-Effects of Tidal Volume and Positive End-Expiratory Pressure, IEEE Trans. Medical Imag, 18, 768-778, 1999.

[50] Frerichs I, Electrical impedance tomography (EIT) in applications related to lung and ventilation: a review of experimental and clinical activities, Physiol. Meas. 21:R1-R21, 2000.

[51] Gadd R, Record P, Rolfe P, Finite element modelling for electrical impedance tomography, Proc 12th Annual Conf of the IEEE Engineering in Medicine and Biology Society, 1990, 133-4.

[52] Graham BM, and Adler A, Objective Selection of Hyperparameter for EIT, Physiol Meas, 2006, 27, S65-S79.

[53] Graham BM, and Adler A, A Nodal Jacobian Inverse Solver for Reduced Complexity EIT Reconstructions, Int. J. for Information & Systems Sciences, 2, 453-68.

[54] Graham BM, and Adler A, Electrode Placement Configurations for EIT, Physiol Meas, 2007, in press.

[55] Geselowitz DB, An application of electrocardiographic lead theory to impedance plethysmography, IEEE Transactions on Biomedical Engineering, 1971, 18, 38-41.

[56] Gibson A, Bayford RH, Holder DS, Two-dimensional finite element modelling of neonatal head, Physiol Meas, 2000, 21, 45-52.

[57] Gisser G, Isaacson D, Newell JC, Current topics in impedance imaging, Clin Physiol Meas, 1987, 8:38-46.

[58] Gisser DG, Isaacson D, Newell JC, Theory and performance of an adaptive tomography system, Clin Phys Physiol Meas, 1988, 9, A35-A41.

[59] Gobel JC, Cheney M, Isaacson J, Electrical Impedance Tomography in three dimensions, Appl Comput Electromagn Soc J, 1992, 7, 128-147.

[60] Gonzalez GC, Woods RE, Digital Image Processing Second Edition, Prentice Hall, 2002.

[61] Griffiths H, Zhang Z, A dual-frequency electrical impedance tomography system, Phys Med Biol, 1989, 34, 1465-1476.

[62] Hahn G, Thiel F, Dudykevych T, Frerichs I, Gersing E, Schröder T, Hartung C, Hellige G, Quantitative Evaluation of the performance of different electrical tomography devices, Biomed Technik, 2001, 46, 91-95.

[63] Hansen PC, Rank-Deficient and Discrete Ill-Posed Problems: Numerical Aspects of Linear Inversion, SIAM, Philadelphia, 1998.

[64] Hansen PC, Analysis of discrete ill-posed problems by means of the L-Curve, SIAM Review, 1992, 34, 561-580.

[65] Hansen PC, Regularization Tools: A Matlab package for analysis and solution of discrete ill-posed problems, Numerical Algorithms , 1994, 6, 1-35.

[66] Harris HD, Suggett AJ, Barber DC, Brown BH, Applied Potential Tomography: A New Technique for Monitoring Pulmonary Function., Clin. Phys. Physiol. Meas., 9, A79-A85, 1988.

[67] Harris ND, Brown BH, Barber DC, Continuous monitoring of lung ventilation with electrical impedance tomography, Med Biol Soc, 1992, 1754-1755.

[68] Heath MT, Scientific Computing: An Introductory Survey 2^{nd} Ed., McGraw Hill, New York, 2002.

[69] Holder DS, Electrical Impedance Tomography: Methods, History and Applications, Institute of Physics, 2004.

[70] Holder DS, Electrical impedance tomography of brain function, Brain Topography, 1992, 5, 87-93.

[71] Hua P, Webster JG, Tompkins WJ, A regularised electrical impedance tomography reconstruction algorithm, Clin Phys Physiol Meas, 1988, 4A, 137-141

[72] Hua P, Woo EJ, Webster JG, Iterative reconstruction methods using regularisation and optimal current patterns in elecrical impedance tomography, IEEE Trans Med Imag, 1991, 10, 621-628.

[73] Hua P, Webster JG, Tompkins WJ, Effect of the measurement method on noise handling and image quality of EIT imaging, IEEE 9th Annual Conf on Engineering in Medicine and Biological Science, 1993, 1429-30.

[74] Hua P, Woo EJ, Webster JG, Tompkins WJ, Finite Element Modeling of Electrode-Skin Contact Impedance in EIT, 1993, IEEE Trans Biomed Eng, 40, 335-343.

[75] Huebner KH, Dewhirst DL, Smith DE, Byrom TG, The Finite Element Method for Engineers, 4th Edition, Wiley 2001.

[76] Isaacson D, Distinguishability of conductivities by electric current computed tomography, IEEE Trans Med Imag, 1986, 5, 91-95.

[77] Kaipo JP, Kolehmainen V, Vauhkonene M, Somersalso E, Inverse problems with structural prior information, Inverse Problems, 1999, 15,713:729.

[78] Kaipio JP, Kolehmainen V, Vauhkonen M, Somersalo E, Construction of nonstandard smoothness priors, Inverse Problems, 1999, 15, 713-729.

[79] Kaipio JP, Kolehmainen V, Somersalo E, Vauhkonen M, Statistical inversion and monte carlo sampling methods in electrical impedance tomography, Inverse Problems, 2000, 16, 1487-1522.

[80] Karmarkar N, A new polynomiacl-time algorithm for linear programming. Combinatorica, 4, 373-395, 1984.

[81] Karl WC, Regularization in image restoration and reconstruction, in Handbook of Image and Video Processing, Bovik A, Ed, chapter 3, 141-161. Academic Press, 2000.

[82] Kerrouche N, McLeod CN, Lionheart WRB, Time series of EIT chest images using singular value decomposition and fourier transform. Physiol Meas, 2001, 22, 147-157.

[83] Kunst PWA, Vonk Noordegraaf A, Hoekstra OS, Postmus PE, de Vries PMJM, Ventilation and perfusion imaging by electrical impedance tomography: A comparison with radionuclide scanning, Physiol Meas, 1998, 19, 481-490.

[84] Kaipio JP, Kolehmainen V, Somersalo E, Vauhkonen M, Statistical inversion and Monte Carlo sampling methods in electrical impedance tomography, Inv Probl 2000, 16, 1487-1522.

[85] Kohlemainen V, Novel approaches to image reconstruction in diffusion tomography, PhD Thesis, Department of Applied Physics, Kuopio University, 2001.

[86] Kotre CJ, EIT image reconstruction using sensitivity weighted filtered backprojection, Physiological Measurement, 1994, 15, A125-A136.

[87] Lionheart WRB, Review: Developments in EIT reconstruction algorithms: pitfalls, challenges and recent developments, Physiol Meas, 2004, 25, 125-142.

[88] Loke MH, Electrical imaging surveys for environmental and engineering studies-A practical guide to 2D and 3D surveys, 1997, Short training course lecture notes. Universiti Sains Malaysia, Penang, Malaysia.

[89] Meeson S, Blott BH, Killingback ALT, EIT data noise evaluation in the clinical environment, Physiol Meas, 1996, 17, A33-38.

[90] Metherall P, Barber DC, Smallwood RH, Brown BH, Three dimensional electrical impedance tomography, Nature, 1996, 380, 509-12.

[91] Molinari M, Cox S, Blott BH, Daniell GJ, Comparison of algorithms for non-linear inverse 3D electrical tomography reconstruction, Physiol Meas, 2002, 23, 95-104.

[92] Murai T, Kagawa Y, Electrical impedance computed tomography based on finite element model, IEEE Transactions on Biomedical Engineering, 1985, 32, 177-184.

[93] Polydorides N, Lionheart WRB, A MATLAB based toolkit for three-dimensional Electrical Impedance Tomography: A contribution to the EIDORS project, Measurement Science and Technology, 2002, 13, 1871-1883.

[94] Nopp P, Rapp E, Pfutzner H, Nakesch H, Ruhsam C, Dielectric Properties of Lung Tissue as a Function of Air Content, Phys. Med. Biol,38, 699-716, 1993.

[95] Paulsen K, Meaney P, Moskowitz M, Sullivan J, A dual mesh scheme for finite element based reconstruction algorithms, IEEE Trans on Medical Imaging, 1995, 14, 504-14.

[96] Paulsen K, Jiang H, An enhanced electrical impedance imaging algorithm for hyperthermia applications, Int J Hyperthermia, 1997, 3(5), 459-80.

[97] Pinheiro PA, Investigation of forward problem solvers and data collection methods in electrical impedance tomography, 1994, MSc Dissertation UMIST.

[98] Polydorides N, Image reconstruction algorithms for soft-field tomography, PhD Thesis, UMIST, 2002.

[99] Polydorides N, McCann H, Electrode configurations for improved spatial resolution in Electrical Impedance Tomography, Meas Sci Technol, 2002, 13 , 1862-1870.

[100] Pilkington TC, Morrow MN, Stanley PC, A comparison of finite element and integral equation formulations for the calculation of electrocardiographic potentials, IEEE Trans Biomed Eng, 1985, 32, 166-173.

[101] Rockefellar RT, Convex Analysis, Princeton, Princeton University Press, 1970.

[102] Rudin LI, Osher S, Fatemi E, Nonlinear total variation based noise removal algorithms, Physica D, 1992, 60, 259-268.

[103] Seagar AD, Bates RHT, Full-wave computed tomography part 4: Low-frequency electric current CT, IEE Proceedings, 1985, 132, 455-466.

[104] Seppänen A, Vauhkonen M, Somersalo E, Kaipio JP, State space models in process tomography - approximation of state noise covariance, Inverse Problems in Engineering, 2001, 9, 561-585.

[105] Seppänen A, Vauhkonen M, Vauhkonen PJ, Somersalo E, Kaipio JP, State estimation with fluid dynamical evolution models in process tomography - an application to impedance tomography, Inv Probl, 2001, 17, 467-484.

[106] Silvester PP, Ferrari RL, Finite Elements for Electrical Engineers, Cambridge University Press, 3rd edition, 1996.

[107] Smallwood RH, Mangnall YF, Leathard AD, Transport of gastric contents, Physiol Meas, 1994, 15, 175-188.

[108] Somersalo E, Isaacson D, Cheney M, Existence and uniqueness for electrode models for electric current computed tomography, SIAM J Appl Math, 1992, 52, 1023-40.

[109] Somersalo E, Kaipio J, Vauhkonen M, Baroudi D, Järvenpää S, Impedance imaging and Markov chain Monte Carlo methods, 1997, SPIE Proceedings Series, Vol 3171, 175-185.

[110] Soni NK, Paulsen KD, Dehghani H, Hartov A, Image Reconstruction in Electrical Impedance Tomography Using The Full Set of Maxwell's Equations, Scientific Abstracts from the 6th Conference on Biomedical Applications of Electrical Impedance Tomography, University College London, June 22-24 2005.

[111] Tenorio L, Statistical Regularization of Inverse Problems, SIAM Review, 2001, 43, 347-366.

[112] Vauhkonen M, Electrical Impedance Tomography and Prior Information, PhD thesis, Department of Applied Physics, Kuopio University, 1997.

[113] Vauhkonen M, Kaipio JP, Somersalo E, Karjalainen PA, Electrical impedance tomography with basis constraints, Inv Probl, 1997, 13, 523-530.

[114] Vauhkonen M, Vadász D, Karjalainen PA, Somersalo E, Kaipio JP, Tikhonov regularization and prior information in electrical impedance tomography, IEEE Trans Med Imaging, 1998, 17, 285-293.

[115] Vauhkonen PJ, Vauhkonen M, Savolainen T, Kaipio JP, Three-dimensional electrical impedance tomography based on the complete electrode model, IEEE Trans Biomed Eng, 1999, 46, 1150-1160.

[116] Vauhkonen M, Lionheart WRB, Heikkinen LM, Vauhkonen PJ and Kaipio JP, A Matlab Package for the EIDORS project to reconstruct two-dimensional EIT images, Physiol Meas, 2001, 22 107-111.

[117] Vogel C, Computational methods for inverse problem, SIAM, Philadelphia, 2001.

[118] Vogel C R, Oman M E. Iterative methods for total variation denoising. SIAM J. Sci. Computing, 17, 227-238, 1996.

[119] Wahba G, Practical Approximate Solutions to Linear Operator Equations When the Data Are Noisy, SIAM Journal of Numerical Analysis, 1977, 14, 651-667.

[120] Wheeler J, Wang W, Tang M, A comparison of methods for measurement of spatial resolution in two dimensional circular EIT images, Physiol Meas, 2002, 23, 169-76.

[121] Vavasis SA, Stable finite elements for problems with wild coefficients, SIAM J Numer Anal, 1996, 33, 890-916.

[122] Wirgin A, The inverse crime ArXiv Mathematical Physics e-prints arXiv:math-ph/0401050, 2004.

[123] Woo EJ, Hua P, Webster JG, Tompkins WJ, Measuring lung resistivity using electrical impedance tomography, IEEE Trans Biomed Eng, 1992, 39, 756-60.

[124] Wright S J, Primal Dual Interior Point Methods, SIAM, Philadelphia, 1997.

[125] Xue G, Ye Y, An Efficient Algorithm for Minimizing a Sum of Euclidean Norms with Applications, SIAM Journal on Optimization, 2000, 10, 551-579.

[126] Yorkey TJ, A quantitative comparison of the reconstruction algorithms used in impedance tomography, PhD Thesis, University of Wisconsin, 1986.

[127] Yorkey TJ, Webster JG, Tompkins WJ, Comparing reconstruction algorithms for electrical impedance tomography, IEEE Trans Biomed Eng, 1987, BME-34, 843-852.

[128] Yorkey TJ, Webster JG, Tompkins WJ, An improved perturbation technique for electrical impedance imaging with some criticisms, IEEE Trans Biomed Eng, 1987, BME-34, 898-901.

[129] Zhu QS, McLeod CN, Denyer CW, Lidgey FJ, Lionheart WRB, Development of a real-time adaptive current tomograph, Physiol Meas, 1994, 15, A37-A43.

VITA

Name:	Bradley Michael Graham P.Eng
Place and Year of Birth:	Scarborough Township, Ontario, Canada, 1962
Education:	Ph.D Student, Electrical and Computer Engineering, University of Ottawa 2002-2007 M.Sc, Computer Science, Queen's University 2000-2001 B.Eng, Computer Engineering, First Class Honours, 2000 Royal Military College of Canada, 1996-2000
Experience:	Aerospace Engineering Officer, Canadian Forces, 1996-2007 Research Assistant, Queen's University, Summer 2001 Teaching Assistant, Queen's University, 2000-2001 Aircraft Technician, Canadian Armed Forces, 1987-1996
Awards:	NSERC PGS A, 2000 OGS, 2000 Queen's Ross R.S. McLaughlin Fellowship, 2000